

MULTIPOINT CONVERTER TOPOLOGIES
FOR DISTRIBUTED ENERGY SYSTEM APPLICATIONS

A Dissertation

by

JOSHUA TIMOTHY HAWKE

Submitted to the Office of Graduate and Professional Studies of
Texas A&M University
in partial fulfillment of the requirements for the degree of

DOCTOR OF PHILOSOPHY

Chair of Committee,	Prasad N. Enjeti
Committee Members,	B. Don Russell
	Shankar P. Bhattacharyya
	Perla Balbuena
Head of Department,	Chanan Singh

August 2014

Major Subject: Electrical Engineering

Copyright 2014 Joshua Timothy Hawke

ABSTRACT

In the midst of a present-day global energy renaissance, power electronics has evolved into a top-tier technology discriminator in distributed energy resource (DER) systems. Faced with the formidable task of integrating various types of DER technologies into singular systems, there is a growing appetite for multiport converter (MPC) design. In response, three unique DER MPC topologies are presented: the power sharing converter (PSC), the multi-level nine switch converter (ML9SC), and the modular fuel cell hybrid energy storage (MFC+HES) converter.

First, low-voltage and medium-voltage PSC architectures are shown to decouple series-connected source currents and enable independent control. Multidimensional modeling and analysis is then discussed. Next, three system designs are discussed: single-zone, dual-zone, and multi-zone. Each implements PSC technology and high-frequency isolated full-bridge converters to interface multiple fuel cell sources to a medium voltage grid via a single multilevel neutral point clamped inverter interface. A 1-MW simulation and a reduced-scale hardware prototype offer collaborative insight into the inherent benefits of the proposed PSC systems: increased output power, operational flexibility, thermal balancing, source availability, and cost-effectiveness.

Secondly, the ML9SC is presented as a component-minimized multi-port converter with low cost, high efficiency, high power quality, and low noise. The multiport characteristic of the ML9SC can be effectively employed in uninterruptible power systems, six-phase wind generators, and doubly-fed induction wind generators. Next,

operating constraints and modulation index limits are analyzed at different operating conditions. Loss breakdown is analyzed and compared with the conventional back-to-back multi-level converter. Finally, simulation results are included as proof of concept.

Lastly, the proposed MFC+HES converter integrates energy-dense MFC technology with power-dense storage technology. System modularization and hybridization are discussed initially, followed by a selection between supercapacitors and lithium-ion batteries (LIBs). Next, system topology and design is discussed, and the MFC and LIBs are electrically modeled such that Middlebrook's Extra Element Theorem can mitigate unwanted system resonance and optimize system design. Simulation and hardware results for a 100W MFC+HES system realizes a 300% boost current response capability as well as the following system benefits: limp-home capability, evenly distributed heat/aging, and maximized output power.

ACKNOWLEDGEMENTS

I would like to thank my committee chair, Prof. Enjeti, and my committee members, Prof. Russell, Prof. Bhattacharyya, and Prof. Balbuena, for their guidance and support throughout the course of this research.

Also, a special thanks goes to my friends and colleagues with whom I've had the distinct pleasure of working here at Texas A&M. Prof. Al-Othman your tutelage and friendship has inspired me greatly. Harish, I am thankful for all you've taught me; you are going to be a great professor someday! Wenping, it was pleasure getting to know you both as a friend and a colleague. Jackie, Tammy, Jeanie, Janice, and Annie, thank you for your selfless support and open doors; it's been an honor working with you.

Next, I want to take a moment to express my deepest appreciations towards the many scholarship programs which have not only helped me achieve this degree, but also taught me the significance of investing and believing in others. Specific thanks goes to the ASEE-SMART Program and the Terry Foundation.

Finally, I am extremely grateful for the support of my friends and family. Chris, Jacoby, Paul, Mike, Michelle, and Travis, thanks for being pillars in my life. Mom, thank you for raising me well and teaching me to always remain diligent and faithful before the Lord. To Chelsea, my bride: your love and encouragement warm my heart and inspire me to be my best; I am the luckiest man in the world to have you by my side! And to my Father: thank you for your wisdom, your patience, and your love. You are truly faithful to finish the work that you have begun in me.

NOMENCLATURE

A	Amps
AC	Alternating Current
ANPC	Active Neutral Point Clamped
B2B	Back to Back
CPG	Center Point Grounding
DC	Direct Current
DFIG	Doubly-Fed Induction Generator
DER	Distributed Energy Resource
DERS	Distributed Energy Resource Systems
DF	Different Frequency
EDLC	Electronic Doubly Layer Capacitor
EMI	Electromagnetic Interference
ESD	Energy Storage Device
FC	Fuel Cell
H	Henry
HES	Hybrid Energy Storage System
HF	High Frequency
HFI	High Frequency Isolation
Hz	Hertz
I	Current

IGBT	Insolated Gate Bipolar Transistor
L	Inductance/Inductor
LF	Low Frequency
LIB	Lithium-Ion Battery
LV	Low Voltage
LV	Low Voltage Power Sharing Converter
M_a	Modulation Index
MFC	Modular Fuel Cell
MISO	Multi-Input Single-Output
MIMO	Multi-Input Multi-Output
ML9SC	Multi-Level Nine-Switch Converter
MOSFET	Metal-Oxide Semiconductor Field-Effect Transistor
MV	Medium Voltage
MV-PSC	Medium Voltage Power Sharing Converter
MW	Mega-Watt
MPC	Multiport Converter
N	Turns-Ratio
NPC	Neutral Point Clamped
P	Power
PSC	Power Sharing Converter
PSIM	Powersim CAD Software
P.U.	Per Unit

PV	Photovoltaic
R	Resistor/Resistance
RMS	Root Mean Squared
SC	Supercapacitor
SFDP	Same-Frequency Different-Phase
SFSP	Same-Frequency Same-Phase
SIMO	Single-Input Multi-Output
STO	Strategic Technology Office
THD	Total Harmonic Distortion
UPS	Uninterruptible Power Supply
V	Voltage/Volts
W	Watt
WTG	Wind Turbine Generation
3L	Three Level
9SC	Nine-Switch Converter
Ω	Ohm

TABLE OF CONTENTS

	Page
ABSTRACT	ii
ACKNOWLEDGEMENTS	iv
NOMENCLATURE	v
TABLE OF CONTENTS	viii
LIST OF FIGURES	x
LIST OF TABLES	xvi
CHAPTER I INTRODUCTION AND TOPICAL OVERVIEW	1
Market Relevance	1
Power Electronics and Distributed Energy Systems	1
The Power Sharing Converter Family	2
The Multi-Level Nine-Switch Converter	3
The Modular Fuel Cell with Hybrid Energy Storage Converter	3
CHAPTER II POWER ELECTRONICS AND DISTRIBUTED ENERGY	4
Energy Electronics: A New Age	4
Distributed Energy Resource Systems	5
Multiport Converters and Resource Bundling	5
CHAPTER III THE POWER SHARING CONVERTER FAMILY	7
Introduction	7
Proposed Power Sharing Converter Technology	10
The Fuel Cell and the Power Sharing Converter	16
Proposed Fuel Cell Power Sharing Converter Grid Connection Topologies	24
Fuel Cell Power Sharing Converter Design Considerations	29
Simulation Results	35
Experimental Results	37
Conclusion	44

CHAPTER IV THE MULTI-LEVEL NINE-SWITCH CONVERTER.....	45
Introduction and Literature Review	45
Proposed Dual-Output Multilevel Converter Topology and Modulation Scheme...	50
Modulation Index Analysis	56
Case Study: Efficiency Analysis of an Online UPS.....	65
Simulation Results.....	76
Conclusion.....	81
CHAPTER V THE MODULAR FUEL CELL WITH HYBRID ENERGY STORAGE CONVERTER	82
Introduction and Concept Overview	82
System Modularization.....	83
System Hybridization	91
Source Modeling	92
The Modular Fuel Cell with Hybrid Energy Storage	102
Conclusion.....	115
CHAPTER VI CONCLUSIONS AND FUTURE WORK.....	116
REFERENCES.....	117
APPENDIX A CASE STUDY: HYBRID ENERGY STORAGE DEVICE SELECTION	124
Modular Fuel Cell Supercapacitor Interface	126
Modular Fuel Cell Li-Ion Battery Interface	127
Modular Fuel Cell / Hybrid Interface.....	128

LIST OF FIGURES

		Page
Figure 1	Conventionally, multiple utility-scale fuel cells are interfaced with a medium voltage utility grid via independent converter strings with bulky 60Hz isolation transformers.	8
Figure 2	The proposed FC power conditioning architecture implements both Low Voltage- and Medium Voltage-Power Sharing Converter (LV/MV-PSC) topologies. By doing so, converter count and component count are reduced and the usage of large 60 Hz transformers is eliminated. Also, each fuel cell is capable of operating at independent power levels.	10
Figure 3	The proposed LV-PSC topology allows Source-1 α and Source-2 α to operate at unique power levels by switching between the two states illustrated in (a.) and (b.). For example, if $P1\alpha > P2\alpha$, then $IL\alpha > 0$	11
Figure 4	If $P1\alpha > P2\alpha$, $D1\alpha$ increases and subsequently induces a positive steady state DC-current through the zonal power sharing inductor as shown by the voltage and current waveforms above.	13
Figure 5	The proposed MV-PSC decouples $P1\gamma$ and $P2\gamma$ at higher voltages by switching between the two states illustrated in (a.) and (b.). The clamping diodes help balance voltages across $S1\gamma$ and $S2\gamma$ or $S3\gamma$ and $S4\gamma$, while the HF Isolated DC-DC Converters hold $V1\gamma = V2\gamma$	15
Figure 6	Linear current dependency characterizes the fuel cell's PV-curve (red) and produces the resulting PI-curve (blue). Two potential power points (50% and 100%) are noted in order to inspect the case where $P1\alpha > P2\alpha$	17
Figure 7	The proposed LV-PSC topology allows FC-1 α and FC-2 α to operate at unique power levels. For example, if $P1\alpha > P2\alpha$, then $IL\alpha > 0$	19

Figure 8	The plots above illustrate the relationship between FC input currents (I_1 and I_2) and PSC output power (P_o) in (a.) 2-d and (b.) 3-d. Golden arrows are used to show how increasing D_1 can adjust the ratio of I_1 to I_2 while maintaining a constant output power.21
Figure 9	The plots above illustrate the relationship between FC input voltages (V_1 and V_2) and PSC output power (P_o) in (a.) 2-d and (b.) 3-d. Golden arrows are used to show how increasing D_1 can adjust the ratio of V_1 to V_2 while maintaining a constant output power.23
Figure 10	The proposed Single-Zone FC-PSC topology provides HF isolation while allowing each fuel cell unit (FC-1 α and FC-2 α) to operate at unique power levels and interface with a medium-voltage three-phase 60 Hz utility grid.....25
Figure 11	The proposed Dual-Zone FC-PSC topology permits each fuel cell unit (FC1, FC2, FC3, and FC4) to operate at a unique power level and interface with a medium-voltage three-phase utility grid, while allowing a variable-voltage power sharing between the DC/DC converter outputs.....27
Figure 12	The proposed Multi-Zone FC-PSC topology permits each fuel cell unit (FC1, FC2, FC3, and FC4) to operate at a unique power level and interface with a medium-voltage three-phase utility grid, while introducing new control strategy flexibilities.....29
Figure 13	Fuel cell filter circuit and AC equivalent used for filter design.....30
Figure 14	PSIM simulation of a single-zone FC-PSC topology where $P_{1\alpha} = 100\%$ and $P_{2\alpha} = 10\%$, displaying: (i.) the power sharing inductor current $I_{L\alpha}$, (ii.) the unfiltered current $I_{1\alpha}$ with large ripples, (iii.) filtered source current $I_{1\alpha,avg}$ with small ripples, and (iv.) filtered source current $I_{2\alpha,avg}$ with small ripples.....31
Figure 15	Simulation results for design example power levels: $P_{1\alpha} = 250$ kW, $P_{2\alpha} = 50$ kW, $P_{1\beta} = 80$ kW, and $P_{2\beta} = 120$ kW. Verifies zone DC-DC converter output voltage balancing ($V_{o\alpha} + V_{o\beta} = V_d$) as well as zone inductor current dependence on varying individual fuel cell power levels.36
Figure 16	The fuel cell power operation points $P_{1\alpha} = 100\%$, $P_{2\alpha} = 20\%$, $P_{1\beta} = 32\%$, and $P_{2\beta} = 48\%$ are arbitrarily chosen, yielding the above voltage and current characteristic values.....37

Figure 17	The power sharing inductor current (blue) directly follows manual adjustments in the control reference signal (yellow), illustrating system capacity for bidirectional inductor current flow during power sharing between sources. Note: 1 division = 5A.....	38
Figure 18	Given Case I's fuel cell input characteristics on the left, the zonal power sharing inductor waveforms are shown on the right. The two verify power sharing for Case I (100% /100%). $V_1 = V_2 \cong 12V$ for $D = D' = 50\%$ and $I_{L\alpha} \cong 0A$	40
Figure 19	Given Case II's fuel cell input characteristics on the left, the zonal power sharing inductor waveforms are acquired on the right. The two verify power sharing for Case II (100% /50%). $V_2 \cong 18V$ for $D' = 40\%$, $V_1 \cong 14.4V$ for $D = 60\%$, and $I_{L\alpha} \cong +2.8A$	42
Figure 20	Given Case III's fuel cell input characteristics on the left, the zonal power sharing inductor waveforms are acquired on the right. The two verify power sharing for Case III (20% /80%). $V_1 \cong 21.6V$ for $D = 40\%$, $V_2 \cong 14.4V$ for $D' = 60\%$, and $I_{L\alpha} \cong -2.3A$	43
Figure 21	Review of topologies with reduced switches: the B4 converter [44].....	46
Figure 22	Review of topologies with reduced switches: the Five-leg converter [45].....	47
Figure 23	Review of topologies with reduced switches: the Four-leg converter [46].....	47
Figure 24	Review of topologies with reduced switches: the nine-switch converter [48].....	48
Figure 25	Review of topologies with reduced switches: the six-switch converter [50].....	48
Figure 26	Traditional dual-output 3-level converter.....	51
Figure 27	Proposed switch-minimized dual-output 3-level converter topology.....	52
Figure 28	Modulation Scheme and Constraint of Proposed Converter.....	55
Figure 29	Modulation waveforms for SFSP operation.....	57
Figure 30	Typical SFSP Application for Proposed Topology: Online UPS.	58

Figure 31	Maximum modulation index as the phase difference is adjusted in SFDP Mode.	60
Figure 32	Typical SFDP Application for Proposed Topology: Six-Phase Wind Generation	61
Figure 33	Two sets of modulation waveforms during DF Mode operation.	63
Figure 34	Typical DF Application for Proposed Topology: DFIG Wind Generation	64
Figure 35	Voltages and Currents for Both Dual-Outputs	65
Figure 36	Interval ②'s Operating Diagram for one switching cycle.	66
Figure 37	Interval ④'s Operating Diagram for one switching cycle.	68
Figure 38	Loss Breakdown (P=30kW, fs=10kHz).	71
Figure 39	Loss distribution of individual switch (P=30kW, fs=10kHz).	72
Figure 40	Efficiency vs. output power.	73
Figure 41	Efficiency vs. Switching Frequency.....	74
Figure 42	Loss vs. Output Power Factor.	75
Figure 43	Driving signals.	76
Figure 44	Input and Output waveforms.	77
Figure 45	Harmonic spectrum distribution of output voltage.	77
Figure 46	THD comparison of proposed converter and 9-switch converter.	78
Figure 47	Dynamic response under abrupt load variations.	79
Figure 48	Input and Output Voltage Waveforms when the converter is operated in DF mode.	80
Figure 49	Conventional fuel cell stack (n cells) with two end terminals and an isolated dc-dc converter.....	84
Figure 50	Exploded view of a modular fuel cell with three stack sections.	84

Figure 51	Modular fuel cell and dc-dc converter concept with three sections.	85
Figure 52	V-I characteristics of the 3-section modular fuel cell proposed in Figure 51.	86
Figure 53	Output power produced by each section of the 3-section modular fuel cell proposed in Figure 51.	86
Figure 54	Thermal imaging of a conventional fuel cell stack, showing temperature imbalance.	88
Figure 55	Thermal imaging of a modular fuel cell stack, showing temperature balance.	88
Figure 56	Operation of the modular fuel cell modular dc-dc converter under a fault. Note: Section 2 current is reduced to zero, while the output voltage continues to be regulated.	90
Figure 57	This Ragone Plot illustrates how SCs and LIBs are legitimate candidates for the quick response ESD hybridized with the MFC.	91
Figure 58	Non-modular fuel cell system connected with a high-power energy storage device and interfaced with dc-dc converters.	93
Figure 59	Review of LIB Models: The Rint Model.	94
Figure 60	Review of LIB Models: The RC Model.	95
Figure 61	Review of LIB Models: The Thevenin Model.	96
Figure 62	Review of LIB Models: The PNGV Model.	97
Figure 63	Review of LIB Models: The Dual Polarization Model.	98
Figure 64	The second order electrical equivalent model of a PEM FC on the basis of electrochemical description.	99
Figure 65	Nyquist Plot for a MFC stack section.	100
Figure 66	Middlebrook's Extra Element System.	101
Figure 67	Modular fuel cell system connected with high-power energy storage devices and interfaced with bidirectional dc-dc converters.	102

Figure 68	Proposed synchronous multi-level high-gain bi-directional converter interfacing the high-power energy storage device with the load and the hybrid fuel cell stack section.	105
Figure 69	Proposed synchronous multi-level high-gain bi-directional dc-dc converter non-ideal gain compared to regular boost and regular buck-boost non-ideal gains. Design specs based on Section IV's design example.	107
Figure 70	Simulated output voltage/current waveforms of a single fuel cell section modularly interfaced with the proposed synchronous multi-level high-gain bi-directional dc-dc converter, sustaining a 7.5V output with a 100% load increase at $t = 1.5s$	108
Figure 71	Regular-Voltage Series Output MFC+HES Topology.	109
Figure 72	Hysteretic Control for the Multiport Conversion Stage of a 3-Level MFC+HES System.	110
Figure 73	90W/5A PEM MFC stack VI-characteristics.	111
Figure 74	MFC+HES inductor-current PI-control.	111
Figure 75	Single MFC Section Response to Instantaneous 300% Current Demand.	112
Figure 76	Type-3 output voltage control for the MFC+HES Modular Isolated Full-Bridge Converter Stage.	113
Figure 77	Dynamic Response of the MFC+HES Modular Isolated Full-Bridge Conversion Stage.	114
Figure 78	Fuel cell section modularly interfaced with a supercapacitor/Li-ion energy storage bank.	124
Figure 79	Total time-sustainable boost-current provision of a modular fuel cell section modularly interfaced with (a.) a supercapacitors only, (b.) a Li-Ion batteries only, and (c.) a hybrid combination of both (a.) and (b.).	129

LIST OF TABLES

	Page
Table 1	100W single-stage FC-PSC hardware verification for three power sharing cases: (i.) 100%/100%, (ii.) 50%/100%, and (iii.) 20%/80%. 39
Table 2	Switching states in T-type variant 3-level converter (x=a, b or c) 53
Table 3	System parameters for a 30kW online UPS 70
Table 4	Conventional and modular approach comparison 87
Table 5	Equivalent FC circuit values 100
Table 6	Benefits and acceptable trade-offs associated with choosing between A123's ANR26650M1-B 2.4Ah LIB and Maxwell's BCAP3000 3kF SC. 104

CHAPTER I

INTRODUCTION AND TOPICAL OVERVIEW

Market Relevance

Engineers, economists, government officials, and businessmen all around the world finally agree on something: energy is our future, and that future starts now. The International Energy Outlook expects world energy demands to grow 1.6% annually as the year 2035 approaches [1]. According to the US Energy Information Administration, in that same time period, the clean/renewable energy sector in the US is projected to grow annually three times faster than all other energy sectors at more than 3% [1]. These rapid growth statistics foreshadow a dependence on twice as many clean/renewable energy sources than exist presently.

Power Electronics and Distributed Energy Systems

In the midst of this global energy renaissance, power electronics has evolved into a top-tier technology discriminator in DERS. The integration of so many different types of DER technologies—each with its own strengths and weaknesses—proffers the unique opportunity to delve into the study of how this sundry assortment of devices can be best integrated per application. In response, this dissertation specifically explores how modern multiport and multilevel power conditioning technologies have evolved to more effectively integrate DER sources and storage. Relevant DER technologies are briefly introduced as to provide insight into utilizing power electronics to allow each's strengths

to negate one another's weaknesses, yielding better efficiencies and performance at lower costs. Finally, MPC research is reviewed in light of resource bundling DER technologies.

The Power Sharing Converter Family

Among the various DER MPCs discussed, first presented is a family of new multiport PSC topologies for utility-scale fuel cell power generation. The proposed system connects multiple fuel cell sources to a medium voltage grid via a single multilevel NPC inverter interface with high-frequency isolation. High voltage series-connected inputs are achieved, despite safely referencing each source to ground. Also, unique power sharing technology decouples series-connected source currents and enables control of each fuel cell's individual power level. Multi-dimensional modeling and analysis of the proposed system's PI- and PV-behavior is presented. Then, system topology and design considerations are discussed. Case study simulations show how this topology can operate four 250-kW fuel cells at separate power levels between 20% and 100%, while connecting to a single 3-level NPC utility-interface. Correspondingly, a reduced-scale hardware prototype provides further proof of concept. Altogether, the proposed family of multiport PSC topologies realize independent power control per source as well as increased output power, operational flexibility, thermal balancing, source availability, and cost-effectiveness for utility fuel cell power generation.

The Multi-Level Nine-Switch Converter

The next proposed DER MPC is the ML9SC. Here, a component-minimized multi-port converter features a design with low cost, high efficiency, high power quality, and low EMI characteristics. The multiport characteristic of the ML9SC can be effectively employed in the following applications: (a.) online UPSs, (b.) six-phase wind generators, and (c.) doubly-fed induction generator (DFIG) wind power systems. The operating principle and constraints on voltage and frequency of the dual outputs are detailed. Limits on the modulation index are also analyzed at different operating conditions. Loss breakdown is then analyzed and compared with the conventional back-to-back multi-level converter. Finally, simulation results are included in the summary to verify the validity of the proposed topology.

The Modular Fuel Cell with Hybrid Energy Storage Converter

The final DER MPC presented is the MFC+HES converter. Here, a unique multiport architecture modularly combines the slow, consistent power generation of a fuel cell with the quick-response, short-term power bursts of LIBs. This design is especially useful for UPSs, since it can continuously power a load while providing a near-instantaneous 300% boost current to the load for over 1 minute. Many benefits are realized, such as increased fault tolerance, limp-home capability, evenly distributed heat and aging, and maximized sectional power. Altogether, by introducing modular dc-dc converter interfacing with high-power HES, a fuel cell system can be tailored to provide time-sustainable responses to sudden high-power load demands.

CHAPTER II

POWER ELECTRONICS AND DISTRIBUTED ENERGY

Power electronics can be defined as the controlled processing of electrical energy via electronic components and devices [2]. There are three primary types of switching conversion: dc-dc, ac-dc, and ac-ac. Dc-dc converters either buck or boost a dc voltage and/or current to a lower or higher dc value, respectively. Ac-dc converters translate ac voltage and current into dc voltages and currents, and vice versa. A converter which operates in ac to dc conversion is generally called a rectifier, and a converter which operates in dc to ac conversion is commonly referred to as an inverter. Ac-ac converters—also called cycloconverters—adjust the magnitude and frequency of ac voltage and current from input to output. All three types of power conversion unavoidably require a control system to intelligently regulate input and output values.

Energy Electronics: A New Age

Traditionally, power electronics consisted of three fields of study: (1.) magnetics and power semi devices, (2.) electric circuits and machines, and (3.) controls. However, as noted by [3], power electronics has evolved into a top-tier technology discriminator—a system of technologies which is transcending many customary boundaries. The introduction of clean and renewable energy, smart-grids, smart-homes, electric transportation, energy harvesting, grid-connected systems, and data centers have required power electronics engineers to expand in expertise. New areas include, but are not limited

to, converter circuits, generation/storage devices, systems engineering, analog/digital/RF circuits, non-linear/linear control, and ICs and monolithic passives. Altogether, the discipline as a whole is expanding from the performance- and reliability-based nature of “power electronics” towards the sustainability- and system-of-systems-based nature of what some are beginning to dub “energy electronics.”

Distributed Energy Resource Systems

In order to understand the progression of research in literature and the significance of multiport power conversion, a moment is now taken to examine one of the primary impetuses for modern converter innovation—distributed energy resource systems. Many terms such as clean energy, green/renewable energy, and energy storage closely orbit the topic of DERS; however, a brief definition within the scope of this paper is hereby provided: integrated systems of “small, modular electricity-generating or storage technologies that are located close to the load they serve” [4]. There are three types of DER electrical sources discussed in this paper: Fuel Cells (FCs), Solar (PV), and Wind Turbine Generation (WTG). Similarly three types of DER electrical storage devices discussed in this paper are Flow Batteries (FBs), Lithium-Ion Batteries (LIBs), and Supercapacitors (SCs). Each is appropriately expounded upon in their respective chapters.

Multiport Converters and Resource Bundling

Faced with the formidable task of interfacing various types of DER technologies with the grid, research and industry have both acquired a naturally growing appetite for

multiport converter (MPC) design. This is primarily because MPC technology excels at simplifying the power conditioning process while improving source utilization [5-7]. MPC designs can be categorized according to three main characteristics: port placement (MISO, SIMO or MIMO), topology (series or parallel), and coupling (isolated or non-isolated) [7-16]. MPC research was initially oriented toward a wide array of lower-power applications, such as telecommunications [17] and micro-electronics [18], but has more recently expanded into higher-power applications such as EV/HEVs [19-21] as well as wind and solar electricity generating DERs [22-27]. Furthermore, the integration of electrical storage DERs introduces load-leveling and load-shifting capabilities and results in the following benefits: improved system efficiency, increased reliability, decreased grid stress, further improved source utilization, and significant financial savings. Therefore, this paper seeks to synthesize a more robust, efficient, and cost effective power conditioning systems by addressing the overlap between these two uniquely progressing topics of interest—MPCs and DERS.

CHAPTER III

THE POWER SHARING CONVERTER FAMILY

Introduction

As high-megawatt fuel cell power plants become more prevalent [28-33], this paper seeks to synthesize a more robust, efficient, and cost effective utility-scale power conditioning system by addressing the overlap between two uniquely progressing topics of interest—high-power MPCs and utility-scale FCs.

Conventionally, utility-scale FC power conditioning systems (see Figure 1) generally of three-stages: a DC-DC converter, a DC-AC NPC inverter, and a 60 Hz isolation transformer interface to electric utility grid [34, 35]. Here, each fuel cell stack requires its own converter using low frequency-isolation to interface with the utility grid, resulting in higher weight, volume, cost, and component count.

Faced with the formidable task of interfacing multiple clean and renewable energy technologies with the grid more effectively, research has acquired a naturally growing appetite for MPC design. This is primarily because MPC technology excels at simplifying the power conditioning process while improving source utilization [6, 7]. MPC research was initially oriented toward a wide array of lower-power applications, such as telecommunications [17], micro-electronics [18], and EV/HEVs [19-22], but has more recently expanded into higher-power applications, such as wind and solar [23-27, 36, 37].

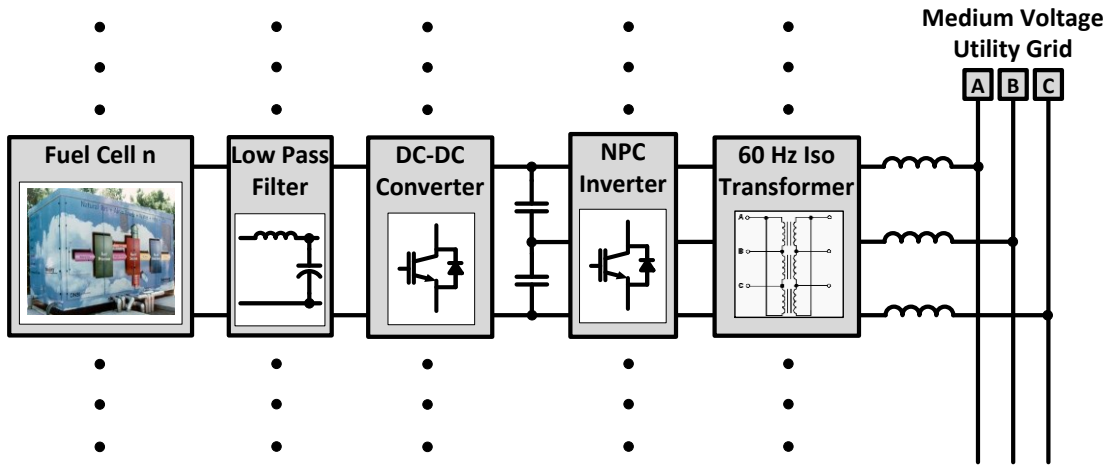


Figure 1. Conventionally, multiple utility-scale fuel cells are interfaced with a medium voltage utility grid via independent converter strings with bulky 60Hz isolation transformers.

MPC designs can be categorized by three main characteristics: port placement (MISO, SIMO or MIMO), topology (series or parallel), and coupling (isolated or non-isolated) [8, 10-16]. Topologically, a series-connection of sources is functional, but in most cases, more problematic. Firstly, current-coupling causes the source with the weakest current to limit the current of the entire string [38]. Secondly, dangerously high electrostatic potentials are often introduced to the sources [28]. Thirdly, voltage-sagging common in FCs and many other renewable sources puts excessive demand on converter designs [39]. Thus, parallel-connected topologies have been traditionally popular. For example, the time-sharing technique [5] and the multi-winding transformer flux additivity method [9] effectively utilize magnetic coupling to parallel-connect sources. Although they result in a reduction in the number of NPC inverters (see Figure 1) necessary to interface a multi-source system with the grid, such concepts do not necessarily reduce the

number of power conditioning converters between the source and the coupling transformer. Moreover higher currents in a parallel connected system compared to a series connected system may increase the conduction losses. Uniquely, the proposed Power Sharing Converter (PSC) technology presents a series-connected MPC solution which (a.) reduces input converter count, (b.) integrates into isolated system topologies (see Figure 2), and (c.) nullifies and/or mitigates the aforementioned short-comings associated series-connected sources. A fully-integrated PSC system can realize the following benefits:

- **Power Sharing:** source-currents are decoupled, such that each input can operate independently at any desired power level, allowing for thermal balancing.
- **Center Point Grounding:** DC-link voltages are doubled, while electrostatic potentials per input remain safely minimized.
- **HF Isolation DC-DC Conversion Stage:** two small HF transformers replace four bulky 60 Hz transformers; this stage strategically tolerates the voltage drooping of naturally saggy FC V-I curves and series-connected MPC technology.
- **Inherent MPC Benefits:** decreased grid stress and increased operational flexibility, availability, source utilization, and cost-effectiveness.

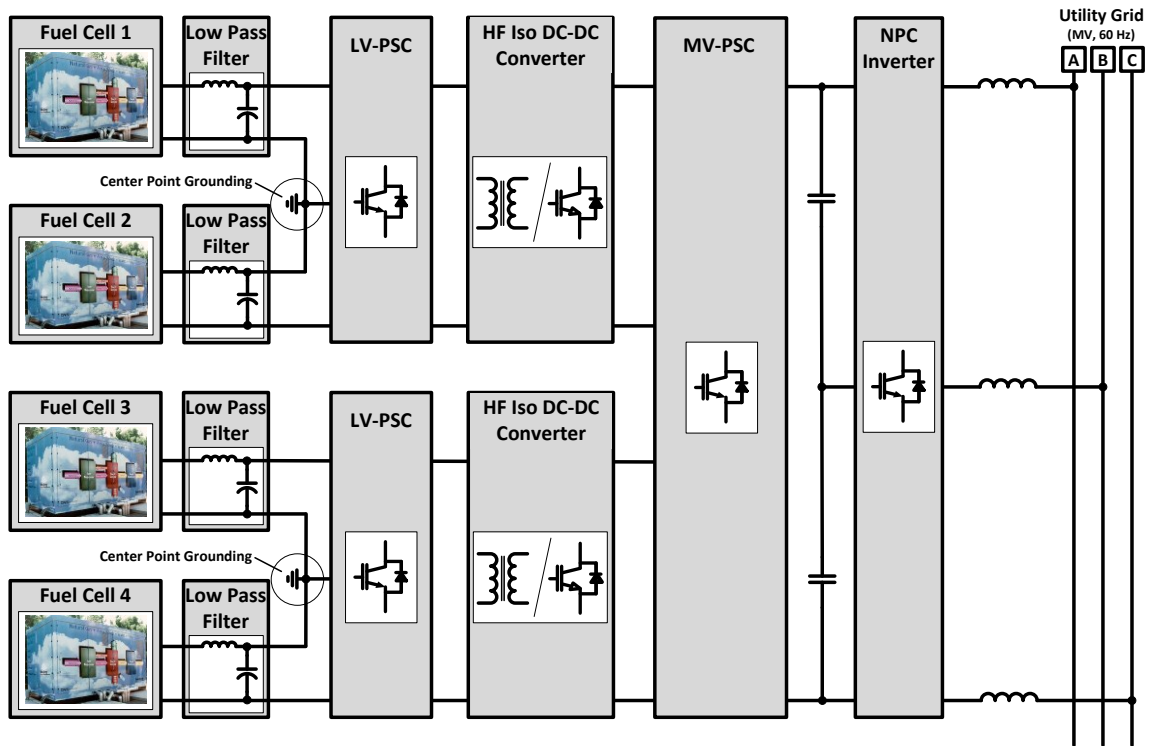


Figure 2. The proposed FC power conditioning architecture implements both Low Voltage- and Medium Voltage-Power Sharing Converter (LV/MV-PSC) topologies. By doing so, converter count and component count are reduced and the usage of large 60 Hz transformers is eliminated. Also, each fuel cell is capable of operating at independent power levels.

Proposed Power Sharing Converter Technology

Series-connected MPCs are desirable because higher input voltages translate into lower conduction losses and less stress from voltage-boosting. However, there are some negative trade-offs to consider. Namely, the coupling of source currents ($I_1=I_2$) and an increase in electrostatic stress across the sources. Fortunately, PSC technology addresses both concerns by decoupling source currents and grounding each input with Center Point Grounding (CPG). In this section, the two primary PSC architectures are introduced as

(a.) the Low Voltage-Power Sharing Converter (LV-PSC) and (b.) the Medium Voltage-Power Sharing Converter (MV-PSC).

The Low-Voltage Power Sharing Converter

The LV-PSC creates Power Sharing Zone α by interfacing two input sources with a single output via a half-bridge leg and a zonal inductor (L_α). When $S_{1\alpha}$ is activated, the zonal inductor sees $V_{1\alpha}$. Similarly when $S_{2\alpha}$ is activated, the zonal inductor sees $-V_{2\alpha}$. As illustrated in Figure 3, this will induce an excess dc-current ($I_{L\alpha}$) to flow through the zonal inductor when the power delivered by the first source ($P_{1\alpha}$) is not equivalent to the power delivered by the second ($P_{2\alpha}$).

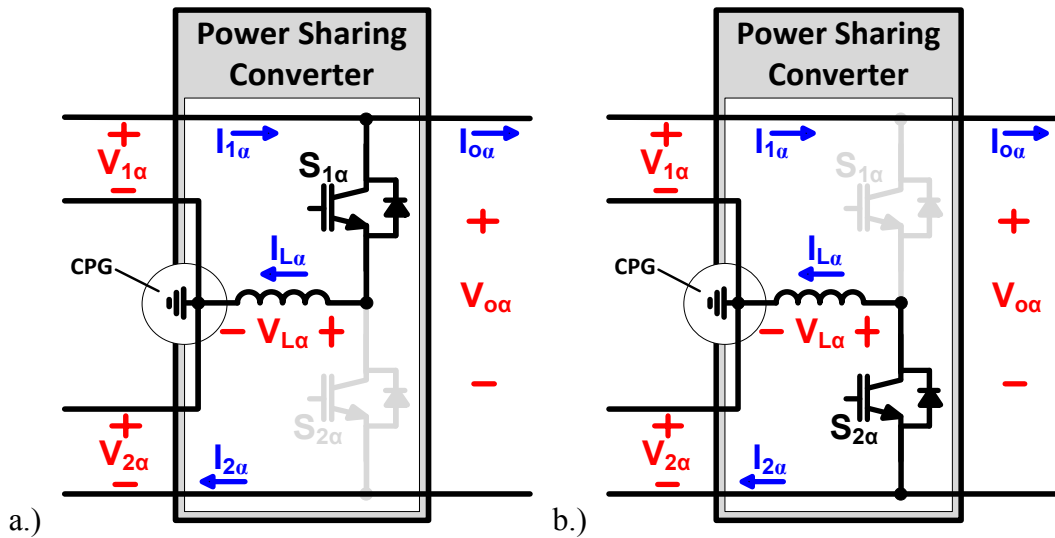


Figure 3. The proposed LV-PSC topology allows Source-1 α and Source-2 α to operate at unique power levels by switching between the two states illustrated in (a.) and (b.). For example, if $P_{1\alpha} > P_{2\alpha}$, then $I_{L\alpha} > 0$.

The steady state duty cycle for $S_{1\alpha}$ and $S_{2\alpha}$ can be written as

$$D_{1\alpha} = \frac{V_{2\alpha}}{V_{1\alpha} + V_{2\alpha}} = 1 - D_{2\alpha}, \quad (3.1)$$

and the zonal power sharing inductance value can be calculated as

$$L_{\alpha} = \frac{D_{1\alpha} \cdot V_{1\alpha}}{f_{sw} \cdot \Delta I_{L\alpha}}. \quad (3.2)$$

Although inspected in much greater detail in Section III, the general output current drawn from the LV-PSC is

$$I_{o\alpha} = \frac{V_{1\alpha} \cdot I_{1\alpha} + V_{2\alpha} \cdot I_{2\alpha}}{V_{1\alpha} + V_{2\alpha}}. \quad (3.3)$$

As an example, assume that $P_{1\alpha} > P_{2\alpha}$. In this case, the duty cycle $D_{1\alpha}$ must be increased to allow a positive DC current through the power sharing inductor ($I_{L\alpha} > 0$ in Figure 3). This balances the apparent current contribution between fuel cells, such that $I_{L\alpha} = I_{1\alpha} - I_{2\alpha}$. Eventually, $D_{1\alpha}$ will be slightly reduced to its appropriate steady state value ($D_{\alpha} > 50\%$) to compensate for a higher $V_{2\alpha}$ and maintain volt-second balance across the zonal power sharing inductor as seen in Figure 4.

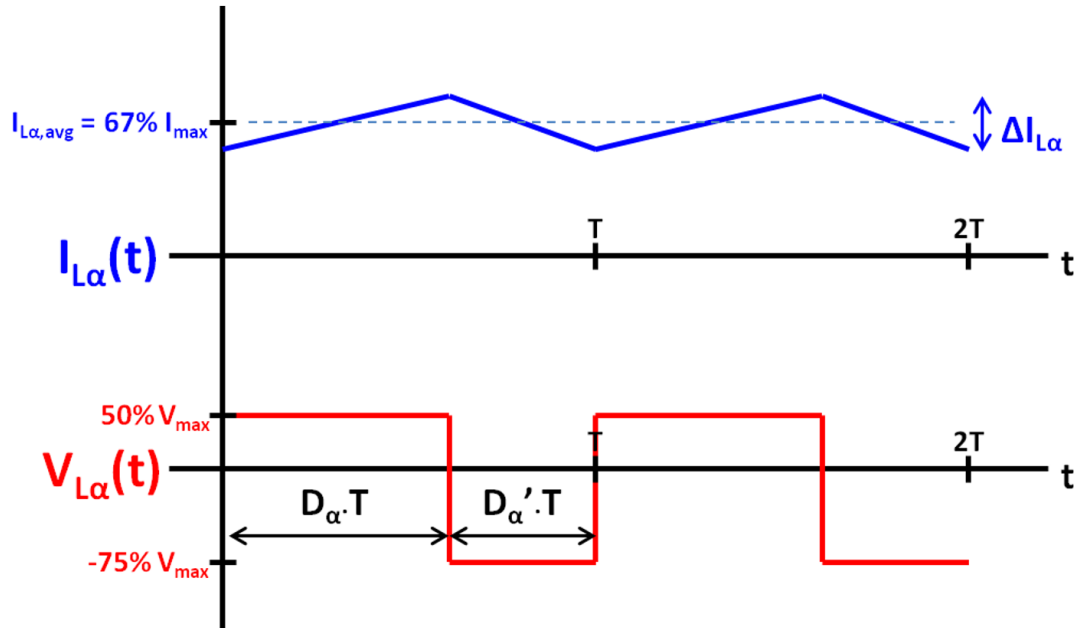


Figure 4. If $P_{1\alpha} > P_{2\alpha}$, $D_{1\alpha}$ increases and subsequently induces a positive steady state DC-current through the zonal power sharing inductor as shown by the voltage and current waveforms above.

Conclusively, it can be seen that the LV-PSC decouples source currents and relieves electrostatic stress with CPG. This allows a unique opportunity to safely control individual power contributions for series-connected sources.

The Medium-Voltage Power Sharing Converter

During higher voltage operation, the two half-bridge switches used in the LV-PSC may not be sufficiently rated. In such cases, the MV-PSC can be implemented. Not unlike an NPC chopper, the MV-PSC has a four-switch leg with diodes clamping each top and bottom switch-set to a neutral point. This effectively doubles the voltage tolerance from that of the LV-PSC by balancing the voltage stress across two inactive switches during either switching state. A significant addition to the NPC topology is the placement of a zonal power sharing inductor between the mid-leg zero voltage ac-output terminal and the neutral point. Similar to the LV-PSC, this inductor decouples the output currents of both HF Isolated DC-DC Converters ($I_{1\gamma}$ and $I_{2\gamma}$) as illustrated in Figure 5.

In the MV-PSC, two switching states are utilized. In State 1 (Figure 5a), $S_{1\gamma}$ and $S_{2\gamma}$ are turned on, allowing the top HFI DC-DC Converter's output voltage to be seen across the zonal inductor, such that $V_{L\gamma} = V_{1\gamma}$. In State 2 (Figure 5b), $S_{3\gamma}$ and $S_{4\gamma}$ are turned on, allowing the bottom HFI DC-DC Converter's output voltage to be seen across the zonal inductor, such that $V_{L\gamma} = -V_{2\gamma}$. The duty cycle and overall ideal operational characteristics mirror that of the LV-PSC. However, it is mandatory to note that $V_{1\gamma} = V_{2\gamma}$ at all times, lest a voltage stress imbalance be introduced among inactive switches. This constraint is tolerable since HFI DC-DC Converters precede the MV-PSC in the grid level connection and can equalize the MV-PSC's input voltages.

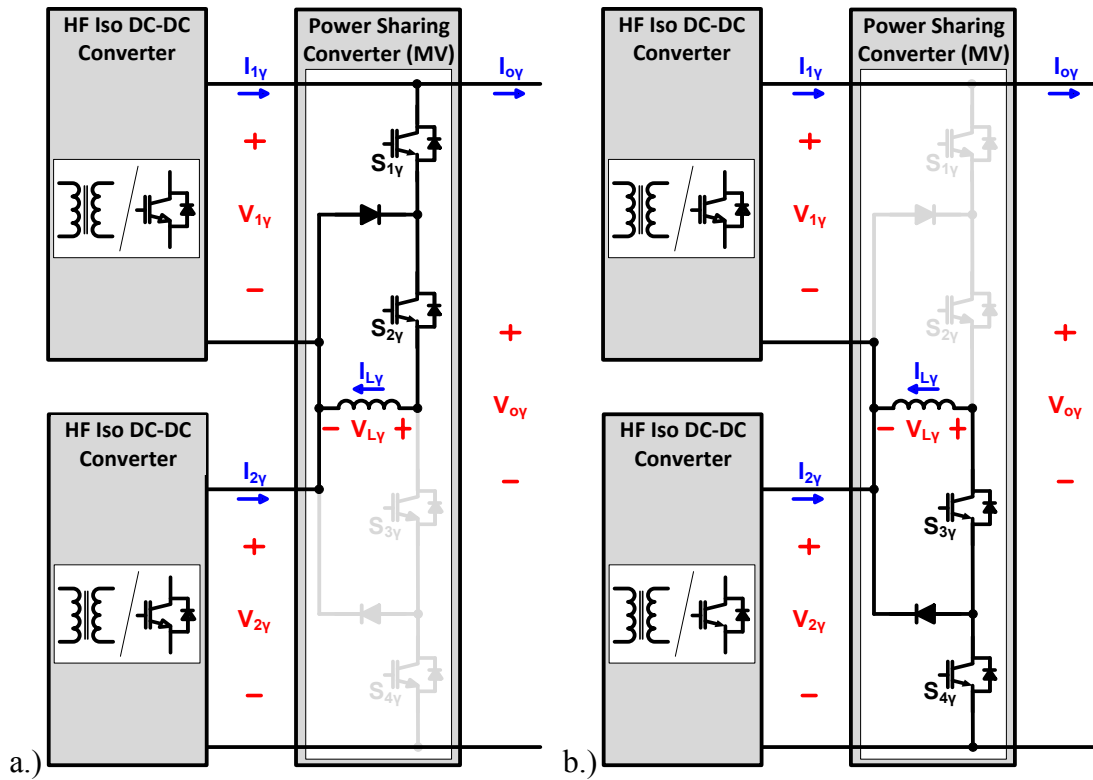


Figure 5. The proposed MV-PSC decouples $P_{1\gamma}$ and $P_{2\gamma}$ at higher voltages by switching between the two states illustrated in (a.) and (b.). The clamping diodes help balance voltages across $S_{1\gamma}$ and $S_{2\gamma}$ or $S_{3\gamma}$ and $S_{4\gamma}$, while the HF Isolated DC-DC Converters hold $V_{1\gamma} = V_{2\gamma}$.

The Fuel Cell and the Power Sharing Converter

Many of the benefits of PSC technology synergize with fuel cell characteristics. Here, the modeling and behavior of the two in tandem is explored.

Synergistic Benefits

When applying PSC technology to FCs, it is imperative to consider FC VI-curve characteristics. As to remain within scope, this paper models fuel cells as voltage sources with linear dependency upon current discharge. Figure 6 and Equations 3.4 and 3.5 describe how the normalized fuel cell voltage and current are then modeled in relation to normalized power operating points.

$$V_{FC,n} = \frac{V_{FC}}{V_{max}} = 1 - 0.5 \cdot P_{FC,n} \quad (3.4)$$

$$I_{FC,n} = \frac{I_{FC}}{I_{max}} = \frac{P_{FC,n}}{2 - P_{FC,n}} \quad (3.5)$$

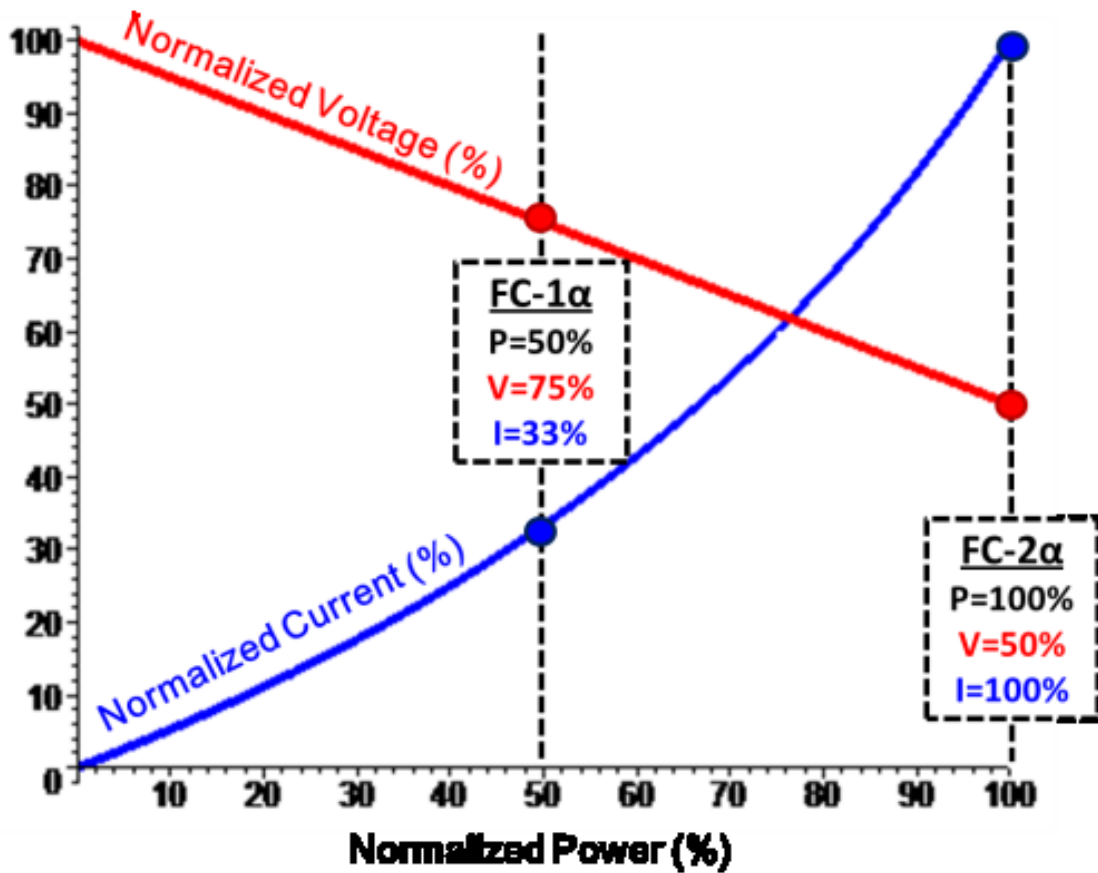


Figure 6. Linear current dependency characterizes the fuel cell's PV-curve (red) and produces the resulting PI-curve (blue). Two potential power points (50% and 100%) are noted in order to inspect the case where $P_{1\alpha} > P_{2\alpha}$.

A single fuel cell produces approximately 0.6 V at full load; thus, they are typically stacked in series in order to obtain higher voltages. These stack voltages are limited by their electrostatic potential with respect to ground [38], thus keeping utility-scale fuel cell (as well as series-connections of fuel cells) under 1 kV [40]. By grounding mid-point of two series-connected FC stacks, the PSC's CPG allows this limit to effectively double.

It is also significant to note, that when fuel cells are stacked in series, their operating points are coupled since each stack must operate at the same current level. Inevitably, the “weaker” FC will heat up more and progressively age faster than a “stronger.” However, PSC technology decouples each stack, which effectively translates into power-, thermal-, and age-balancing [38].

The PSC topology in Figure 7 features a CPG tap, current decoupling, and protective low-pass filters for each FC. The center-point ground is set between the stacks to lower the overall electrostatic potential seen at the terminal of the fuel cells with respect to the ground, and thus it reduces safety risks and potential damage in the case of a fault. Low-pass filters protect the fuel cells from deleterious HF current ripples created by PSC switching, consequently increasing unit performance and lifetime. (FC filter design is discussed in greater depth later in this paper.) Altogether the PSC decouples FC power characteristics and current limitations, allowing the option of running each fuel cell at an optimum power point such that the thermal and electrical stress between the fuel cell stacks is balanced.

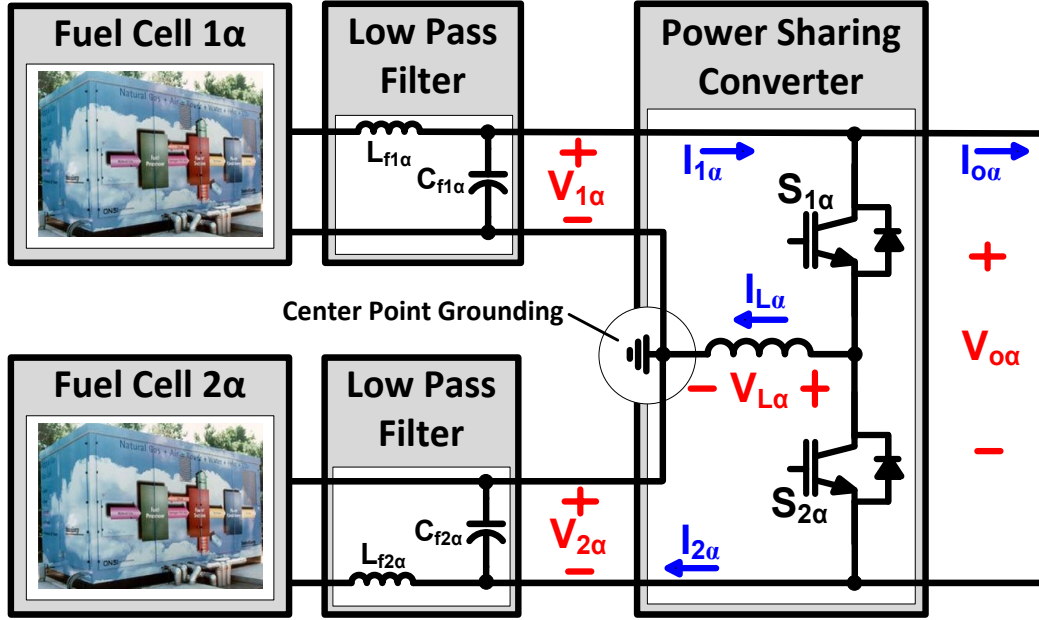


Figure 7. The proposed LV-PSC topology allows FC-1 α and FC-2 α to operate at unique power levels. For example, if $P_{1\alpha} > P_{2\alpha}$, then $I_{L\alpha} > 0$.

Modeling System Behavior

The PSC's three-port power transfer is a multi-dimensional concept, which should be clarified via closer inspection and modeling. The equation below governs the relationships between the PSC's output power and its input sources.

$$P_o = D_1 \cdot [P_2 + V_1 I_2] + D_2 \cdot [P_1 + V_2 I_1] \quad (3.6)$$

In an effort to gain deeper insight into what this relationship looks like when both sources are fuel cells, both sources are modeled according to the following linear-VI equation

$$V_i = R_i \cdot I_i + V_{max,i} \quad (3.7)$$

where

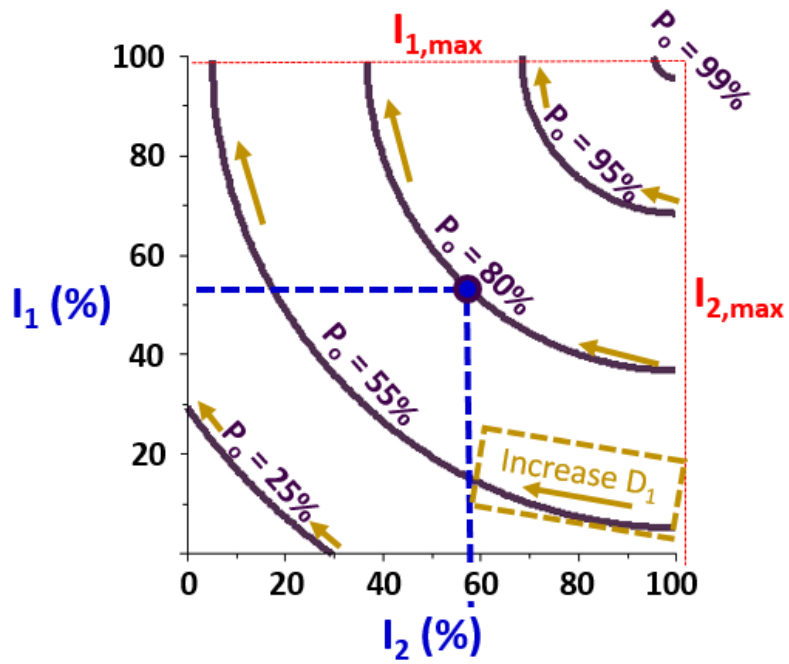
$$R_i = \frac{V_{max,i} - V_{min,i}}{I_{max,i} - I_{min,i}} \quad (3.8)$$

represents the sagging slope of the voltage as current is discharged from a fuel cell. After this model is implemented, the input currents and input voltages are inspected during constant output power scenarios in order to gain insight into the basic operational characteristics of the FC-PSC.

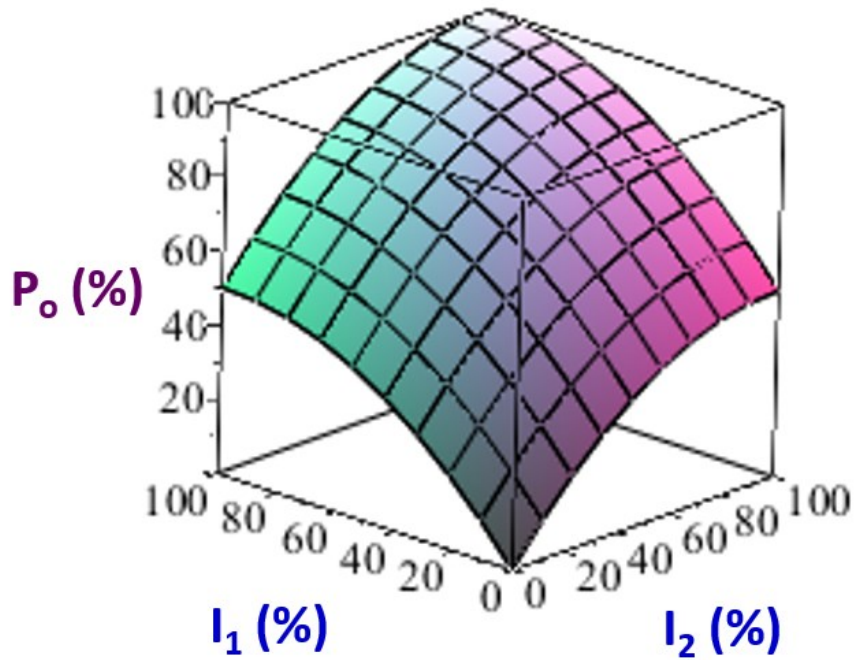
The correlation between the input currents of the fuel cells and the output power of the PSC is first examined. Holding the output power constant, the following equation holds true:

$$P_o = [R_1] \cdot I_1^2 + [V_{max1}] \cdot I_1 \\ + [R_2] \cdot I_2^2 + [V_{max2}] \cdot I_2. \quad (3.9)$$

Figure 8 graphically illustrates the multi-dimensional relationship between the fuel cell currents and the output power as described in the preceding equation.



a.)



b.)

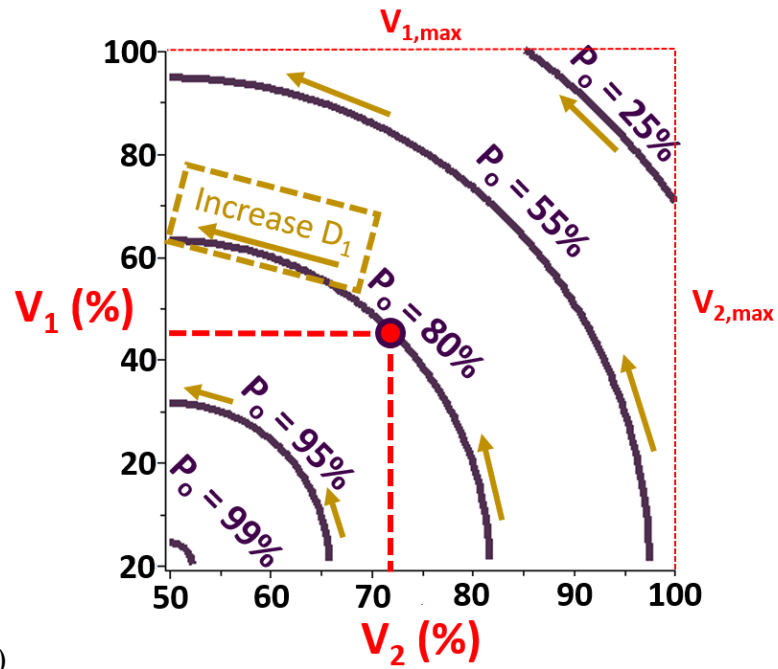
Figure 8. The plots above illustrate the relationship between FC input currents (I_1 and I_2) and PSC output power (P_o) in (a.) 2-d and (b.) 3-d. Golden arrows are used to show how increasing D_1 can adjust the ratio of I_1 to I_2 while maintaining a constant output power.

Similarly, the association between the fuel cell voltages and the PSC output power can also be analyzed. At a constant output power, the fuel cell voltages will obey the following equation:

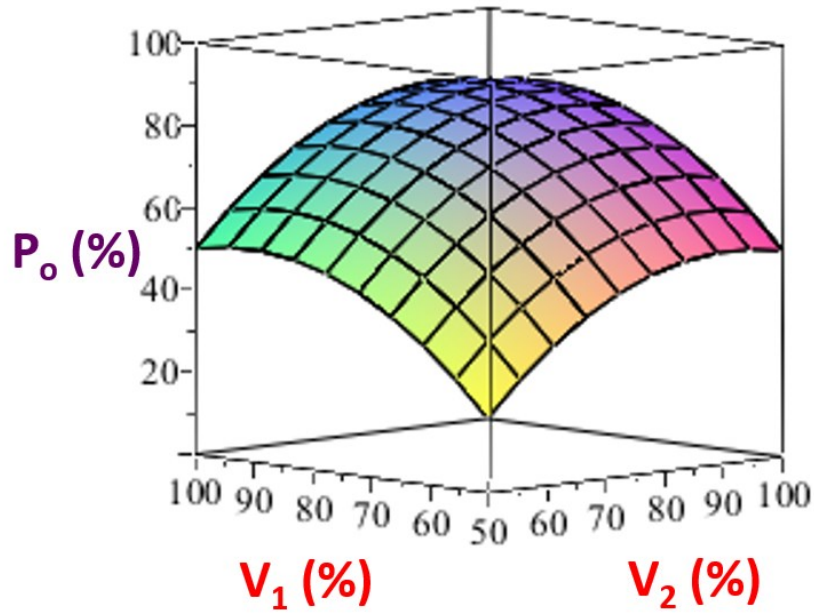
$$P_o = \left[\frac{1}{R_1} \right] \cdot V_1^2 + \left[\frac{-V_{max1}}{R_1} \right] \cdot V_1 \quad (3.10)$$

$$+ \left[\frac{1}{R_2} \right] \cdot V_2^2 + \left[\frac{-V_{max2}}{R_2} \right] \cdot V_2.$$

Again, Figure 9 shows the multi-dimensional relationship between the fuel cell voltages and the PSC output power accordingly. The first image shows a two-dimensional cross section, where the duty cycle is shown to influence the voltage ratio between sources. The second image illustrates the three dimension plane created by varying output power with the two input voltages.



a.)



b.)

Figure 9. The plots above illustrate the relationship between FC input voltages (V_1 and V_2) and PSC output power (P_o) in (a.) 2-d and (b.) 3-d. Golden arrows are used to show how increasing D_1 can adjust the ratio of V_1 to V_2 while maintaining a constant output power.

It is significant to note that both the images in Figure 8 and Figure 9 assume that the linear characteristic for both fuel cells is equal. In other words, $V_1 = V_2$, $R_1 = R_2$, and $V_{\max 1} = V_{\max 2}$ have been chosen as a case example only. If the fuel cell characteristics become incongruent, the PI- and PV-graphs should be re-plotted from Equations 3.9 and 3.10 respectively, thereby displaying an appropriate elliptical distortion to the current images.

Conclusively, this section models the PI- and PV-behaviors of a FC-PSC system with a constant output power. By examining the FC currents (I_1 and I_2) and FC voltages (V_1 and V_2) at layers of constant output powers (P_o), insight can be gained regarding the following:

- Input power (P_1 and P_2) control
- Input power ratio (P_1/P_2) optimization
- Path optimization for front- or load-end power transitions.

Proposed Fuel Cell Power Sharing Converter Grid Connection Topologies

A family of multiport FC-PSCs are hereby proposed in (a.) single-zone, (b.) dual-zone, and (c.) multi-zone topologies.

Single-Zone FC-PSC Topology

The first arrangement, a single-zone topology, allows for individual power control of two fuel cells and is illustrated in Figure 10. Here, a LV-PSC zone is connected to a DC/DC converter with HF isolation. Adding isolation at this point removes the need for

the conventional bulky 60 Hz isolation transformer. The output of the DC/DC converter is then interfaced with an NPC inverter, which offers the following benefits: reduced switching and conduction losses, mitigated output current ripple, and the removal of DC link capacitor leakage compensation problems. Size and cost of the final stage's NPC inverter is reduced by spreading the system gain over multiple stages, allowing for medium voltage interfacing. Furthermore, the insertion of a middle stage decouples multiple control variables, thus reducing overall system control complexity.

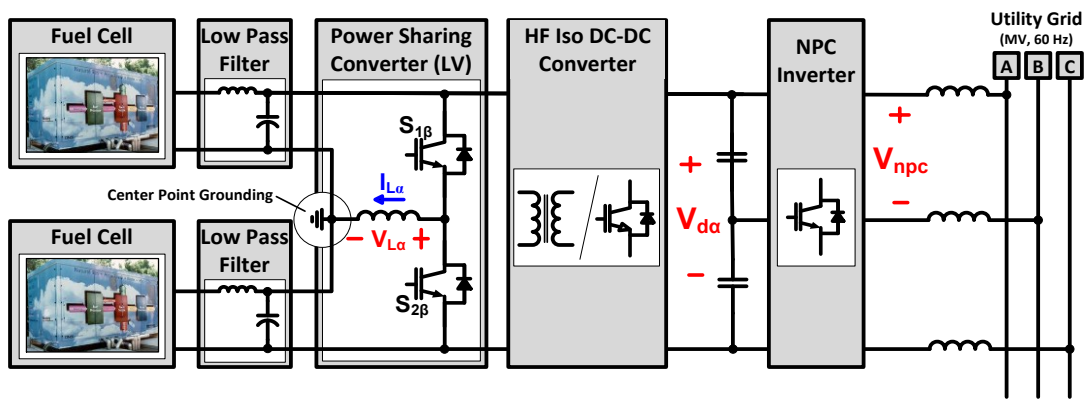


Figure 10. The proposed Single-Zone FC-PSC topology provides HF isolation while allowing each fuel cell unit (FC-1 α and FC-2 α) to operate at unique power levels and interface with a medium-voltage three-phase 60 Hz utility grid.

Dual-Zone FC-PSC Topology

The dual-zone (see Figure 11) and multi-zone (see Figure 12) FC-PSC topologies both allow independent power control of four fuel cell units. Similar to the single-zone FC-PSC topology, both arrangements feed two LV-PSCs into two respective DC-DC

converters with HF frequency isolation, once again removing the need for the conventional bulky 60 Hz isolation transformers. The DC/DC converter outputs from each zone are then stacked.

The dual-zone FC-PSC topology in Figure 11 allows for a wide differential in DC/DC converter output voltages while still enabling power sharing between the zonal outputs to the NPC inverter. When connecting the NPC inverter output to the utility grid, V_{NPC} represents the line-to-line medium voltage. The minimum DC link voltage (V_{DC}) required to generate V_{NPC} is described by

$$V_{DC} = \frac{2\sqrt{2} \cdot V_{NPC}}{\sqrt{3} \cdot m_a} \quad (3.11)$$

where m_a is the modulation index. This V_{DC} is created by the summation of the zonal DC/DC converter output voltages ($V_{DC\alpha}$ and $V_{DC\beta}$), such that

$$V_{DC} = V_{DC\alpha} + V_{DC\beta}. \quad (3.12)$$

Because of the series connection between $V_{DC\alpha}$ and $V_{DC\beta}$, the DC output current must be the same. If there is a case where the output power provided by the two zonal DC/DC converters are not equivalent, and then power balancing must be managed by adjusting $V_{DC\alpha}$ and $V_{DC\beta}$ with respect to Equations 3.11, 3.12, and 3.13.

$$\frac{V_{DC\alpha}}{V_{DC\beta}} = \frac{V_{FC1\alpha} \cdot I_{FC1\alpha} + V_{FC2\alpha} \cdot I_{FC2\alpha}}{V_{FC1\beta} \cdot I_{FC1\beta} + V_{FC2\beta} \cdot I_{FC2\beta}} \quad (3.13)$$

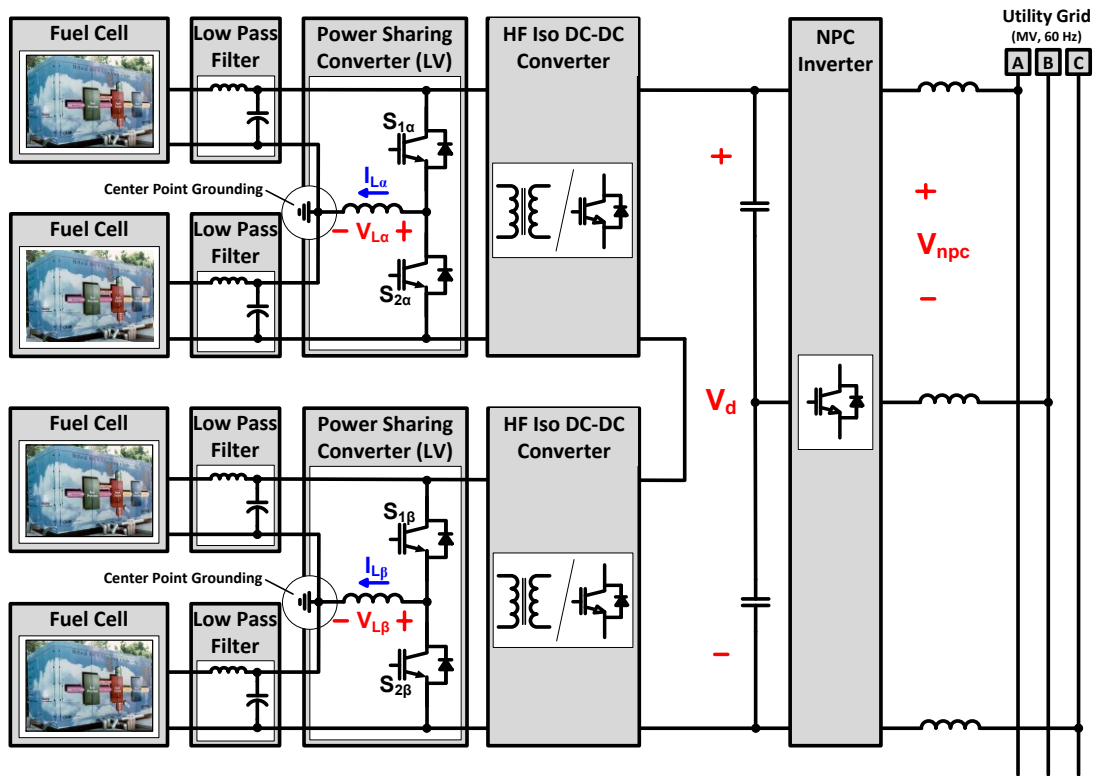


Figure 11. The proposed Dual-Zone FC-PSC topology permits each fuel cell unit (FC₁, FC₂, FC₃, and FC₄) to operate at a unique power level and interface with a medium-voltage three-phase utility grid, while allowing a variable-voltage power sharing between the DC/DC converter outputs.

With both the single- and dual-zone FC-PSC topologies, power sharing between the DC/DC converter outputs is achieved without requiring additional components. At the same time, the ratio between the DC/DC converter output voltages must be limited in order to avoid excessive device overrating. Also, the transformer turns ratio has to be large enough to satisfy the control scheme, as will be discussed later in this paper.

Multi-Zone PSC Topology

The multi-zone FC-PSC topology in Figure 12 is similar to the dual-zone FC-PSC presented in the previous section; however, an MV-PSC is introduced at the DC link between the zonal DC/DC converter outputs and the NPC inverter input. The MV-PSC decouples the DC/DC Converter output currents in the same way as the LV-PSC, but due to the presence of the diode-clamped structure with four IGBTs, the power sharing can occur at a large DC link voltage. In this case, Equations 3.11 and 3.12 still hold true. However, because of the MV-PSC there are no additional constraints in terms of voltages, and so $V_{DC\alpha}$ and $V_{DC\beta}$ can be adjusted to optimize device utilization.

With this topology, the DC/DC converter of the FC-PSC zone with the lowest power can be assigned with the burden of providing the higher DC/DC converter output voltage. This takes advantage of the voltage drooping characteristic of fuel cells with respect to power. One possible MV-PSC control strategy is to maintain a proportionality between the ratio of the DC/DC converter output voltages, such that

$$\frac{V_{DC\alpha}}{V_{DC\beta}} = \frac{V_{FC1\alpha} + V_{FC2\alpha}}{V_{FC1\beta} + V_{FC2\beta}}. \quad (3.14)$$

Altogether, the multi-zone FC-PSC topology offers a greater flexibility in the control strategy and subsequently improves the performance of the zonal DC/DC converters. The only disadvantage to this approach is that it requires more components, possibly influencing system reliability.

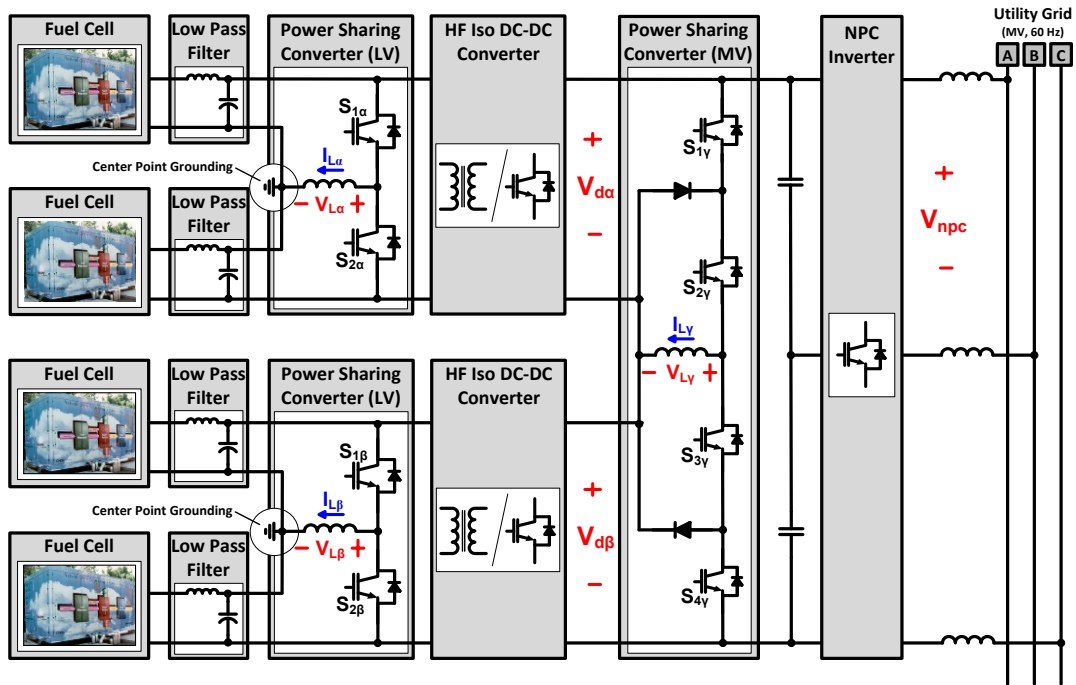


Figure 12. The proposed Multi-Zone FC-PSC topology permits each fuel cell unit (FC₁, FC₂, FC₃, and FC₄) to operate at a unique power level and interface with a medium-voltage three-phase utility grid, while introducing new control strategy flexibilities.

Fuel Cell Power Sharing Converter Design Considerations

When implementing any of the aforementioned topologies, specific attention should be directed towards the design of each of the following: FC filter stages, HF transformers, full-bridge converters, and overall system control, protection, and efficiency.

Filter Design

Ripple current from high frequency switching can be extremely deleterious to fuel cell lifetime; therefore, a low-pass filter is applied to each stack for unit protection. In order to design the filter, the equivalent circuit in Figure 13 is considered. $I_{FC-1\alpha,ripple}$ is the ripple current ($I_{FC-1\alpha} - I_{FC-1\alpha,avg}$), which will flow through the source $FC-1\alpha$ if no filter is applied. After applying a filter, $I_{Lf1\alpha,ripple}$ denotes the ripple current that flows through the filter inductor into the source $FC-1\alpha$. From Equations 3.15, 3.16 and 3.17, the appropriate filter inductance and capacitance values can be chosen.

$$I_{Lf1\alpha,ripple} = 0.05 \cdot I_{FC1\alpha,ripple} \quad (3.15)$$

where

$$|I_{FC1\alpha,ripple}| = 0.5 \cdot I_{max} = 0.5 \text{ p.u.} \quad (3.16)$$

From **Figure 13**, the transfer function can be written as

$$I_{Lf1\alpha,ripple} \leq \left| \frac{0.5 * 0.05}{1 - \omega^2 LC} \right| \text{ p.u.} \quad (3.17)$$

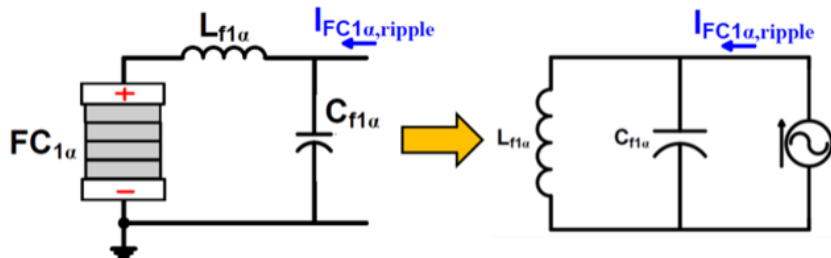


Figure 13. Fuel cell filter circuit and AC equivalent used for filter design.

PSIM was used to simulate a single-zone FC-PSC topology, in which a switching frequency of 20 kHz was utilized. Thus, filter values of $L_{f1\alpha} = 100 \mu\text{H}$ and $C_{f1\alpha} = 10\mu\text{F}$ were selected. Figure 14 shows the resulting current waveforms with and without the filter. It can be seen that $I_{FC-1\alpha}$ (unfiltered current) has large ripples, whereas $I_{FC-1\alpha,avg}$ (filtered source current) is almost ripple free.

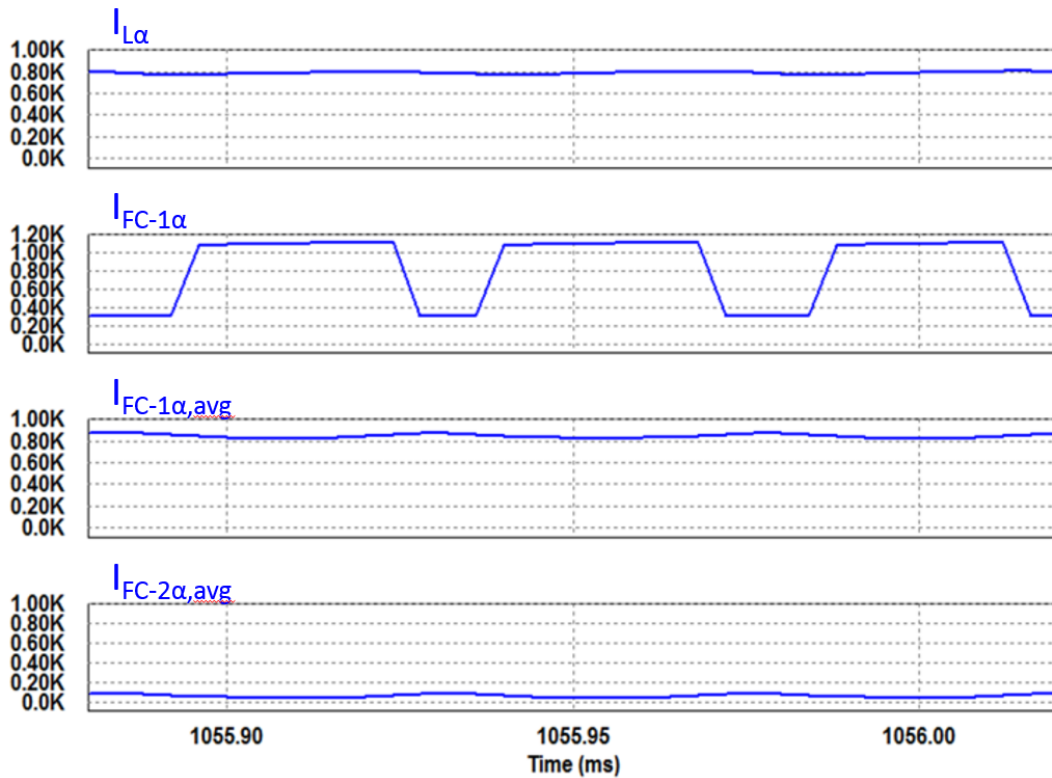


Figure 14. PSIM simulation of a single-zone FC-PSC topology where $P_{FC-1\alpha} = 100\%$ and $P_{FC-2\alpha} = 10\%$, displaying: (i.) the power sharing inductor current $I_{L\alpha}$, (ii.) the unfiltered current $I_{FC-1\alpha}$ with large ripples, (iii.) filtered source current $I_{FC-1\alpha,avg}$ with small ripples, and (iv.) filtered source current $I_{FC-2\alpha,avg}$ with small ripples.

Transformer Design

The transformer design depends on the topology that is used for the utility integration. This section provides the design of the transformer for both dual- and multi-zone systems (based on Figure 11 and Figure 12). Because the transformer only sees a high frequency square wave, the generic transformer VA rating is described by Equation 3.18.

$$VA_{rating} = \frac{V_{1,max}I_{1,max} + V_{2,max}I_{2,max}}{2} \quad (3.18)$$

where $V_{1,max}$ and $I_{1,max}$ are the peak primary voltage and current, and $V_{2,max}$ and $I_{2,max}$ are the peak secondary voltage and current.

Case. 1- Dual-Zone FC-PSC

Assuming that the full load voltage and full load power is 1.0 p.u, it is possible that the no load voltage can go as high as 2.0 p.u. This makes the maximum current 1.0 p.u. For the secondary side power rating, it is necessary to decide how much of a variation can be tolerated in the power generated by the two zones in order to maintain appropriate power balancing at the output. Therefore, let $r:1$ ($r > 1$) be the maximum ratio that can be accommodated in the design. For this case, the maximum DC link voltage ratio now will follow Equation 3.19, depending on which zone is delivering more power.

$$\frac{V_{DC\alpha}}{V_{DC\beta}} = \frac{r}{1} \text{ or } \frac{1}{r} \quad (3.19)$$

The transformer turns ratio is now given by Equation 3.11 and 3.20.

$$N = \frac{r \cdot V_{DC}}{(r+1) \cdot V_{Z,min}} \quad (3.20)$$

Here, $V_{Z,min}$ is the minimum zonal voltage at the transformer. Because of the design, the VA rating of the transformer secondary now has to be increased by a factor of $(r-1/r+1)$. So, the net VA rating of the transformer reduces to Equation 3.21.

$$VA_{rating} = \left\{ 1.0 + \left(\frac{r}{r+1} \right) \right\} p.u \quad (3.21)$$

For example, if the fuel cells have to be interfaced to a 2300V medium voltage utility grid, minimum VDC should be 3.8kV. If the minimum zonal voltage at fuel cell stack is 600V (at full power) and the maximum ratio is fixed as $r = 2$, then the turns-ratio will be $N \approx 4.25$ and the VA rating of the transformer will be 1.66 p.u.

Case. 2- Multi-Zone FC-PSC

With the MV-PSC, the DC link voltage ratio does not need to follow the ratio $r:1$ ($r > 1$), as in previous case. In order to make optimum use of devices, the value of r has to be 1 in Equations 3.20 and 3.21. The duty cycle of the DC-DC converter can be adjusted for varying zonal voltages in order to regulate $V_{DC\alpha} = V_{DC\beta} = V_{DC}/2$. For the same problem statement discussed under Case 1, the turns-ratio of the transformer will now be $N \approx 3.2$ and the VA rating will be 1.5 p.u. Both the turns-ratio and VA rating are smaller than those in Case 1. Altogether, this topology offers more flexibility in design, but adds more circuitry and components to the MV-PSC power sharing stage. Nonetheless, the VA rating still appears to be large because of the fuel cell PV-characteristic.

IGBT-based DC-DC Full-bridge Converter Design

The isolated full-bridge converter is a very popular DC-DC converter topology used for grid integration of various energy sources. In this paper, such a converter is used (with high frequency transformer isolation) to boost the fuel cell voltages to the required DC link voltage level [41]. As the voltages at the primary sides of the transformers are within 1200V, conventional 1700V IGBTs can be employed; aided by the fuel cell PV-characteristic that when voltage is high, current is low and stress on the devices is low. The secondary sides of the transformers have diode full bridges. 4.5kV fast diodes can be used for this application. Variable DC-link voltages can be achieved by adjusting the duty cycle of the IGBT full bridge.

System Control, Protection, and Efficiency

As observed in [42], the controller for series-connected power conversion modules must (a.) carefully balance the voltages across the DC-link capacitors (e.g., in the dual-zone PSC topology) and (b.) fault identification and thyristor-based module bypass capabilities. Furthermore, phase-shifting between the two DC-DC converters' modulation (see Figure 12) reduces the DC output voltage ripple.

PSC technology introduces many benefits as far as efficiency is concerned. Due to the series-connected input, the current is halved on the primary side of the IGBT full-bridge converter when compared to a conventional system, thus reducing the conduction losses. Similarly, a higher dc-link voltage reduces conduction losses for the NPC inverter

in the proposed systems (see Figure 10 - Figure 12) compared to the conventional system in Figure 1. It is important to note that compared to the conventional system, the proposed system will incur slightly higher losses due to the additional PSC stage. Nonetheless, the reduction in the conduction losses in the rest of the system will offset this loss to an extent. At the same time, the flexibility of operation of the FC stacks brought in by the PSC improves the system availability compared to a typical series connected structure, since each FC can now work uninterrupted under different operating conditions.

Simulation Results

A 1MW Dual-Zone FC-PSC (see Figure 11) is simulated in PSIM for a 2.3kV medium voltage utility interface, and the results are shown in Figure 15. Here, a maximum power level of 250kW is chosen for each source; $P_{FC-1\alpha}$, $P_{FC-2\alpha}$, $P_{FC-1\beta}$, and $P_{FC-2\beta}$ are arbitrarily chosen to operate at 100%, 20%, 32%, and 48% (see Figure 16). It is evident that the output voltages of the DC/DC converters ($V_{DC\alpha}$ and $V_{DC\beta}$) sum to the required DC-link voltage ($V_{DC} = 3.8kV$) at the input of the NPC inverter, and the ratio between DC-link voltages $V_{DC\alpha}$ and $V_{DC\beta}$ follows Equation 3.13. Also, power sharing through each zonal inductor is verified by the display of the appropriate zonal inductor current directions and magnitudes. Note that the polarity properly indicates that $P_{FC-1\alpha} > P_{FC-2\alpha}$ and $P_{FC-1\beta} < P_{FC-2\beta}$.

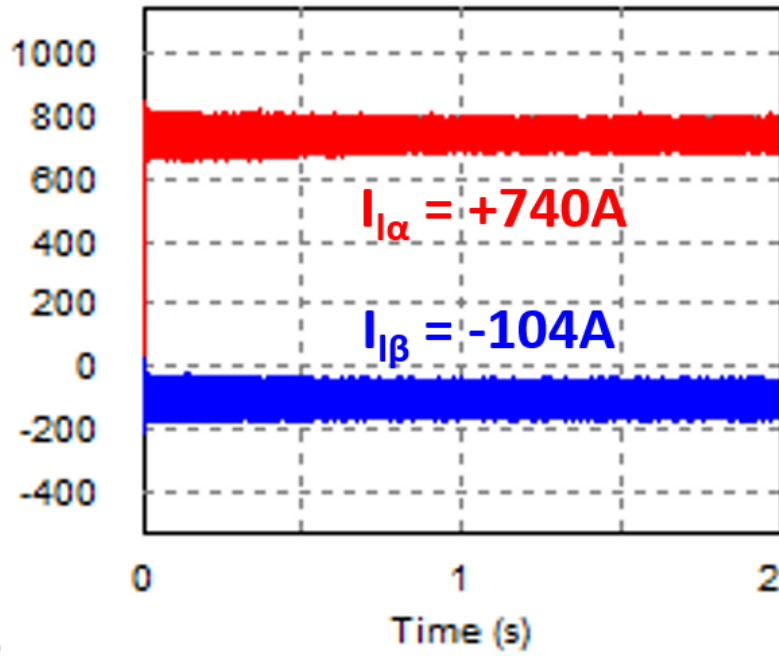
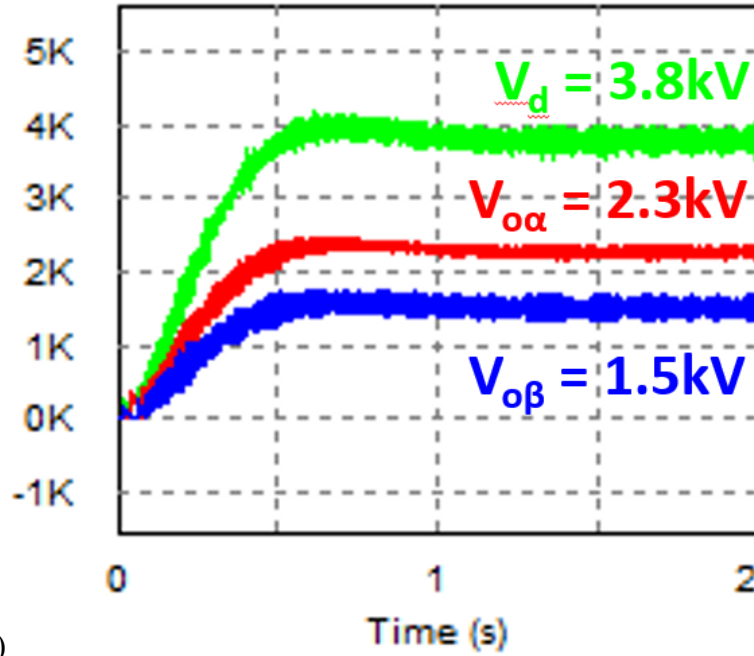


Figure 15. Simulation results for design example power levels: $P_{FC-1\alpha} = 250$ kW, $P_{FC-2\alpha} = 50$ kW, $P_{FC-1\beta} = 80$ kW, and $P_{FC-2\beta} = 120$ kW. Verifies zone DC-DC converter output voltage balancing ($V_{o\alpha} + V_{o\beta} = V_d$) as well as zone inductor current dependence on varying individual fuel cell power levels.

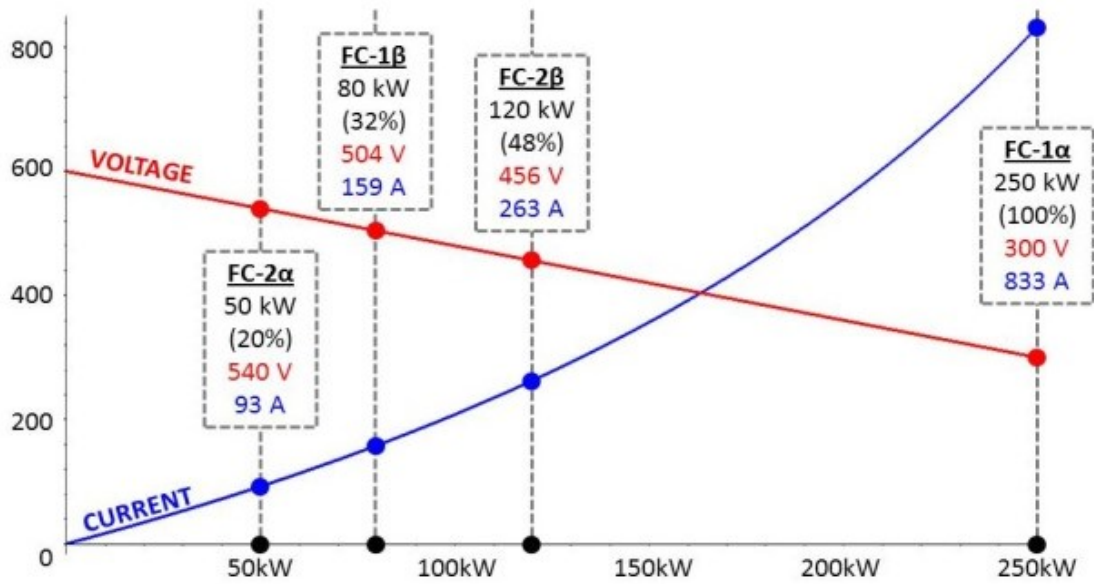


Figure 16. The fuel cell power operation points $P_{FC-1\alpha} = 100\%$, $P_{FC-2\alpha} = 20\%$, $P_{FC-1\beta} = 32\%$, and $P_{FC-2\beta} = 48\%$ are arbitrarily chosen, yielding the above voltage and current characteristic values.

Experimental Results

A laboratory prototype was constructed to verify the design and control of the single-zone PSC. The circuit in Figure 7 is first built with two IGBTs and a 0.1 mH zonal power sharing inductor. Two LC-filters with the following values are then applied to the sources: $L_{f1\alpha} = L_{f2\alpha} = 100 \mu\text{H}$ and $C_{f1\alpha} = C_{f2\alpha} = 10 \mu\text{F}$. Figure 17 illustrates how the Texas Instruments TMS320F28035 microcontroller is then used to control the current flow through the zonal power sharing inductor (of 220 μH) at a switching frequency of 20 kHz. Here, it can be seen that the zonal inductor current (blue) follows the manually adjusted reference signal (yellow) between Operating Extrema #1 ($P_1=100\%/P_2=20\%$) and Operating Extrema #2 ($P_1=100\%/P_2=20\%$). Thus, verifying a wide range of system

operation as well as bidirectional current flow capability through the power sharing inductor.

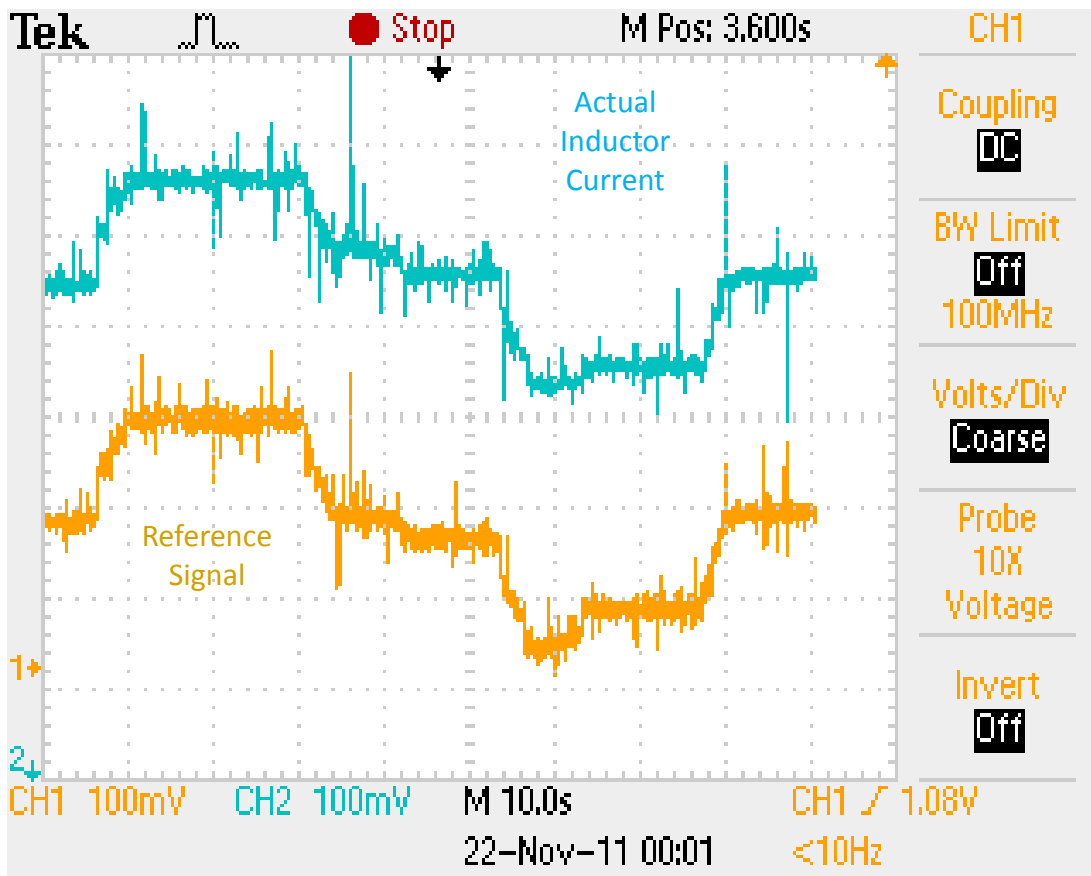


Figure 17. The power sharing inductor current (blue) directly follows manual adjustments in the control reference signal (yellow), illustrating system capacity for bidirectional inductor current flow during power sharing between sources. (Note: 1 division = 5A.)

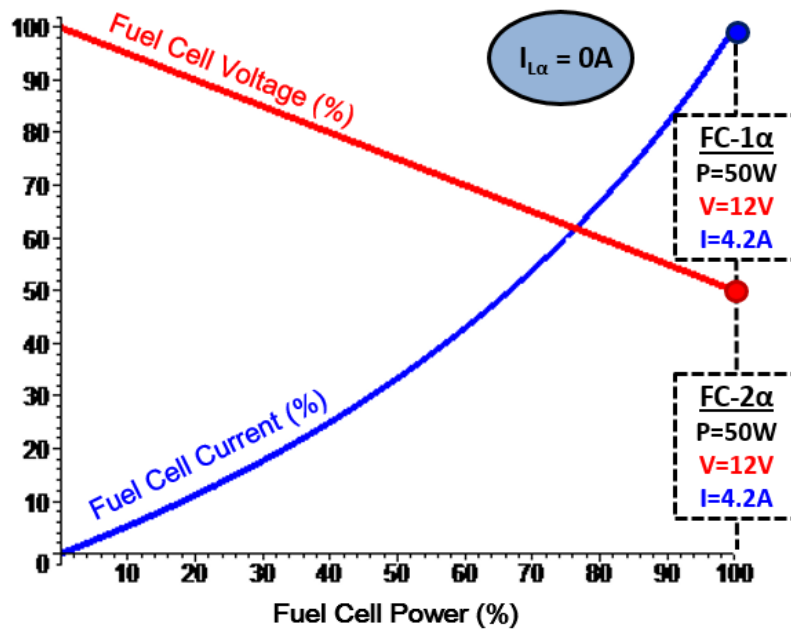
Next, two Magna-Power Electronics DC Power Sources (55V/180A/2kW) are used to emulate two fuel cell stacks; along with a Chroma DC Electronic Load (125V/500V/2kW) to model the fuel cell V-P and I-P characteristic behavior illustrated in

Figure 6 during various power sharing conditions. Next, the sources are set at the voltage levels corresponding to the desired power levels, and the electronic load resistance is set to draw the appropriate amount of current. Table 1 describes the power operation points for the three different cases. Figure 18 - Figure 20 illustrate the respective fuel cell input characteristics (on the left) and the resulting power sharing inductor voltage and current waveforms (on the right). It is significant to note that the ratios of oscilloscope divisions to actual values are 10V/10V for voltage and 500mV/5A for current.

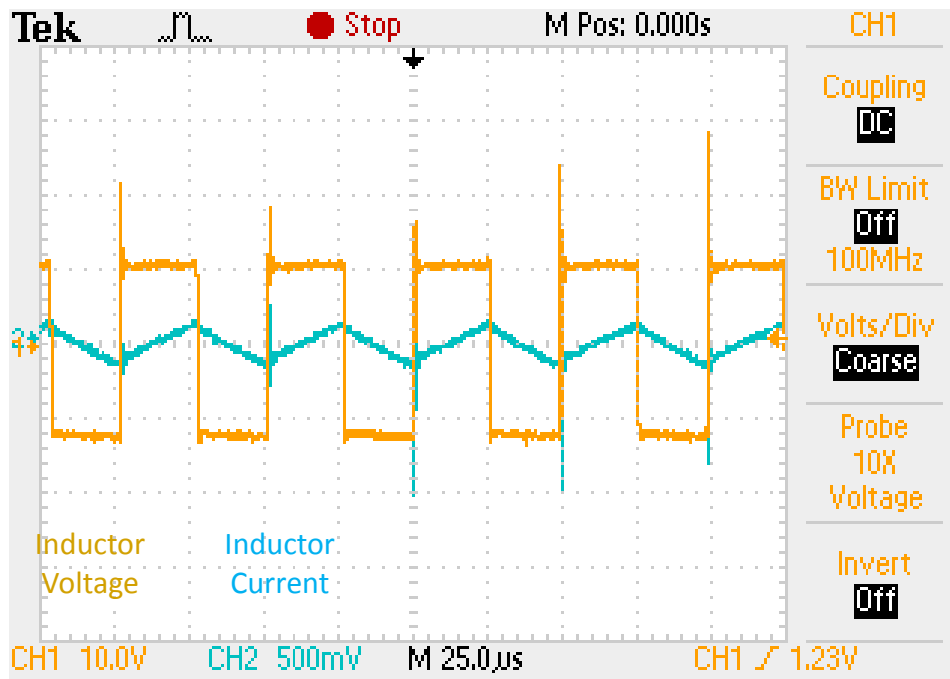
Table 1: 100W single-stage FC-PSC hardware verification for three power sharing cases:
(i.) 100%/100%, (ii.) 50%/100%, and (iii.) 20%/80%.

Case	FC-1 α			FC-2 α			Load
#	P ₁ [W]	V ₁ [V]	I ₁ [A]	P ₂ [W]	V ₂ [V]	I ₂ [A]	R [Ω]
I	50.4	12.0	4.2	50.4	12.0	4.2	5.7
II	50.4	12.0	4.2	25.2	18.0	1.4	11.9
III	10.1	21.6	0.5	40.3	14.4	2.8	25.7

Figure 18 displays the results of Case I's 100%/100% power sharing scenario. Here, it can be seen the source voltages are equivalent, such that $V_1 = V_2 \cong 12V$ and $D = D' = 50\%$. This results in the average DC current through the zonal power sharing inductor being zero. This verifies that both source powers are equal as no current is shared between them.



a.)



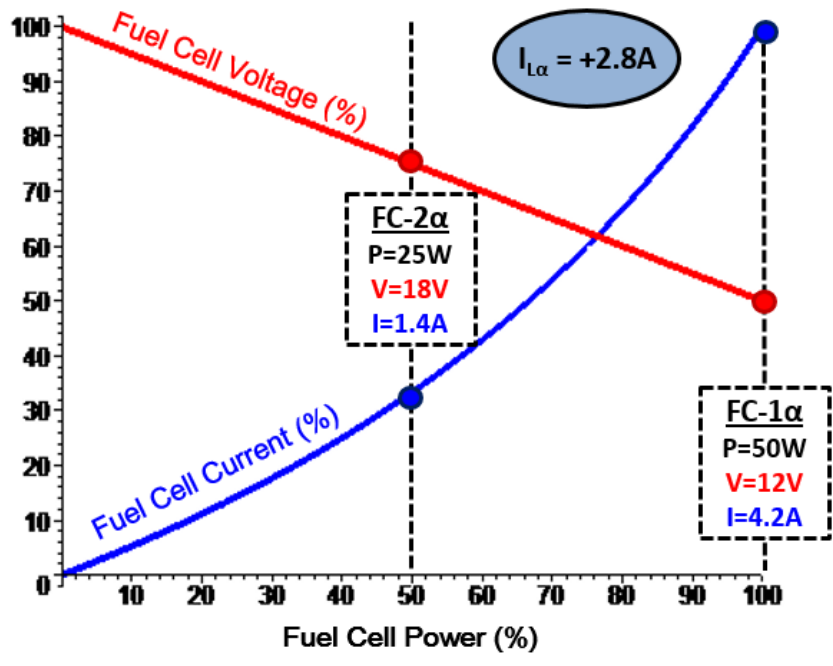
b.)

Figure 18. Given Case I's fuel cell input characteristics on the left, the zonal power sharing inductor waveforms are shown on the right. The two verify power sharing for Case I (100% /100%). $V_1 = V_2 \cong 12V$ for $D = D' = 50\%$ and $I_{L\alpha} \cong 0A$.

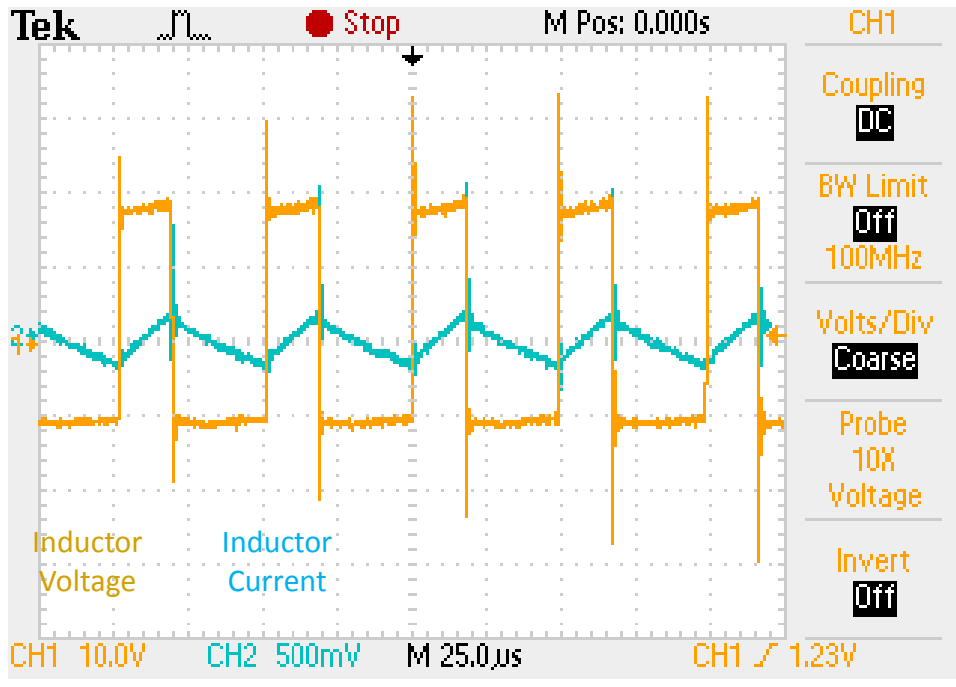
Figure 19 displays the results of Case II's 100%/50% power sharing scenario. Here, it can be seen that $V_2 \cong 18\text{V}$ for $D' = 40\%$, and $V_1 \cong 12\text{V}$ for $D = 60\%$. A resulting +2.8 DC current average through the zonal power sharing inductor can also be observed, verifying power sharing between sources.

Figure 20 displays the results of Case III's 20%/80% power sharing scenario. Here, it can be seen that $V_1 \cong 21.6\text{V}$ for $D = 40\%$, and $V_2 \cong 14.4\text{V}$ for $D' = 60\%$. A resulting -2.3 DC current average through the zonal power sharing inductor can also be observed, once again verifying power sharing between sources.

Altogether, these findings serve as hardware proof-of-concept for the power sharing technology proposed in this paper. The input voltage characteristics have been modified to replicate FC behavior as three resulting power sharing cases are examined: $I_{L\alpha} = 0\text{A}$, +2.8A, and -2.3A. Conclusively, a wide range of bidirectional operation for the PSC is verified.



a.)



b.)

Figure 19. Given Case II's fuel cell input characteristics on the left, the zonal power sharing inductor waveforms are acquired on the right. The two verify power sharing for Case II (100% /50%). $V_2 \cong 18V$ for $D' = 40\%$, $V_1 \cong 14.4V$ for $D = 60\%$, and $I_{L\alpha} \cong +2.8A$.

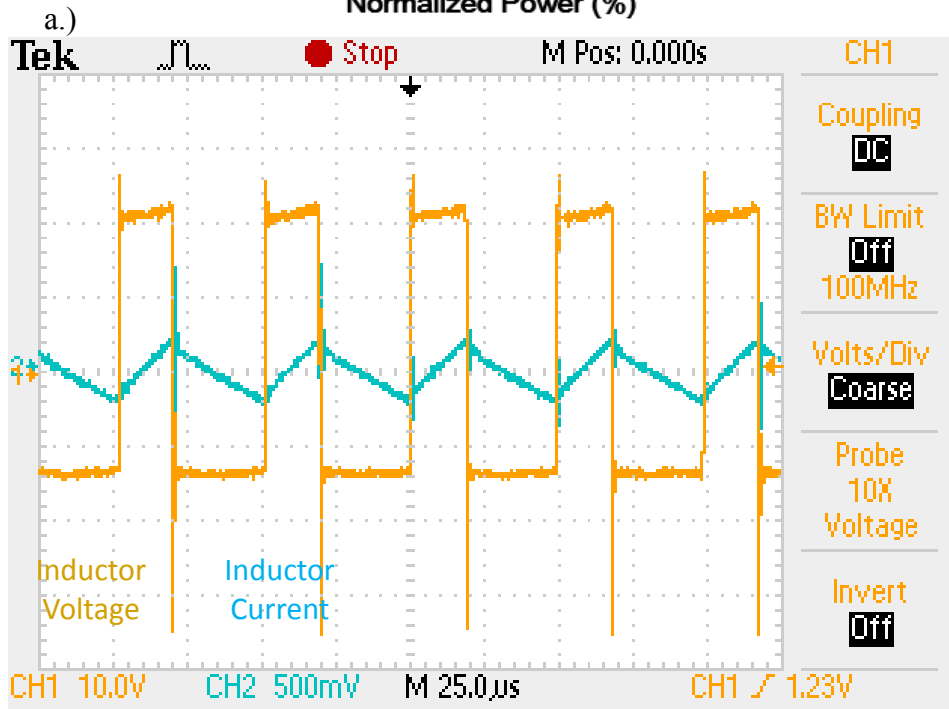
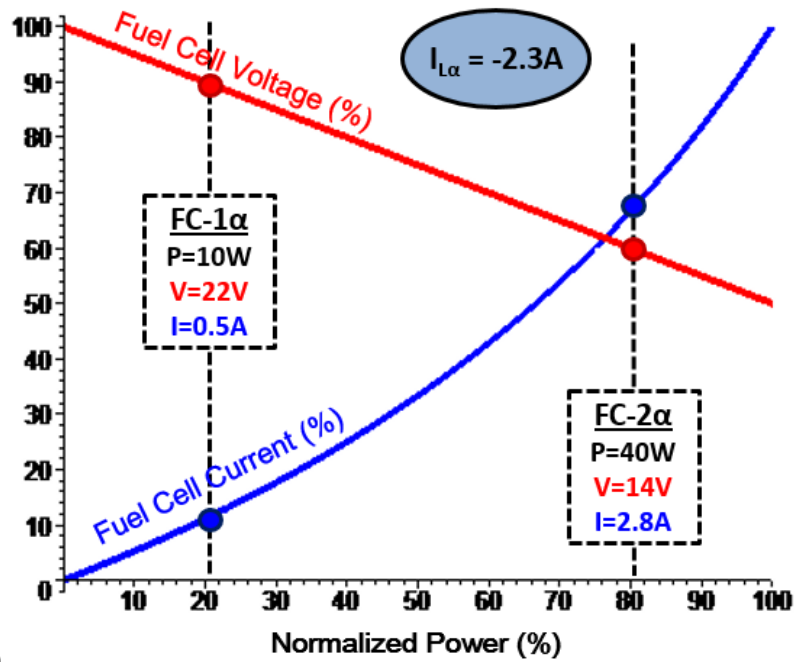


Figure 20. Given Case III's fuel cell input characteristics on the left, the zonal power sharing inductor waveforms are acquired on the right. The two verify power sharing for Case III (20%/80%). $V_1 \cong 21.6V$ for $D = 40\%$, $V_2 \cong 14.4V$ for $D' = 60\%$, and $I_{L\alpha} \cong -2.3A$.

Conclusion

This chapter presents a family of new multiport power sharing converter topologies for utility-scale fuel cell power generation. Multiple fuel cell sources have been shown to connect to a medium voltage grid via a single multilevel NPC inverter interface with high-frequency isolation. The proposed concept enables each fuel cell source to be electrically grounded, thereby eliminating the rise in electrostatic potential and contributing to increased safety. A unique family of power sharing technology has been shown to decouple series-connected source currents and enable control of each fuel cell's individual power level. Furthermore, multi-dimensional modeling and analysis of the proposed system's PI- and PV- characteristics have been presented. Various system topologies and design considerations are then discussed. Detailed analysis, simulation, and hardware experimentation has illustrated the functionality of PSC technology between 20%-100% power levels and has verified system-level benefits in a method which can be extended to any number of power sharing zones. Conclusively, the proposed family of multiport power sharing converter topologies realize independent power control per source as well as increased output power, operational flexibility, thermal balancing, source availability, and cost-effectiveness for utility fuel cell power generation.

CHAPTER IV

THE MULTI-LEVEL NINE-SWITCH CONVERTER

Introduction and Literature Review

In this chapter, a component-minimized dual-output multilevel converter is proposed, featuring low cost, high efficiency, high power quality, and low EMI characteristics. The dual-output characteristic of the proposed converter can be effectively employed in the following applications: (a.) online uninterruptible power supplies (UPSs), (b.) six-phase wind generators, and (c.) doubly-fed induction generator (DFIG) wind power systems. The operating principle and constraints on voltage and frequency of the dual outputs are detailed. Limits on the modulation index are analyzed at different operating conditions. Also, the loss breakdown is analyzed and compared with a conventional back-to-back multilevel converter. The simulation results are included in the summary to verify the validity of the proposed topology.

Normally, a dual-output DC/AC converter is widely used in the following industrial applications: dual 3-phase motor drives, online UPS systems with two controllable terminals, and six-phase motor drives [43-45]. In a conventional system, a separate converter is used for each output powered from the same dc-link voltage. This results in increased component count and adds to the inverter cost.

Previous research has explored component-minimized topologies which reduce the number of semiconductor switches and associated drivers. Two reduced switch scenarios are proposed in [44] and [45], where the “B4” and five-leg converters are presented,

respectively (see Figure 21 and Figure 22). In the first case of the B4 converter, one output phase is connected to the midpoint of the dc-bus instead of the converter leg as shown in Figure 21. In the second case of the five-leg converter, two ac ports share one leg, shown in Figure 22. Other methods component-minimized topologies have also been more recently proposed. In [46], the combined use of dc midpoint connection and phase leg sharing has been proposed, which is called four-leg converter as shown in Figure 23. A similar approach is also applied in single phase system and three-phase four-wire system [47]. The nine-switch converter is a recent and compelling solution [48, 49], shown in Figure 24. Note that the synthesis of nine-switch and dc-midpoint connection is called the six-switch converter [50], where one switching leg is replaced with dc-bus capacitors as shown in Figure 25. The similar approach is employed in single phase system, called three-switch converter. However, the variant form is achieved at the expense of dc bus utilization and output waveform quality [51, 52].

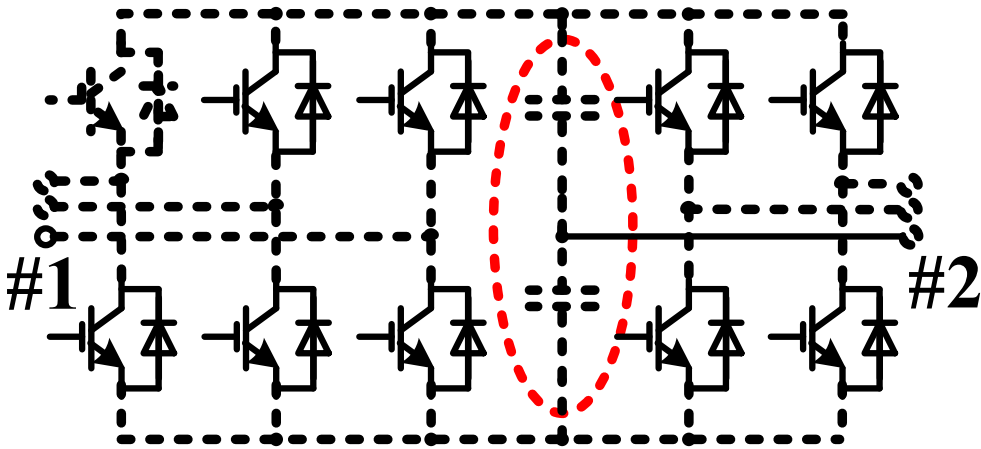


Figure 21. Review of topologies with reduced switches: the B4 converter [44]

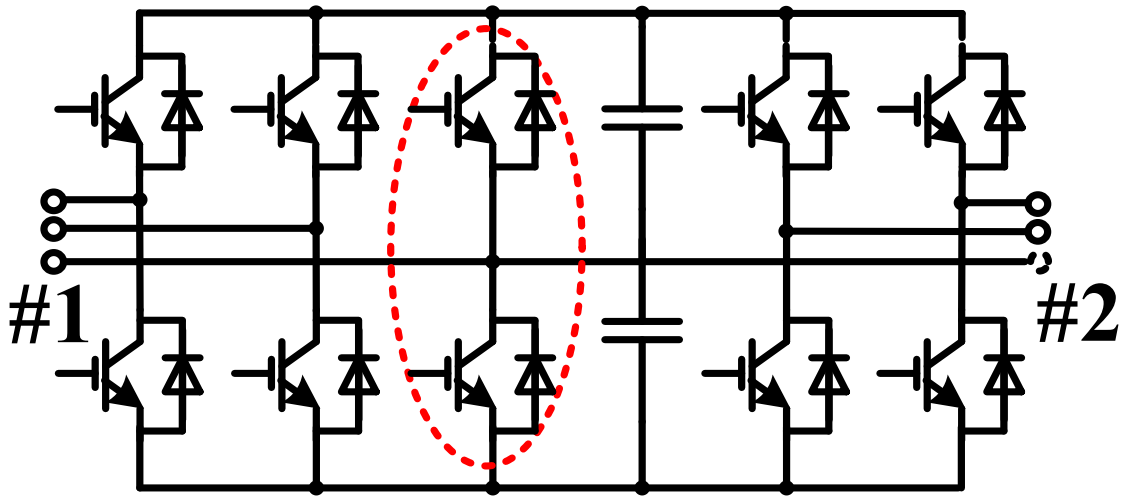


Figure 22. Review of topologies with reduced switches: the Five-leg converter [45]

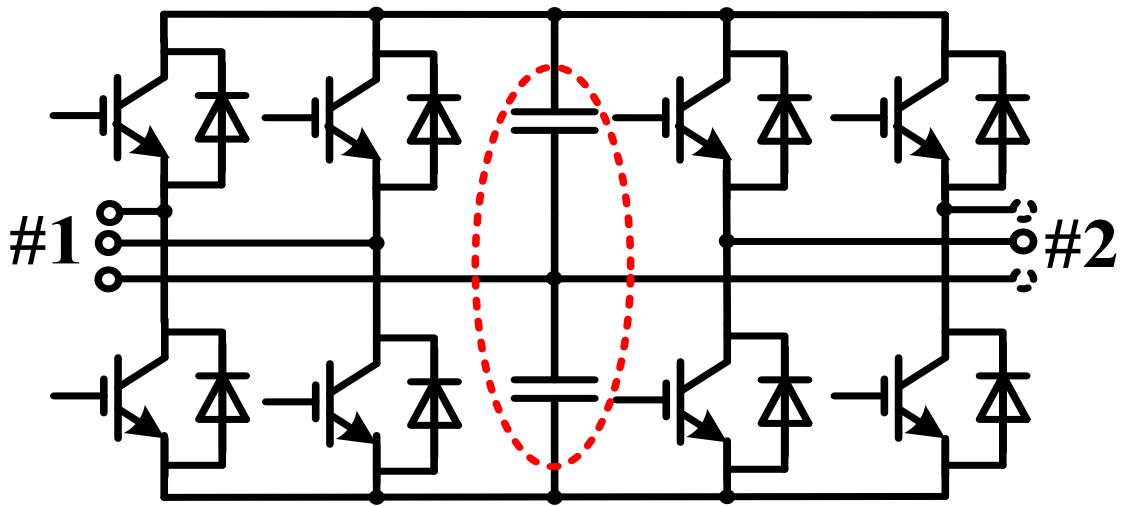


Figure 23. Review of topologies with reduced switches: the Four-leg converter [46]

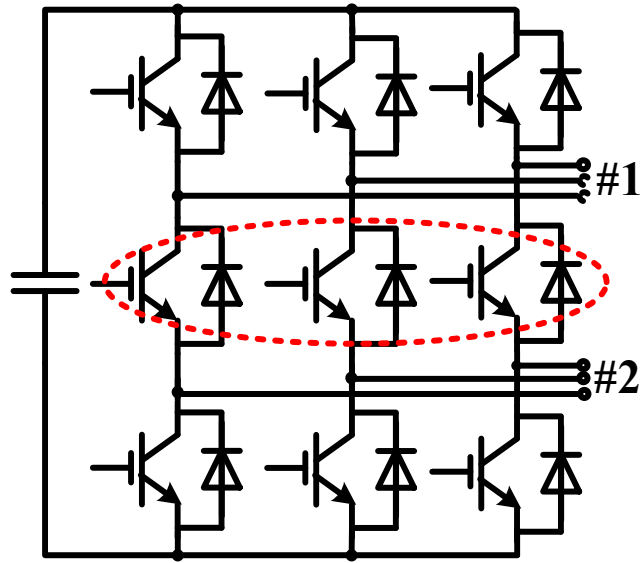


Figure 24. Review of topologies with reduced switches: the nine-switch converter [48]

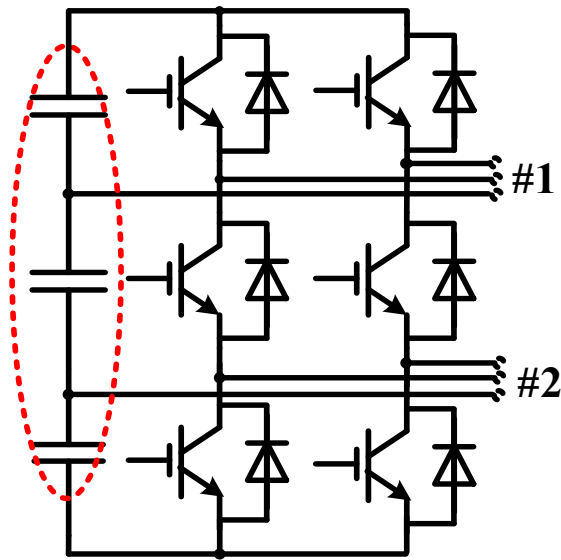


Figure 25. Review of topologies with reduced switches: the six-switch converter [50]

It should be noted that the nine-switch converter still has two-level converter drawbacks, such as low efficiency, poor THD, high EMI, etc. Nowadays, the multilevel converters, especially three-level converters, are a promising alternative to the conventional two-level converters, due to their ability to meet the increasing demand of power ratings and power quality with lower THD, lower EMI, and higher efficiency [53, 54]. Reference [55] applied new IGBT modules in advanced Neutral-Point Clamped (NPC) 3-level converters to achieve higher efficiency. The active NPC (ANPC) inverter is proposed to overcome the unequal power loss distribution among the devices [56]. This paper proposes a component-minimized dual-output multilevel converter which synthesizes the aforementioned three-level topology and nine-switch techniques. The proposed converter retains most of the desirable features of multilevel converter such as lower THD, low EMI. More advantages are as follows:

1. **Economical.** Size and weight are reduced. As for proposed T-type variant converter (see Figure 27), the switch count is reduced by 12.5% in comparison to two separate converters.
2. **High DC-bus Utilization.** In the case of dual outputs at same frequency and same phase, there is no reduction compared to conventional separate converters.
3. **Higher Efficiency.** As discussed later, conduction losses are greatly reduced due to the effect of dual-current cancellation in the online UPS applications.

Proposed Dual-Output Multilevel Converter Topology and Modulation Scheme

In this section, a three-phase dual-output multilevel converter topology is proposed. The modulation scheme and constraints are then discussed in light of different applications and operation modes.

Proposed Topology

A traditional dual-output multilevel converter is illustrated in Figure 26, where Figure 27 shows the proposed three-phase switch-minimized dual-output 3-level converter topology. It is noted that the middle switch (S_{aM} , S_{bM} , S_{cM}) in each individual leg is shared by the top and bottom converters, thereby reducing the switch count by 12.5% in comparison to the traditional dual separate converters.

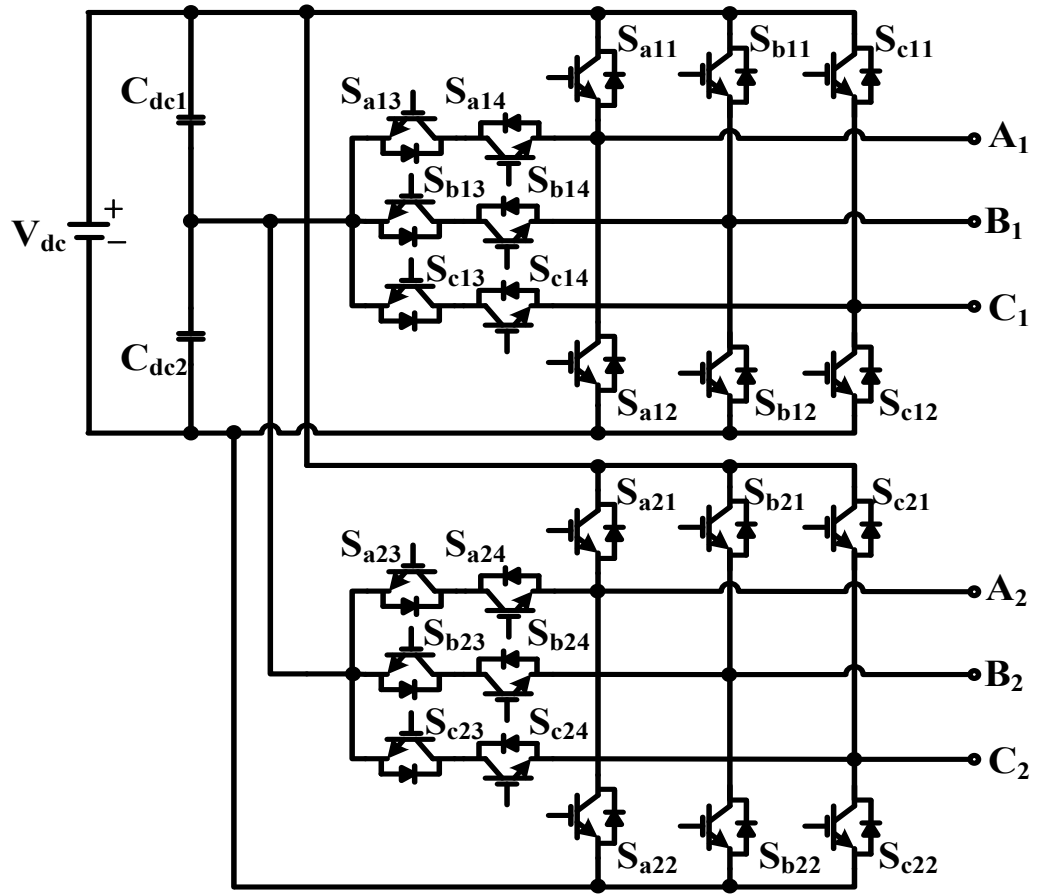


Figure 26. Traditional Dual-output 3-level Converter

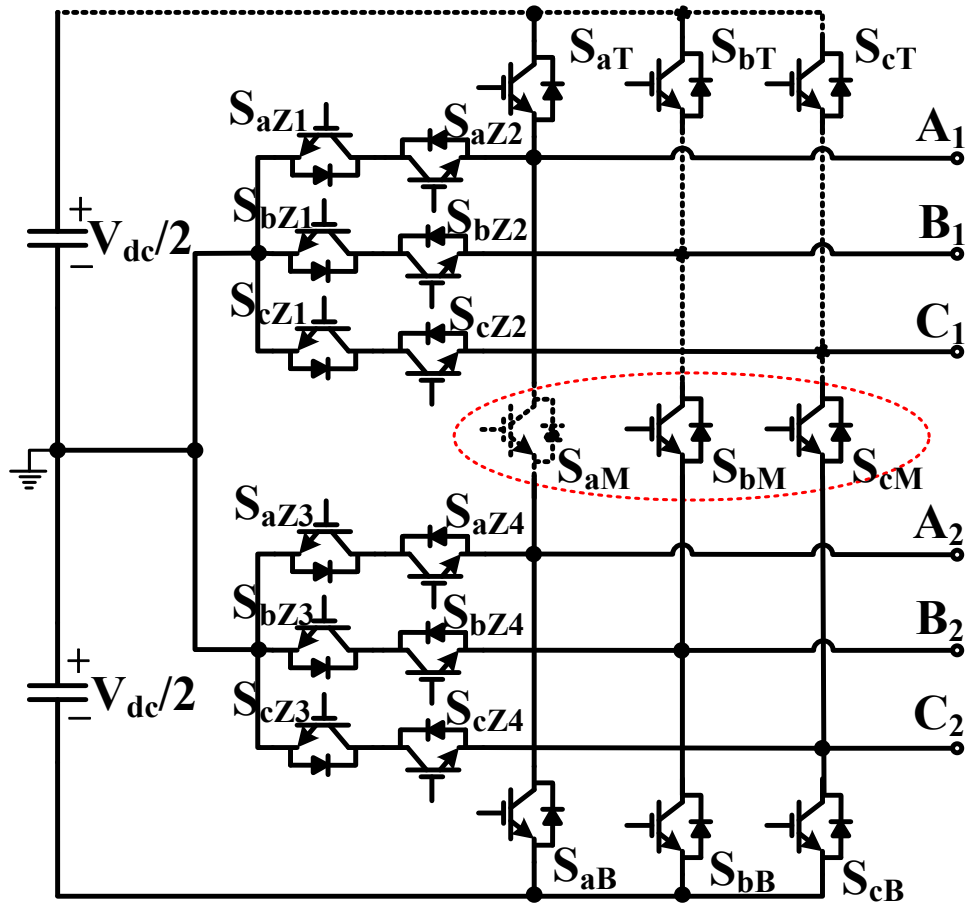


Figure 27. Proposed switch-minimized dual-output 3-level converter topology.

Modulation Scheme and Constraints

In order to reduce switch count, the proposed converter topology imposes certain constraints on the switching state design. Due to the middle switches shared by both of top and bottom sets, the proposed converter has only 6 valid switching states per phase as listed in Table 2. Here, it is noted that 3 switching states are forbidden; each occurs when the bottom output (V_{x2}) is greater than the top (V_{x1}). For instance, when the top set output is $-V_{dc}/2$ and the bottom one is $+V_{dc}/2$, switches S_{xT} , S_{xM} and S_{xB} are conducted simultaneously, yielding a short-through loop and a resulting switching state which cannot be achieved.

Table 2: Switching states in T-type variant 3-level converter (x=a, b or c)

STATES	S_{xT}	S_{xM}	S_{xB}	S_{xZ1}	S_{xZ2}	S_{xZ3}	S_{xZ4}	V_{x1}	V_{x2}
VALID	1	1	0	0	1	0	1	$V_{dc}/2$	$V_{dc}/2$
	1	0	0	0	1	1	1	$V_{dc}/2$	0
	1	0	1	0	1	1	0	$V_{dc}/2$	$-V_{dc}/2$
	0	0	0	1	1	1	1	0	0
	0	0	1	1	1	1	0	0	$-V_{dc}/2$
	0	1	1	1	0	1	0	$-V_{dc}/2$	$-V_{dc}/2$
FORBIDDEN	1	X	X	1	1	X	X	0	$V_{dc}/2$
	1	1	1	X	X	X	X	$-V_{dc}/2$	$V_{dc}/2$
	X	X	1	X	X	1	1	$-V_{dc}/2$	0

Figure 28 shows the generalized carrier-based modulation scheme for the proposed dual-output converter. As illustrated, two modulating waveforms are compared with a common triangular carrier. It can be observed that the forbidden states occur when the bottom reference is greater than the top one. Therefore, in order to avoid forbidden states

occurring, it is significant to guarantee that the reference of the top set should be greater than that of the bottom at any instant. This fact becomes the main constraint for the switching scheme design of proposed converter.

From the valid switching states in Table 2, it can be seen that the state of S_{xM} is high only when the states of S_{xZ2} and S_{xZ3} are different. Therefore, for all valid states ($v_{Top_ref} > v_{Bot_ref}$), the switching behavior of S_{xM} can be obtained from Equation 4.1.

$$S_{xM} = \overline{S_{xZ2}} + \overline{S_{xZ3}} \quad (4.1)$$

With regard to the rest of the switches, the switching pattern is similar to that of traditional dual separate converters. Taking the top set as an example, as shown in Figure 28, when the top set reference is at the positive cycle, S_{xZ2} is constantly high. Meanwhile, if the top reference is higher than the carrier, S_{xT} is “1” and S_{xZ1} is “0”, which yields a high-level output. In contrast, if the top reference is lower than the carrier, S_{xZ1} is high and S_{xT} is low, resulting in the zero-level output.

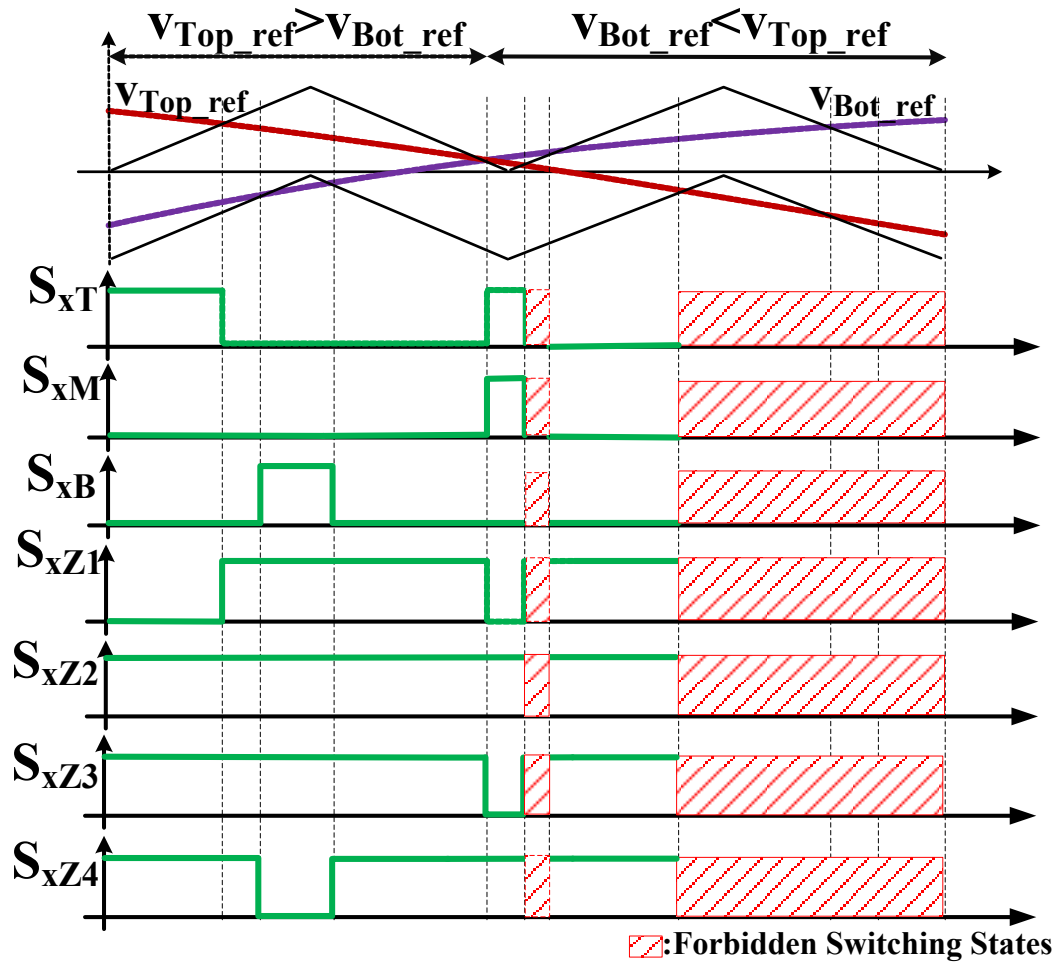


Figure 28. Modulation Scheme and Constraint of Proposed Converter

Modulation Index Analysis

Depending on the operating frequency and phase difference between the two outputs, the proposed converter can be operated in the following three modes: Same Frequency and Same Phase (SFSP), Same Frequency and Different Phase (SFDP), and Different Frequency (DF). Analysis of the modulation index is given for each mode.

Mode 1: Same Frequency and Same Phase

SFSP mode occurs when both of the dual-outputs operate at a similar frequency and phase. In order to maximize the modulation index and avoid intersecting each other, the reference signals of the top set are upward to the top of the dc plane, whereas the bottom set references are pushed to the bottom by adding appropriate dc bias. The references of two sets (v_{Top} , v_{Bot}) are as follows:

$$\begin{cases} v_{Top}(t) = M_{Top} \sin(\omega t) + (1 - M_{Top}) \\ v_{Bot}(t) = M_{Bot} \sin(\omega t) - (1 - M_{Bot}) \end{cases} \quad (4.2)$$

where M_{Top} and M_{Bot} are the modulation indices of top set and bottom set (defined as the peak-to-peak magnitude of the sinusoid reference divided by the peak-to-peak magnitude of the carrier), respectively.

The constraint that the top reference should be greater than the bottom one should be satisfied as shown in Equation 4.3 [49, 52].

$$M_{Top} \sin(\omega t) + (1 - M_{Top}) \geq M_{Bot} \sin(\omega t) - (1 - M_{Bot}) \quad (4.3)$$

From Equation 4.3, we can get Equation 4.4.

$$M_{Bot} \leq 1 \leq M_{Top} + \frac{2 - 2 \times M_{Top}}{1 + \sin(\omega t)} \quad (4.4)$$

From Equation 4.4, it can be seen that M_{Top} and M_{Bot} can approach 1 simultaneously. Figure 29 illustrates the modulation waveforms at different modulation indices (0~1). It can be observed that both of modulation indices can simultaneously reach the maximum of unity, which means the proposed converter can output the same voltage as traditional back-to-back topology.

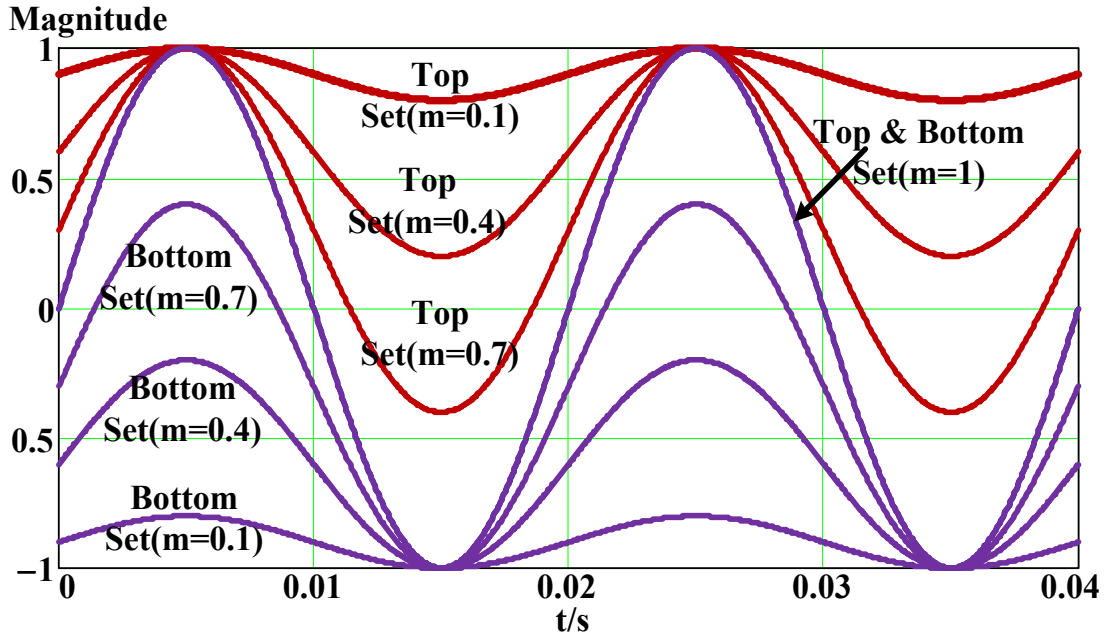


Figure 29. Modulation waveforms for SFSP operation.

SFSP Mode is particularly suitable for the online UPS application shown in Figure 30, where the voltage of the load is forced to follow that of the grid [49].

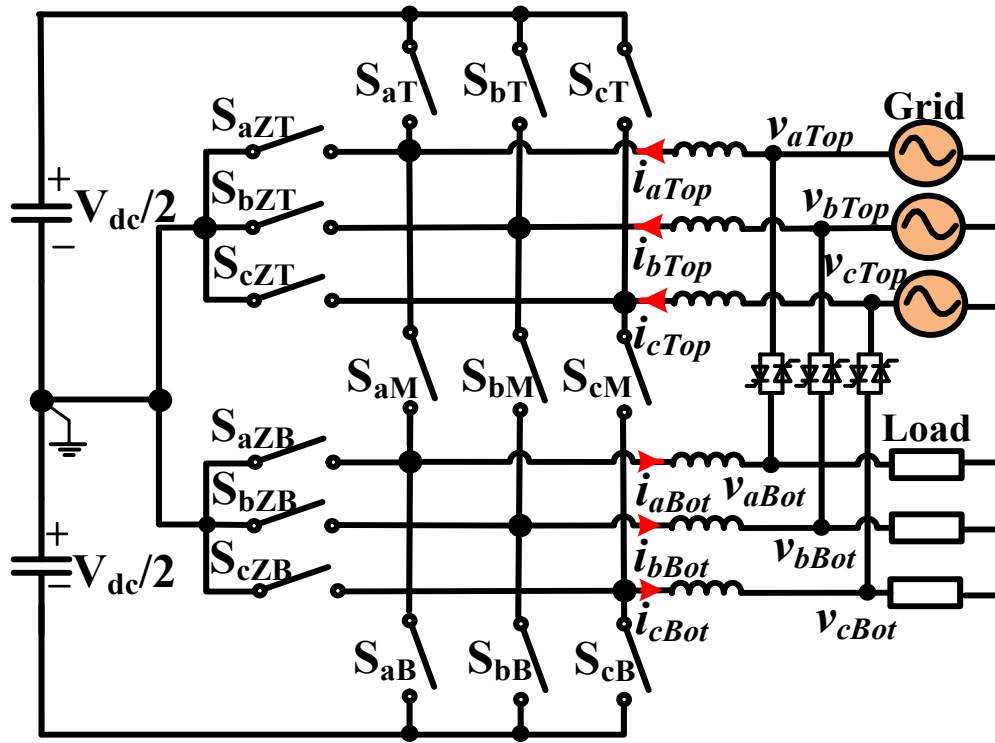


Figure 30. Typical SFSP Application for Proposed Topology: Online UPS.

Mode 2: Same Frequency and Different Phase

SFDP mode occurs when both of the dual-outputs operate at a similar frequency but experience a difference in phase. For SFDP operation with phase difference θ , the reference voltages and modulation constraints are as follows:

$$\begin{cases} v_{Top}(t) = M_{Top} \sin(\omega t + \theta) + (1 - M_{Top}) \\ v_{Bot}(t) = M_{Bot} \sin(\omega t) - (1 - M_{Bot}) \end{cases} \quad (4.5)$$

$$M_{Top} \sin(\omega t + \theta) + (1 - M_{Top}) \geq M_{Bot} \sin(\omega t) - (1 - M_{Bot}) \quad (4.6)$$

Assuming that $M_{Top}=M_{Bot}=M$, Equation 4.6 can be simplified as follows.

$$M \leq \frac{2}{2 - 2 \cos(\omega t + \frac{\theta}{2}) \sin\left(\frac{\theta}{2}\right)} \quad (4.7)$$

Next, the maximum modulation index M_{max} is obtained in Equation 4.8, and is depicted in Figure 31.

$$M_{max} = \frac{1}{1 + \left| \sin\left(\frac{\theta}{2}\right) \right|} \quad (4.8)$$

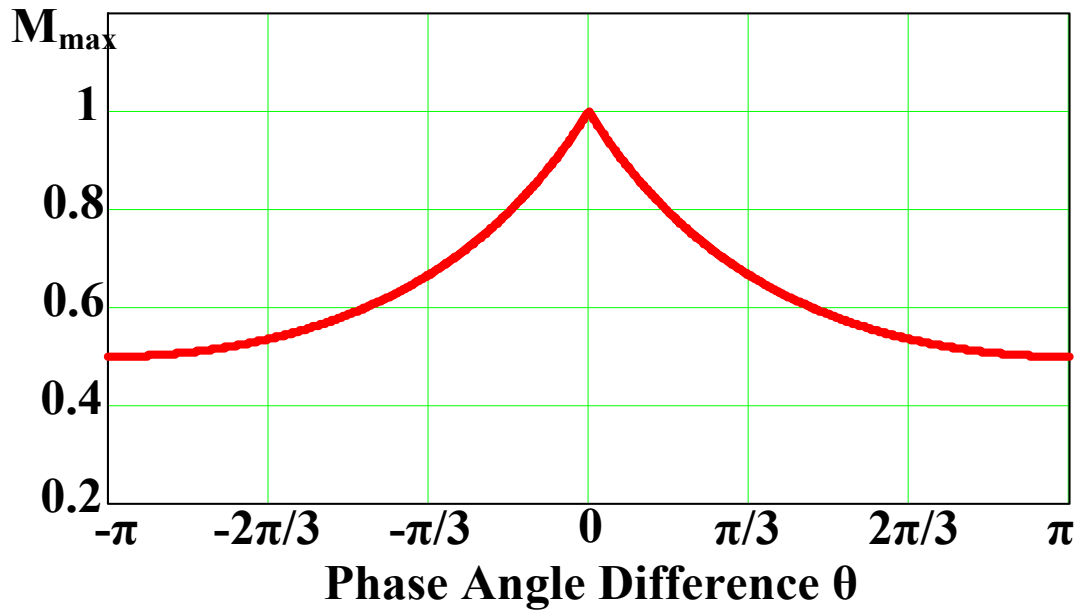


Figure 31. Maximum modulation index as the phase difference is adjusted in SFDP Mode.

Here, it can be seen that M_{max} decreases as the absolute value of the phase difference increases. In the worst case, the modulation index is reduced to one half, which means that the dc bus voltage should be doubled in order to maintain the same output voltage as that in traditional topology.

A suitable application for SFDP Mode operation is the six-phase large-scale wind generation illustrated in Figure 32. Here, the phase of one output can be shifted by either 30° or 60° with respect to the other [57].

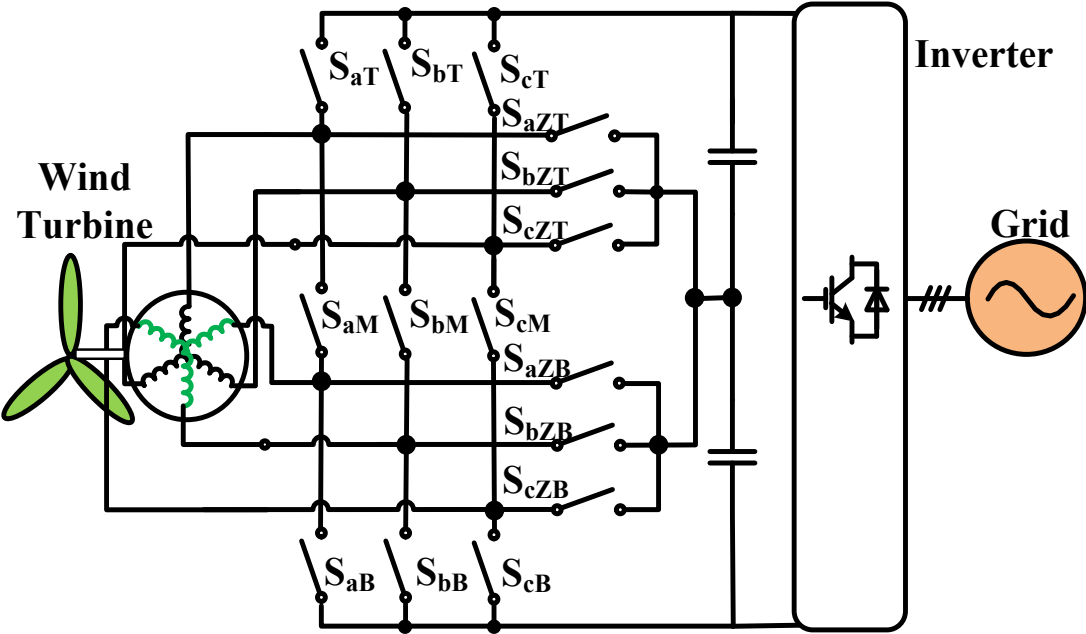


Figure 32. Typical SFDP Application for Proposed Topology: Six-Phase Wind Generation

Mode 3: Different Frequency

The DF Mode occurs when the frequency of each of the dual-outputs is different. Assuming that the modulation references have a difference in frequency and phase angle, the reference voltages and modulation constraint are as follows:

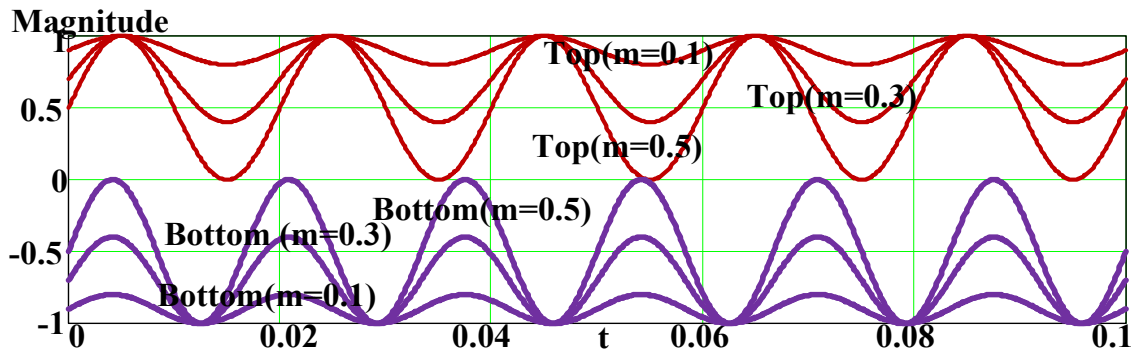
$$\begin{cases} v_{Top}(t) = M_{Top} \sin(\omega_1 t + \theta) + (1 - M_{Top}) \\ v_{Bot}(t) = M_{Bot} \sin(\omega_2 t) - (1 - M_{Bot}) \end{cases} \quad (4.9)$$

$$M_{Top} \sin(\omega_1 t + \theta) + (1 - M_{Top}) \geq M_{Bot} \sin(\omega_2 t) - (1 - M_{Bot}) \quad (4.10)$$

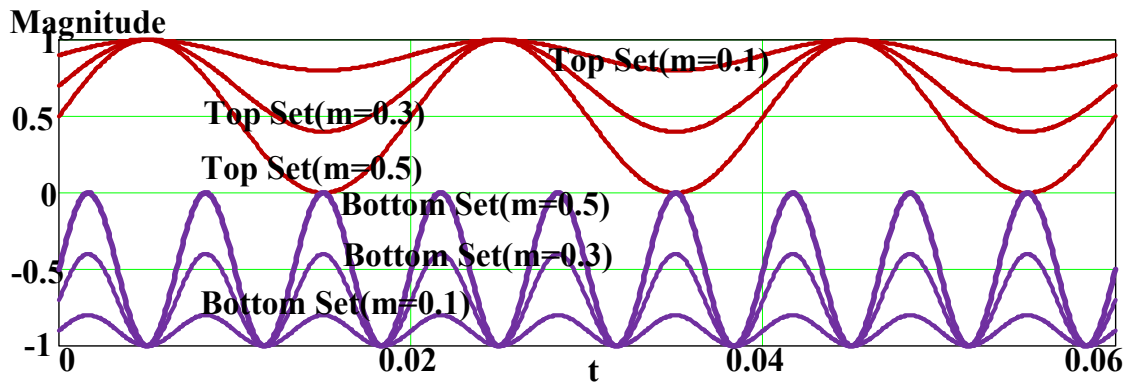
From Equation 4.10, we can obtain Equation 4.11, which shows that the sum of two modulation indices must not exceed 1.

$$M_{Bot} + M_{Top} \leq 1 \quad (4.11)$$

Figure 33 illustrates two examples where two outputs are operated at different frequencies. It is noted that the modulation indices $M_{Bot} = M_{Top} = 0.5$ are critical values. Therefore, the dc voltage of the converter has to be twice as high as the rated dc voltage of traditional topologies with the same ac outputs.



(a) Top: 50Hz, Bottom: 60Hz



(b) Top: 50Hz, Bottom: 150Hz

Figure 33. Two sets of modulation waveforms during DF Mode operation.

From the above analysis, the needed dc-bus voltage varies in different cases due to the different modulation indices. This affects the semiconductor devices selection and system cost. Therefore, it is necessary to evaluate the system cost according to specific application cases.

Some suitable applications for DF Mode operation are for DFIG wind generation (see Figure 34) or some dual-motor drive applications [58].

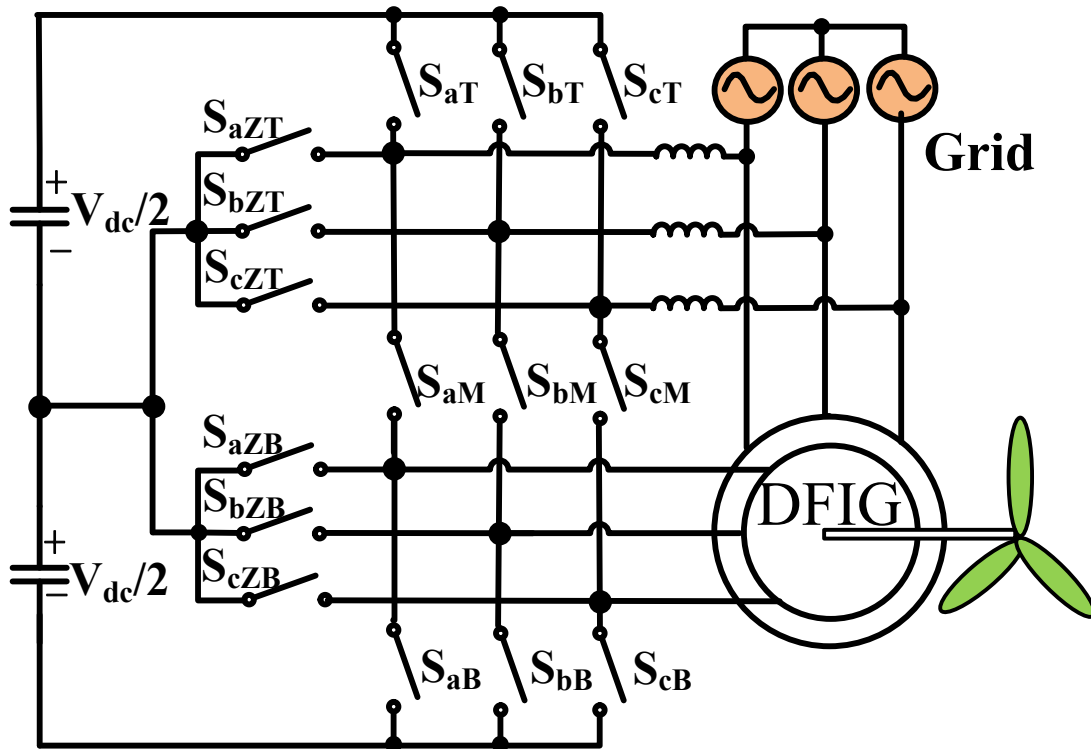


Figure 34. Typical DF Application for Proposed Topology: DFIG Wind Generation

Operation Mode Conclusions

Based on the analysis, the proposed topology is most aptly suited for SFSP applications, like online-UPS system, due to the unchanged dc-bus utilization. Therefore, the following section further investigates the converter's power loss profile using online UPS system as an example.

Case Study: Efficiency Analysis of an Online UPS

In order to effectively inspect efficiency of the proposed dual-output topology, a case study of a 30kW online UPS is taken as an example (see Figure 30). It is worth mentioning that, due to the distinctive structure of proposed topology, input-output currents flowing paths are coupled. Subsequently, system efficiency is dependent on a series of variables such as output power, load power factor, modulation index, and switching frequency. This makes the efficiency analysis complicated.

Assuming that the voltage and current of two sets are shown Figure 35, it can be divided into 9 sections in one power cycle based on the directions of voltages and currents. Basically, the 9 sections can be divided two categories. The first one has independent current paths (e.g., ①, ②, etc.), while the second has coupled current paths (e.g., ③, ④, etc.). Hence, the following analysis only chooses ② and ④ as examples.

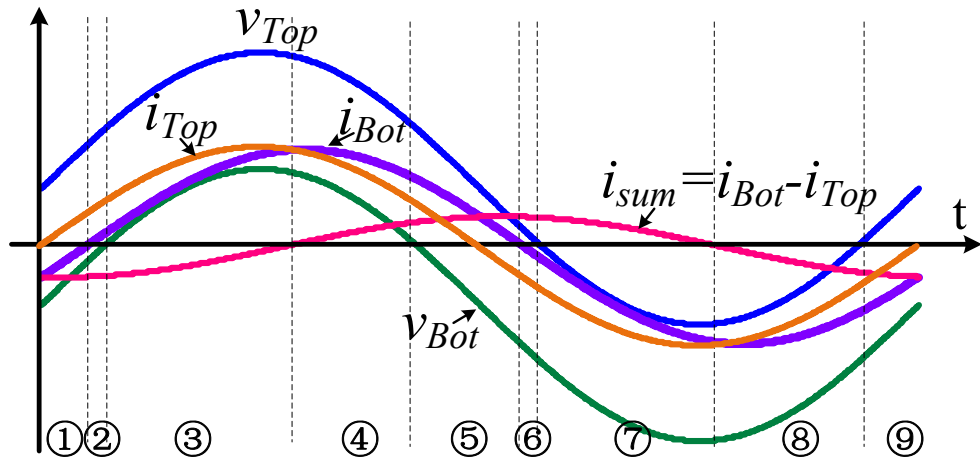


Figure 35. Voltages and Currents for Both Dual-Outputs

Independent Current Path Example: Interval ②

Figure 36 illustrates the Interval ②'s operating process in one switching cycle. Since the top and bottom current paths are decoupled, the loss calculation in this process is the same as that for traditional back-to-back converter.

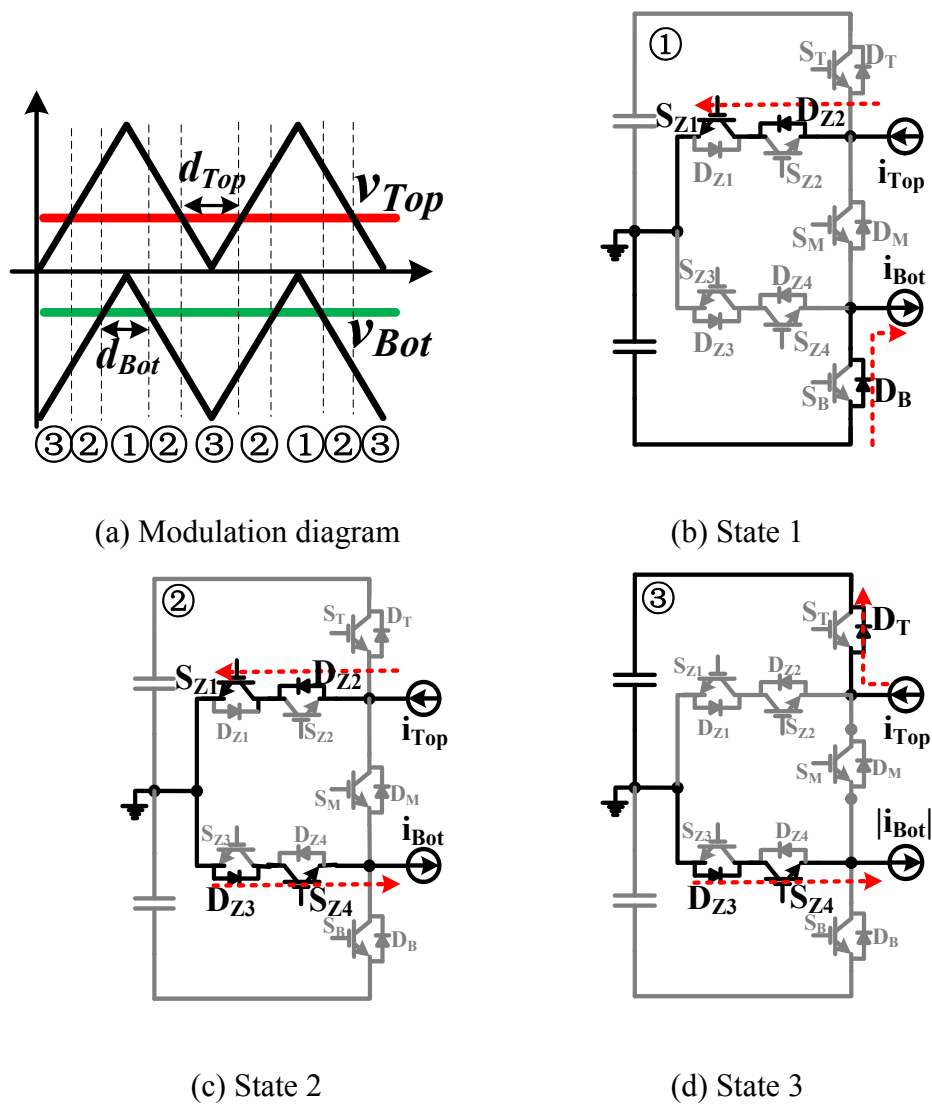


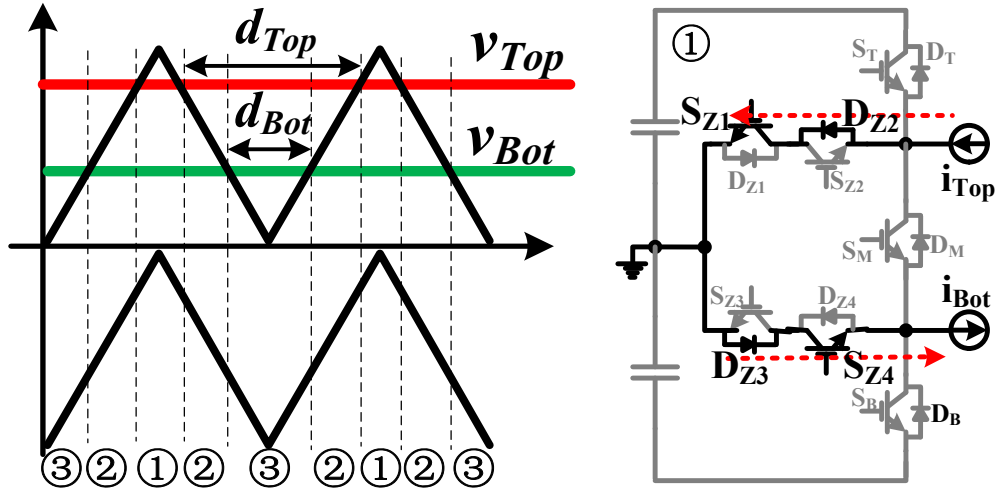
Figure 36. Interval ②'s Operating Diagram for one switching cycle.

As shown in Figure 36, the top current i_{Top} commutes between S_{Z1} and D_T , whereas the bottom current i_{Bot} commutes between S_{Z4} and D_B . Equation 4.12 governs the switching loss in this interval, including the turn-on losses of S_{z1} and S_{Z4} (E_{onSZ1} and E_{onSZ4}), turn-off losses of S_{z1} and S_{Z4} (E_{offSZ1} and E_{offSZ4}), the reverse recovery losses of D_B , and D_T (E_{rrDT} and E_{rrDB}).

$$E_{sw_2} = \sum_{n=0}^{N_I} E_{onSZ1} [i_{Top}(n)] + \sum_{n=0}^{N_I} E_{offSZ1} [i_{Top}(n)] + \sum_{n=0}^{N_I} E_{rrDT} [i_{Top}(n)] + \sum_{n=0}^{N_I} E_{onSZ4} [i_{Bot}(n)] + \sum_{n=0}^{N_I} E_{offSZ4} [i_{Bot}(n)] + \sum_{n=0}^{N_I} E_{rrDB} [i_{Bot}(n)] \quad (4.12)$$

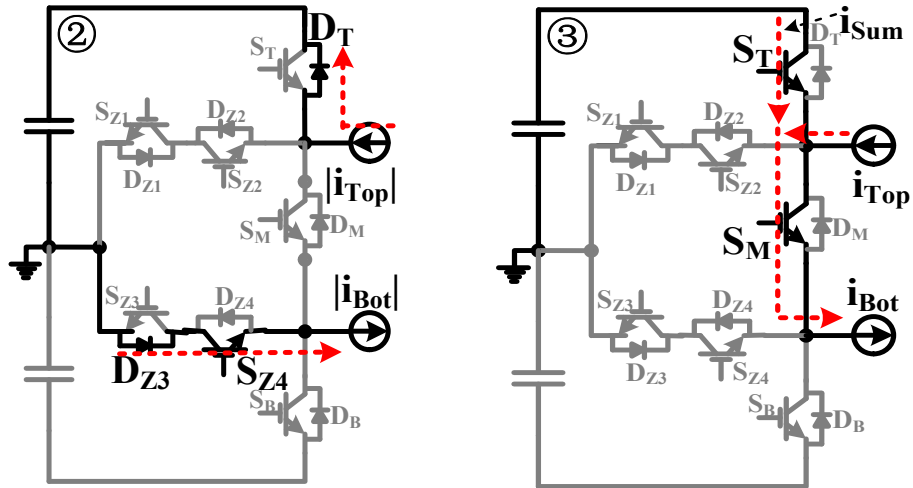
Coupled Current Path Example: Interval ④

Figure 37 illustrates Interval ④'s operating process in one switching cycle. Here, the current paths of each output are coupled. Conduction loss is calculated, noting that the current flowing through S_T is the sum of i_{Top} and i_{Bot} when the converter is operated in State 3. From Figure 36, we can see the sum of currents i_{Sum} is less than either i_{Top} or i_{Bot} due to the partial cancellation of two currents, which means the conduction loss can be reduced greatly compared to the traditional back-to-back converter. Therefore, the proposed converter takes full advantage of the coupled current to decrease the conduction loss. Note, that the polarity of the current sum i_{Sum} determines whether the IGBT S_T or the anti-parallel diode D_T is conducted in State 3. If i_{Sum} is positive, S_T will be conducted, while the anti-parallel diode D_T will be conducted when i_{Sum} is negative.



(a) Modulation diagram

(b) State 1



(c) State 2

(d) State 3

Figure 37. Interval ④'s Operating Diagram for one switching cycle.

The conduction losses in the switching cycle are presented by the equations below.

$$E_{con+}_4 = \sum_{n=0}^{N_f} v_{D_T} [i_{Top}(n)] \cdot i_{Top}(n) \cdot (d_{Top} - d_{Bot}) T_s + \sum_{n=0}^{N_f} v_{S_T} [i_{Sum}(n)] \cdot i_{Sum}(n) \cdot d_{Bot} + v_{S_M} [i_{Bot}(n)] \cdot i_{Bot}(n) \cdot d_{Bot} \quad (4.13)$$

$$E_{con0}_4 = \sum_{n=0}^{N_f} (v_{S_{Z1}} [i_{Top}(n)] + v_{D_{Z2}} [i_{Top}(n)]) \cdot i_{Top}(n) \cdot (1 - d_{Top}) T_s + \sum_{n=0}^{N_f} (v_{D_{Z3}} [i_{Bot}(n)] + v_{S_{Z4}} [i_{Bot}(n)]) \cdot i_{Bot}(n) \cdot (1 - d_{Bot}) T_s \quad (4.14)$$

Here, E_{con+}_4 represents the conduction losses when output level is high, and E_{con0}_4 represents the conduction losses when output level is zero. For the top set, the switching loss occurs in the commutation process between States 1 and 2, including the turn-on losses of S_{Z1} (E_{onSZ1}), turn-off losses of S_{Z1} (E_{offSZ1}), and the reverse recovery losses of D_T (E_{rrDT}). For the bottom set, the switching loss occurs in the commutation process between States 2 and 3, including the turn-on losses of S_M (E_{onSM}), turn-off losses of S_M (E_{offSM}), and the reverse recovery losses of D_{Z3} (E_{rrDZ3}).

The switching loss in this interval E_{sw}_4 can be expressed as follows.

$$E_{sw}_4 = \sum_{n=0}^{N_f} E_{onSZ1} [i_{Top}(n)] + \sum_{n=0}^{N_f} E_{offSZ1} [i_{Top}(n)] + \sum_{n=0}^{N_f} E_{rrDT} [i_{Top}(n)] + \sum_{n=0}^{N_f} E_{onSM} [i_{Bot}(n)] + \sum_{n=0}^{N_f} E_{offSM} [i_{Bot}(n)] + \sum_{n=0}^{N_f} E_{rrDZ3} [i_{Bot}(n)] \quad (4.15)$$

Calculated Results

The calculation parameters are listed in **Table 3**, and the analytic results are shown in Figure 38 through Figure 41. Note all results are compare the proposed topology with a conventional back-to-back 3-level (B2B-3L) converter.

Definition of Parameters

The parameters for the 30kW Online UPS are delineated below.

Table 3: System parameters for a 30kW online UPS

Item	Description
Input Voltage	220V _{rms} / 50Hz
Output Voltage	220V _{rms} / 50Hz
Dc-bus Voltage	700V
IGBT S_T, S_M, S_B	150A/1200V (FF150R12RT4)
IGBT $S_{Z1}, S_{Z2}, S_{Z3}, S_{Z4}$	150A/600V (BSM150GB60DIC)
Filter Inductor	0.5mH
Filter Capacitor	25 μ F(330VAC)

Converter Losses

Figure 38 shows the loss breakdown of the proposed converter when it is operated at output power 30kW (resistive load), unity input power factor, a switching frequency of 10 kHz, and the inverter modulation index of 0.89. It can be seen that the conduction losses are reduced and, correspondingly, efficiency is higher in the proposed converter compared to traditional B2B-3L topology. Switching loss and inductor loss are almost same as the conventional one.

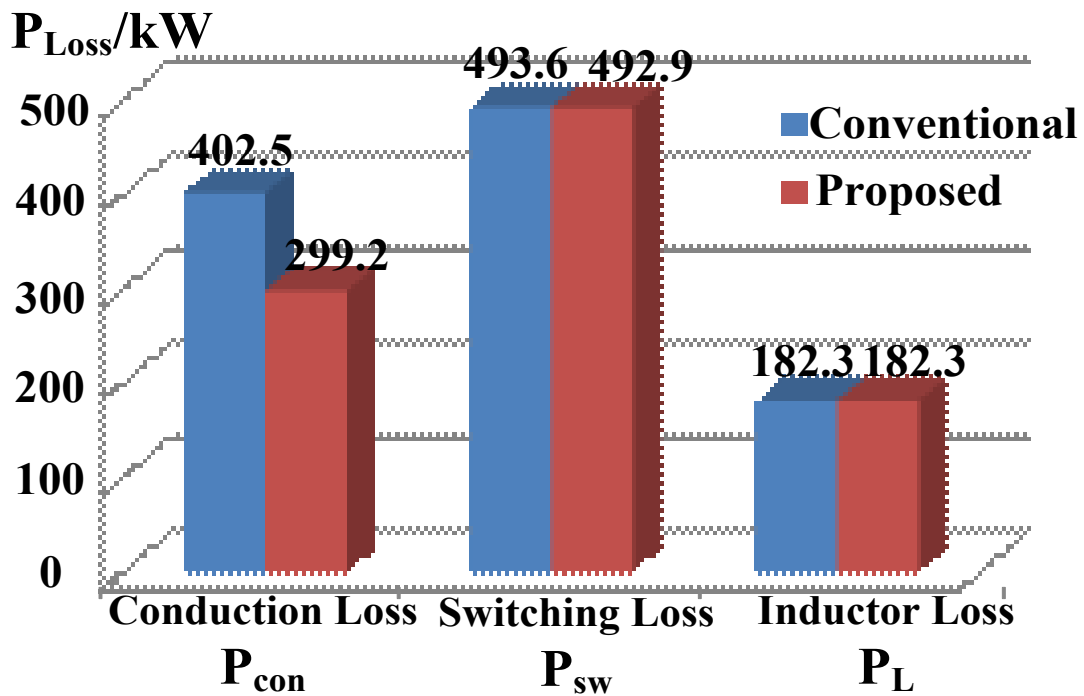


Figure 38. Loss Breakdown ($P=30\text{kW}$, $f_s=10\text{kHz}$).

Unlike the traditional back-to-back converter which features a symmetrical structure, the loss distribution on the top, middle, and bottom switches in the proposed converter are not even. As shown in Figure 39, due to the middle switch shared by two sets, in general the middle three switches dissipate more than twice the loss of those from the top three and bottom three switches.

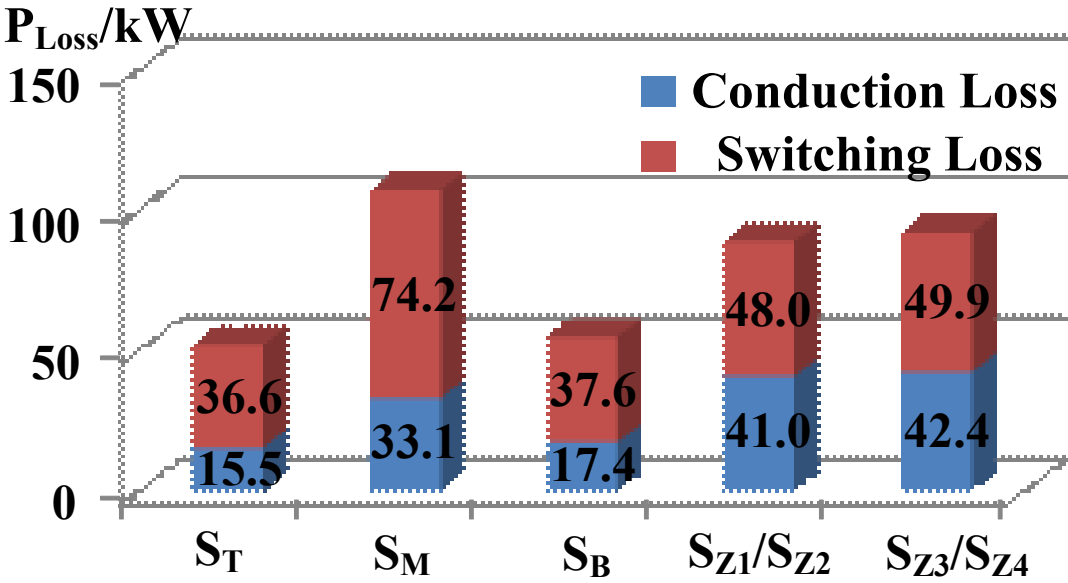


Figure 39. Loss distribution of individual switch ($P=30\text{kW}$, $f_s=10\text{kHz}$).

Converter Efficiency

From Figure 40, it can be seen that the efficiency of both proposed and conventional converters follows a similar trend with the increase of output power. However, the efficiency of the proposed converter is 0.5% higher than the traditional one.

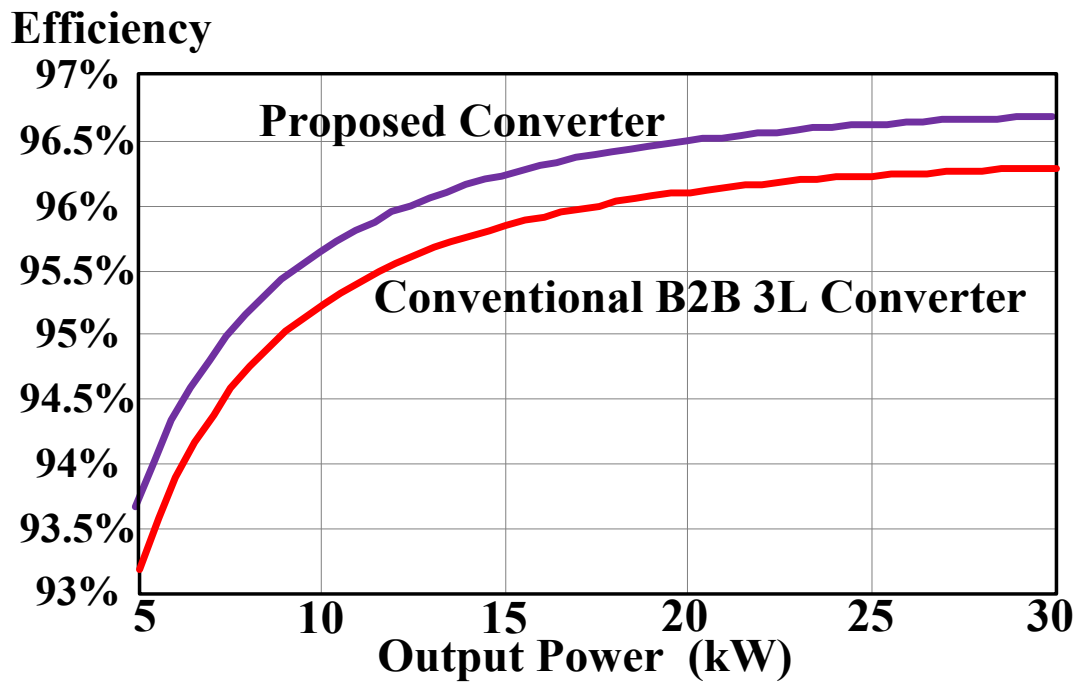


Figure 40. Efficiency vs. output power.

As illustrated in Figure 41, the efficiency continues to decrease with the increase of frequency due to the increase of the switching loss. However, this decrease is at a similar rate to the conventional topology.

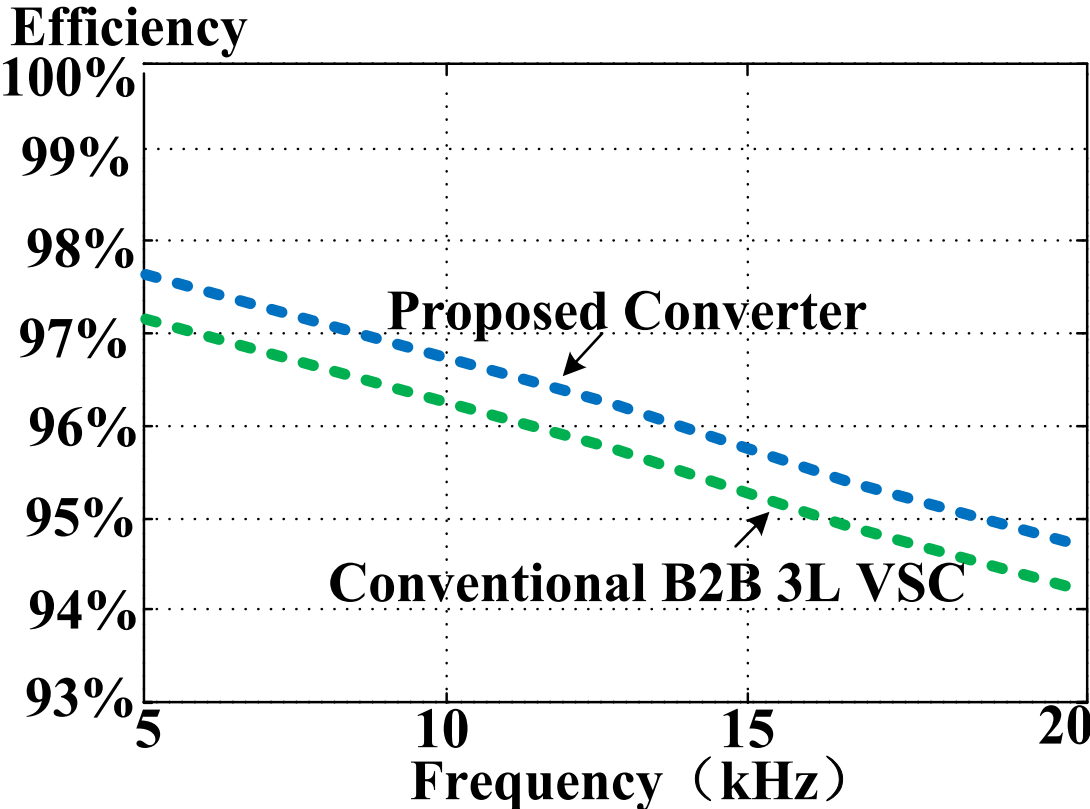


Figure 41. Efficiency vs. Switching Frequency.

Power Factor

The output power factor affects the sum of input and output currents, and ultimately influences the conduction loss. As shown in Figure 42, the conduction losses are slightly increased as the output power factor is decreased.

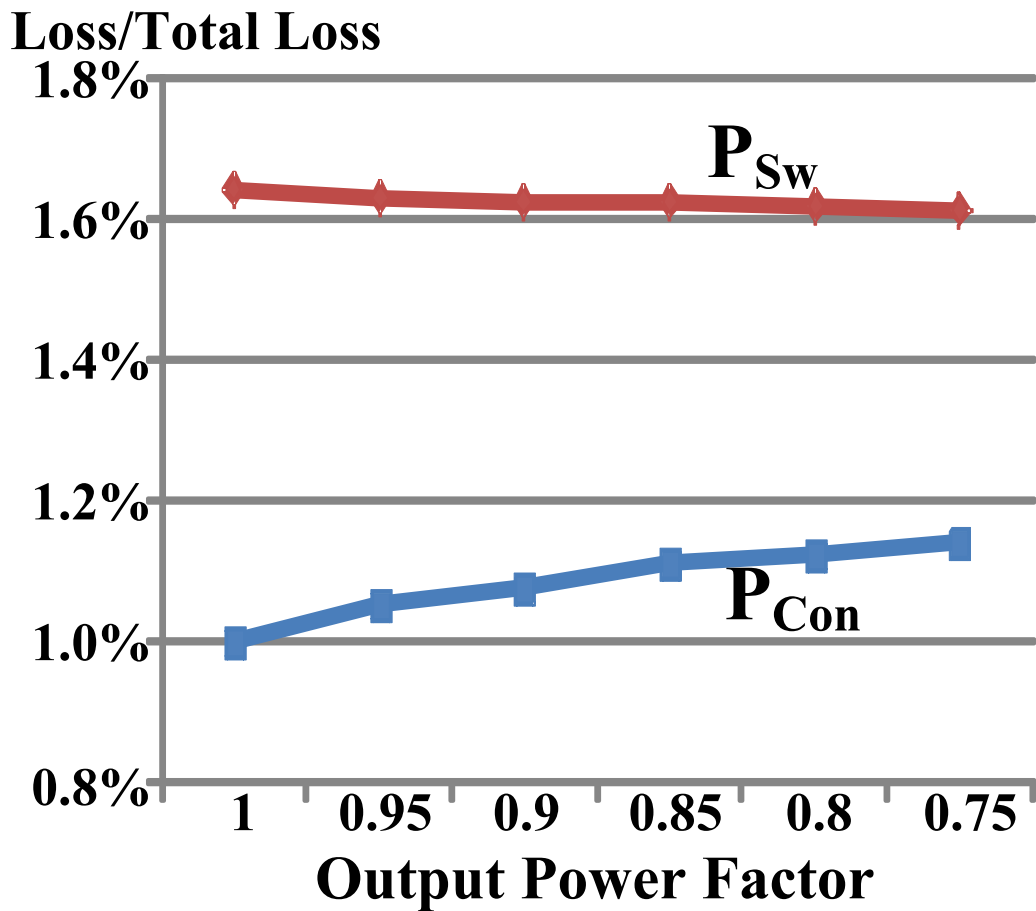


Figure 42. Loss vs. Output Power Factor.

Simulation Results

The simulation parameters are the same as those given in the efficiency calculation shown in Table 3. The driving signals of three switches (S_{aT} , S_{aM} , S_{aB}) are shown in Figure 43. Figure 44 shows the measured grid-side current and output line-to-line voltage with unity power factor operation. It should be noted that the control of the rectifier and inverter is decoupled, and therefore, the inverter operation will not affect the operation of the rectifier. The harmonic spectrum distribution is presented in Figure 45.

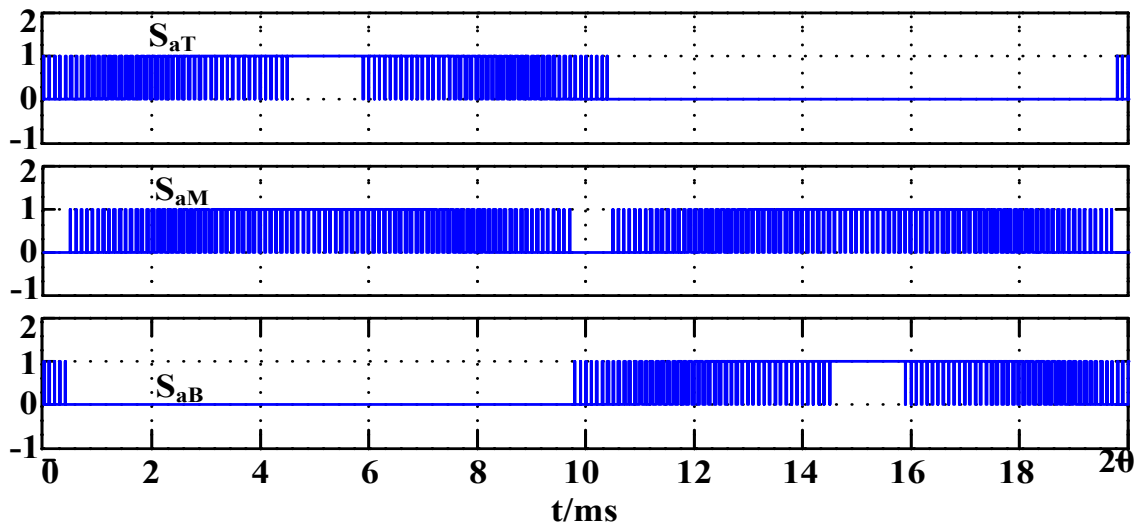


Figure 43. Driving signals.

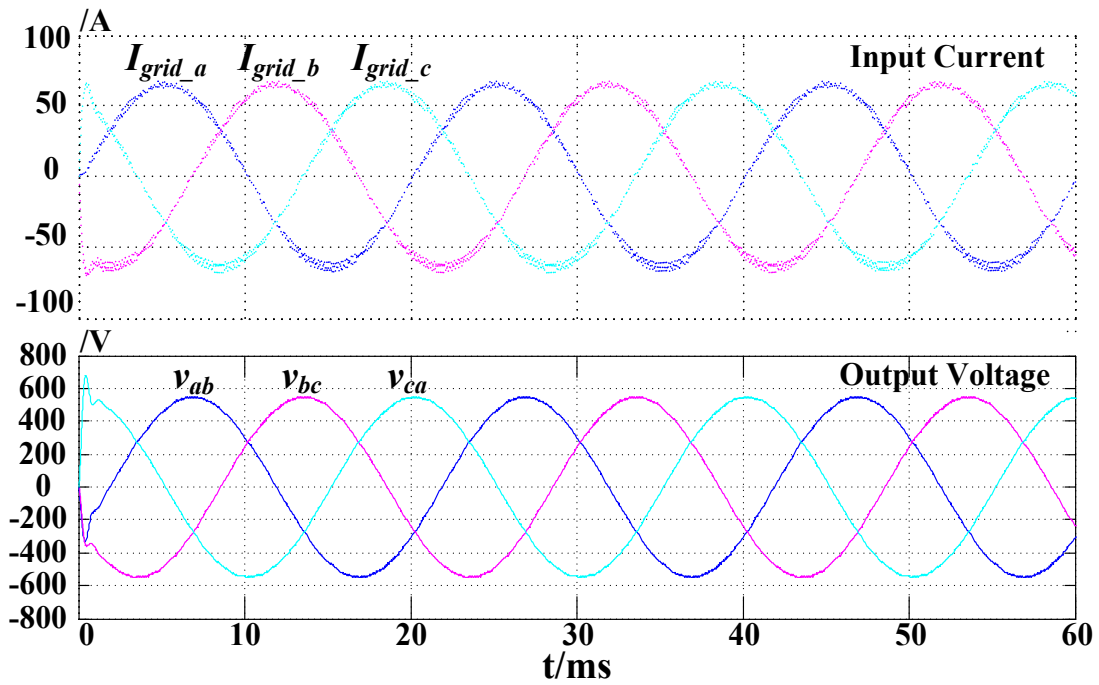


Figure 44. Input and Output waveforms.

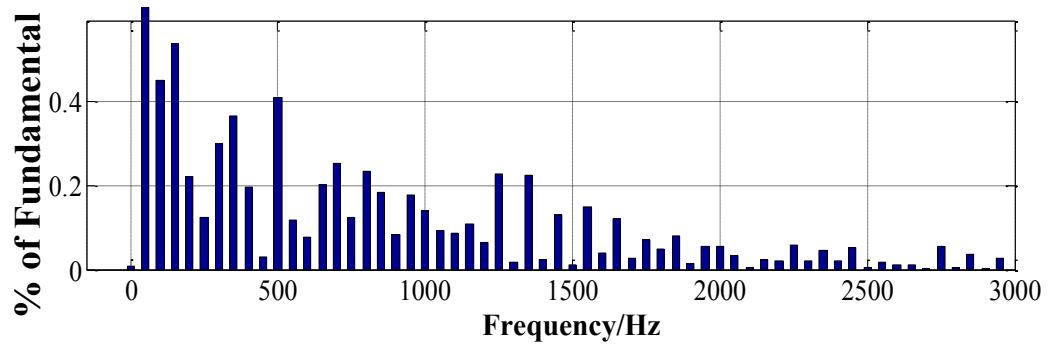


Figure 45. Harmonic spectrum distribution of output voltage.

Since the proposed topology inherits favorable 3-level converter characteristics, the THD of the output voltage is lower compared to the nine-switch converter shown in Figure 46.

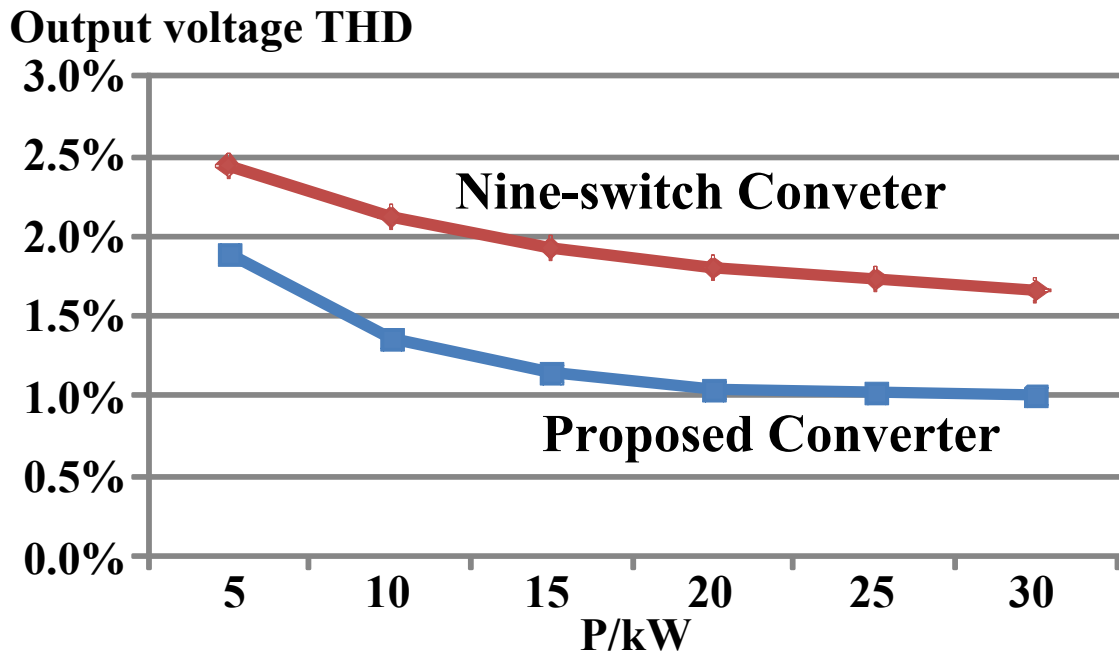
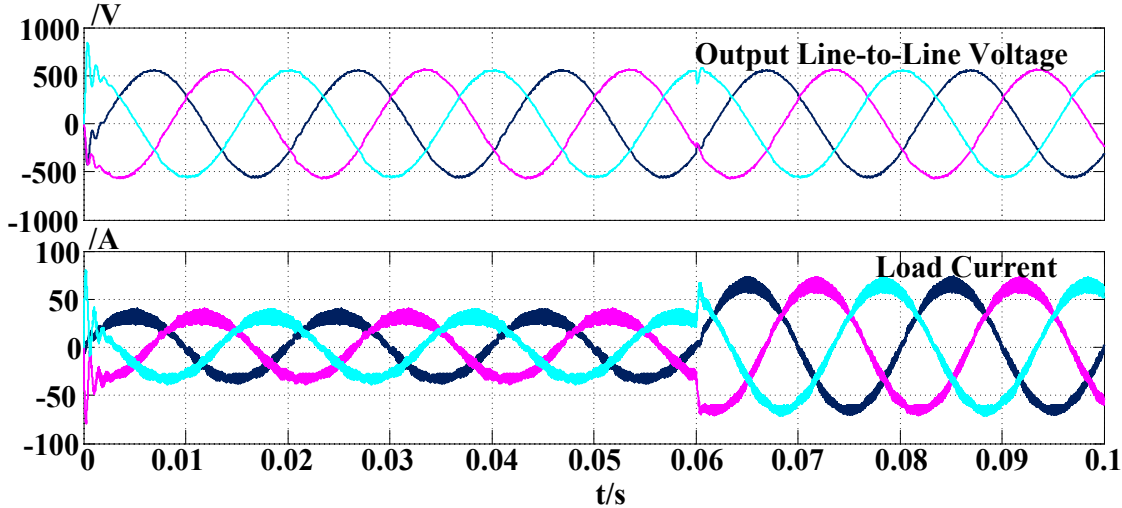
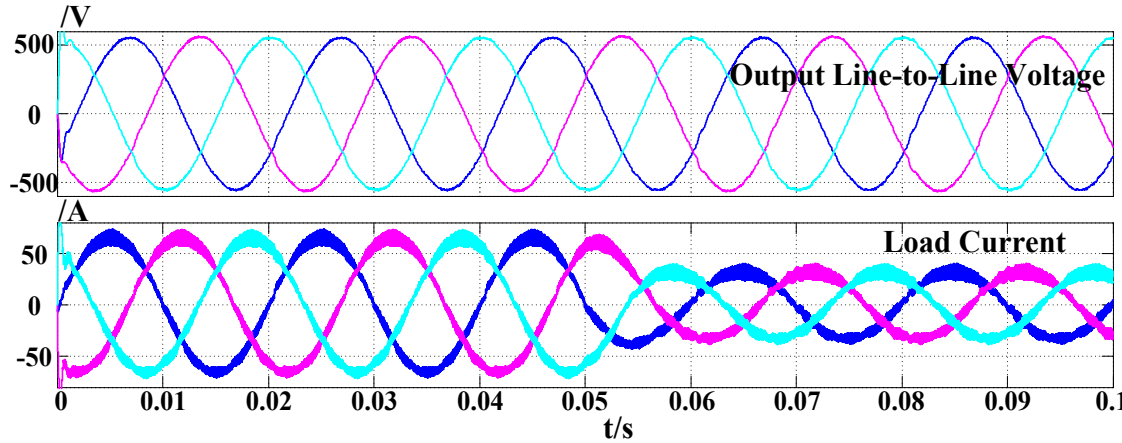


Figure 46. THD comparison of proposed converter and 9-switch converter.

Figure 47 shows the dynamic response of the proposed converter when the load steps between 15kW and 30kW. It can be seen that the load voltage is maintained smoothly and the voltage drop is quite small.



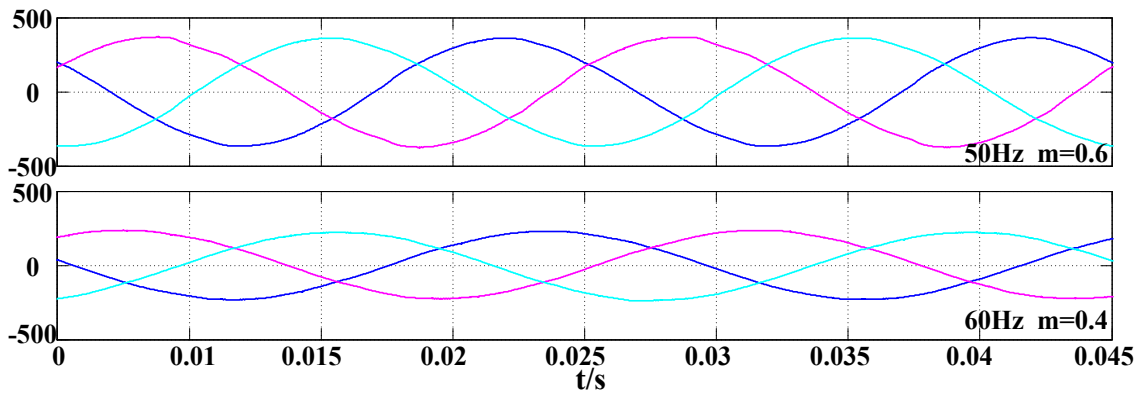
(a) Load steps up from 15kW to 30kW at 0.06s



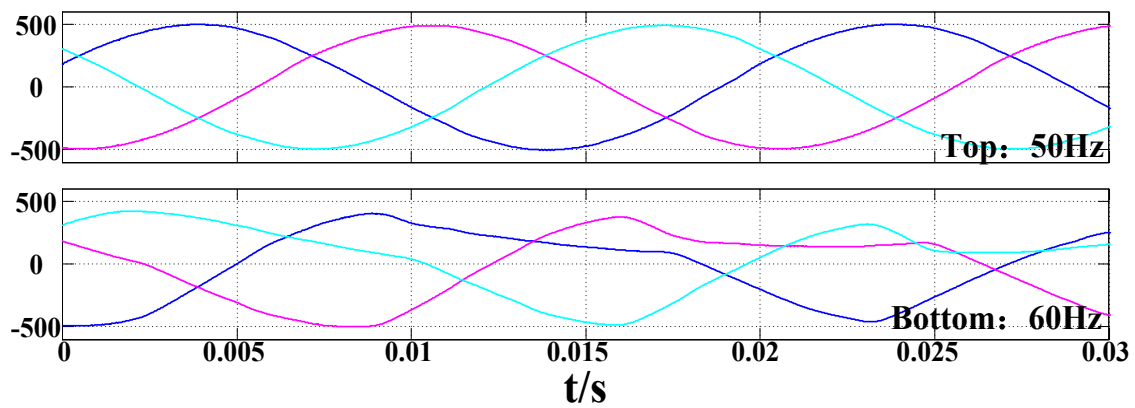
(b) Load steps up from 30kW to 15kW at 0.05

Figure 47. Dynamic response under abrupt load variations.

As previously analyzed, when two outputs of this converter are operated at different frequency, the modulation index sum of both sets will be restricted to unity. Figure 48a shows the voltage waveforms when $m_{Top}=0.6$ (50Hz), $m_{Bottom}=0.4$ (60Hz) and $m_{Top}+m_{Bottom}=1$. If $m_{Top}+m_{Bottom}>1$, the output voltage of the bottom set will be distorted as shown in Figure 48b.



(a) $m_{Top}=0.6$ (50Hz), $m_{Bottom}=0.4$ (60Hz)



(b) $m_{Top}=0.8$ (50Hz), $m_{Bottom}=0.8$ (60Hz)

Figure 48. Input and Output Voltage Waveforms when the converter is operated in DF mode.

Conclusion

A component minimized dual output multi-level converter topology with reduced number of switches has been proposed. Three typical applications for the proposed converter were explained, and the dc-bus utilization was calculated. It has been shown that there is no reduction of the modulation index when both sets of output voltages have the same frequency and same phase. In the online UPS application, the efficiency was analyzed to demonstrate that the proposed converter achieves at least 0.5% higher efficiency compared to the traditional back-to-back 3-level converter while employing less number of switches. Finally, simulation results have been shown to demonstrate the validity of proposed topology.

CHAPTER V

THE MODULAR FUEL CELL WITH HYBRID ENERGY STORAGE CONVERTER

Introduction and Concept Overview

Fuel Cells are relatively new in the energy market in comparison to most other available DERs. Very similar to batteries, they convert chemical energy from into electrical energy. However, they differ in the fact that FCs are slightly more energy-dense and can operate indefinitely (as long as there is a constant flow of fuel), whereas batteries are more power-dense and have an operation time directly limited to the amount of chemical “fuel” stored inside of their own packaging. Being such consistent base-load generation sources, FCs have proven their utility inside of large scale power generation up into the MW-range. Besides high-power generation, FCs have become viable options when sourcing smaller-scale power for transportation, auxiliary power, and military applications.

Altogether, FCs have stormed the energy market with annual growth rates that have soared to a very solid projection of 16.6% through 2014 [59]. High efficiencies, silent operation, zero pollutant outputs, superb energy density, low maintenance, high reliability, and a broad range of power outputs and fuel selections are many of the reasons FCs have been so successful. Although there are plenty of future infrastructure challenges for FCs, they have undeniably fought their way into a rather permanent-looking position of competition with the more traditional choices of batteries and gas turbines.

The proposed MFC+HES system specifically addresses improving FC efficiency in lower power applications, while improving the system power-density with the integration of an HES for time-limited current boost requests from the load. Unique fault-tolerance capability enhances the robustness of the system.

In order to understand the concepts proposed in this section, conventional system standards and the concepts of hybridization, modularization, and source modeling are first presented. Then, the design and analysis of the proposed topology is discussed in detail.

System Modularization

Fuel cells are electrochemical devices that produce electric power by combining a hydrogen based fuel with oxygen. A fuel cell consists of two electrodes – anode and cathode – and an electrolyte. The voltage produced by a single fuel cell is approximately 0.8 V. So to realize a practical system, a number of fuel cells have to be stacked in series. One disadvantage encountered when using fuel cell stacks is the fact that they are not stiff voltage sources, as they exhibit a no-load to full-load output voltage variation of up to 50%. This necessitates a dc-dc converter to boost the output voltage and compensate for the voltage variation. A simple conventional fuel cell system thus takes the form as shown in Figure 49.

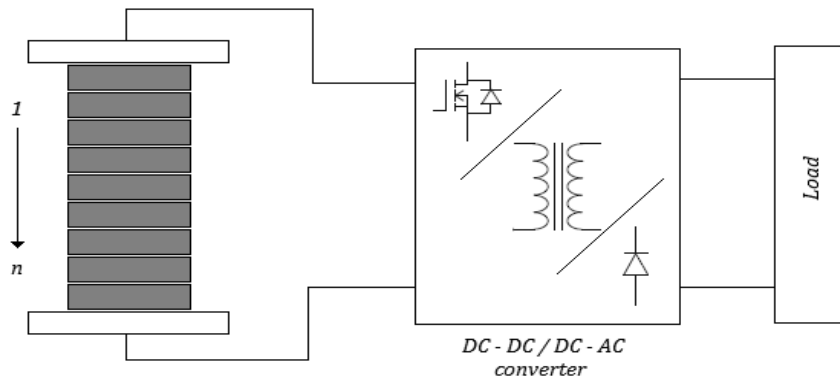


Figure 49. Conventional fuel cell stack (n cells) with two end terminals and an isolated dc-dc converter.

A modular fuel cell system can be created by dividing a large fuel cell stack into several smaller electrically subdivided stack sections as illustrated in Figure 50 below. A dc-dc converter with an energy storage buffer is then used to interface each subdivided stack section with the load (see Figure 51). In this specific topology, the modules have their own dc-dc converters and they are connected at the output.

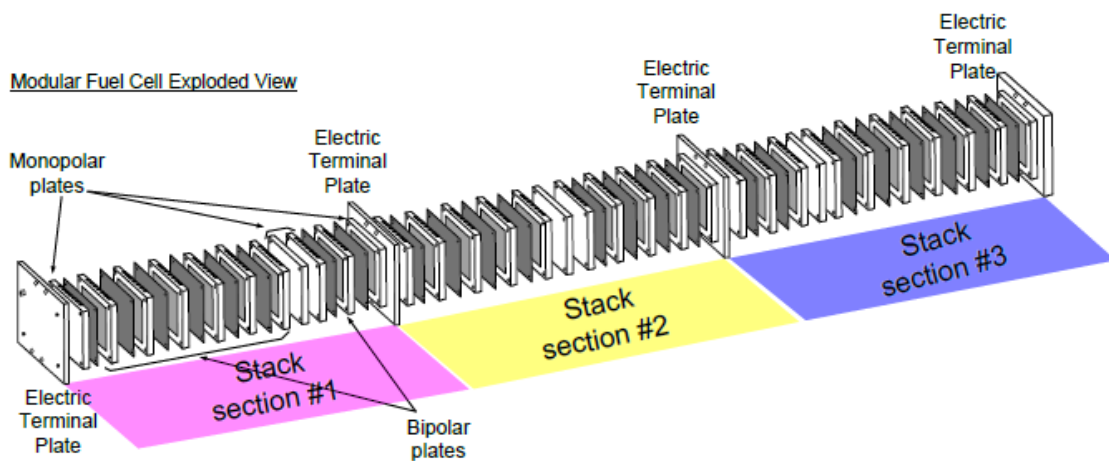


Figure 50. Exploded view of a modular fuel cell with three stack sections.

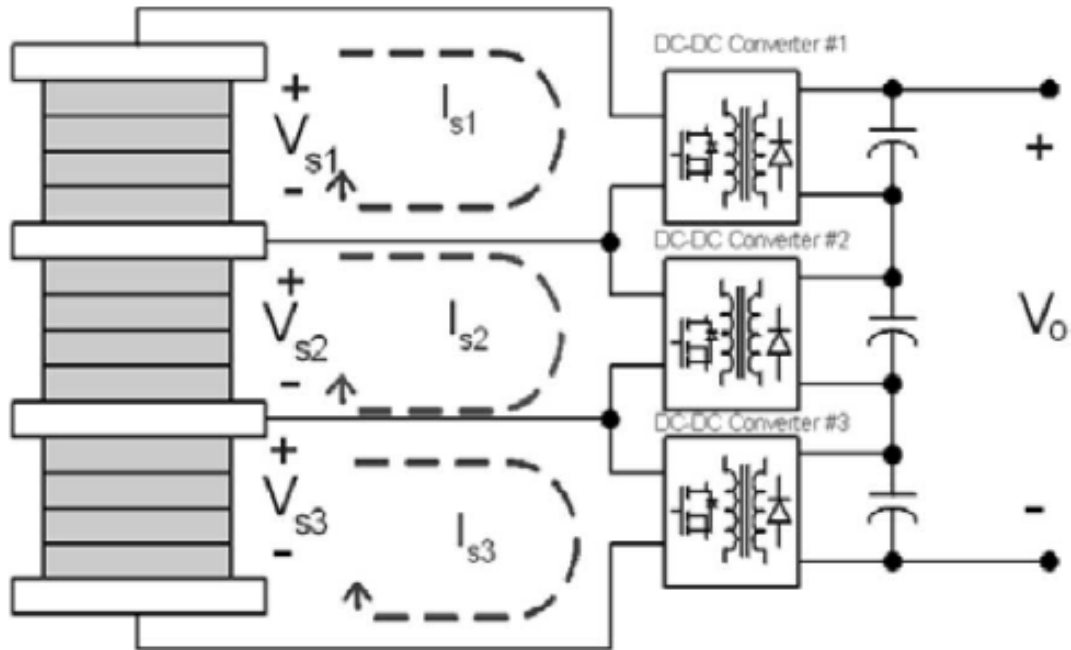


Figure 51. Modular fuel cell and dc-dc converter concept with three sections.

Many advantages to this topology are realized when inspecting a 150W three-section modular fuel cell. Figure 52 and Figure 53 show the modular section voltages and currents with respect to points of power operation, and **Table 4** shows that a modular approach provides more than a 10% increase in output power in comparison to a conventional stack. This result shows that despite having underperforming cells in the system the power generated is close to the stack nominal.

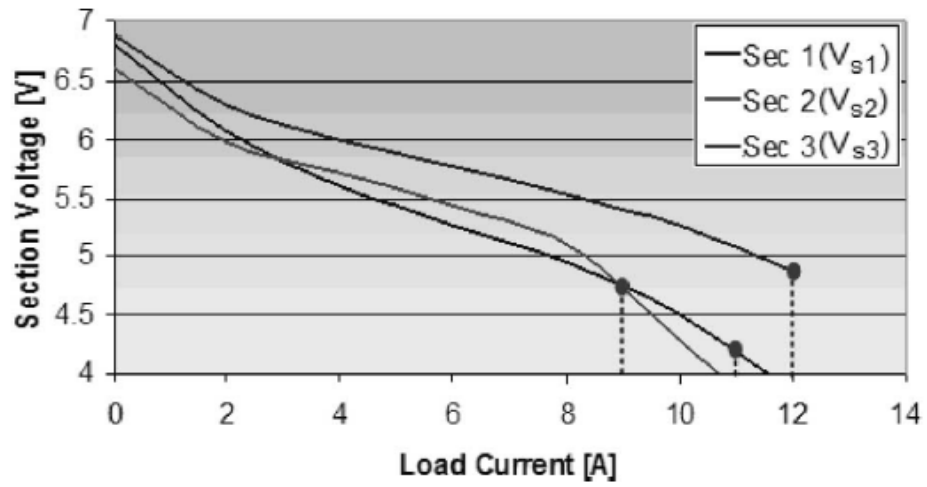


Figure 52. V-I characteristics of the 3-section modular fuel cell proposed in Figure 51.

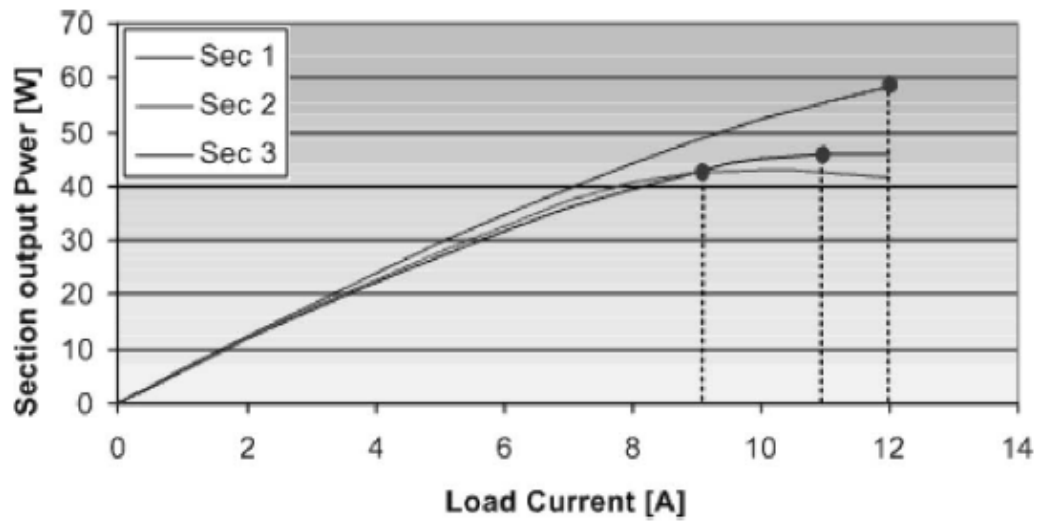


Figure 53. Output power produced by each section of the 3-section modular fuel cell proposed in Figure 51.

Table 4: Conventional and modular approach comparison

	Conventional	Modular
Section 1	42 W	42 W
Section 2	43 W	47 W
Section 3	49 W	58 W
Total power	134 W	147 W

To further verify the effectiveness of the modular approach, thermal images of the fuel cell stack operating in both single stack and modular stack modes were taken. Figure 54 and Figure 55 shows a thermal image of the prototype stack operating in conventional mode. Load current in this case is 7.25 A, and the voltage of the stack was measured to be 12 V, which is the nominal voltage of the fuel cell for full-load. The power generated by the stack operating under this condition was measured to be 87 W. It can be observed that the temperature distribution is quite uneven due to the presence of bad cells in Section 2, while Sections 1 and 3 show a lower temperature indicating that they are underused.

The result of reconfiguring the stack for modular operation and the use of the proposed dc–dc converter is shown in Figure 54 and Figure 55. In this case, the voltage across each of the sections was regulated by the dc–dc converter modules to 4 V, i.e., the nominal voltage for each section. The currents drawn from Sections 1–3 in the stack were measured to be 10, 6, and 9 A, respectively. Thus, the power generated by the fuel cell in this case is 102 W. As can be seen from Figure 55, the temperature distribution within the stack in this case is even, indicating full utilization of the three sections. Moreover, due to the use of the modular approach, the fuel cell generates 15% more power than in the conventional case (see Figure 54).

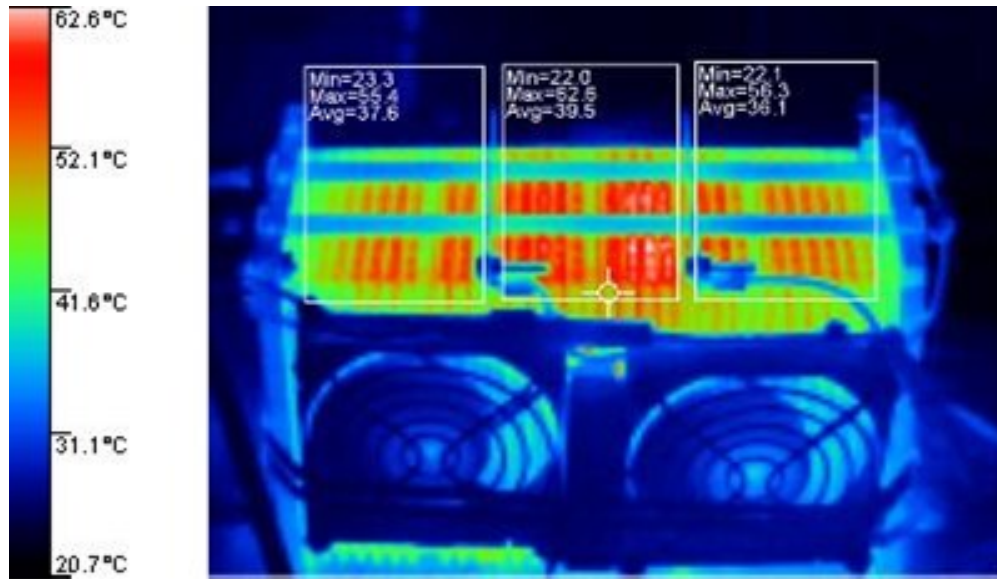


Figure 54. Thermal imaging of a conventional fuel cell stack, showing temperature imbalance.

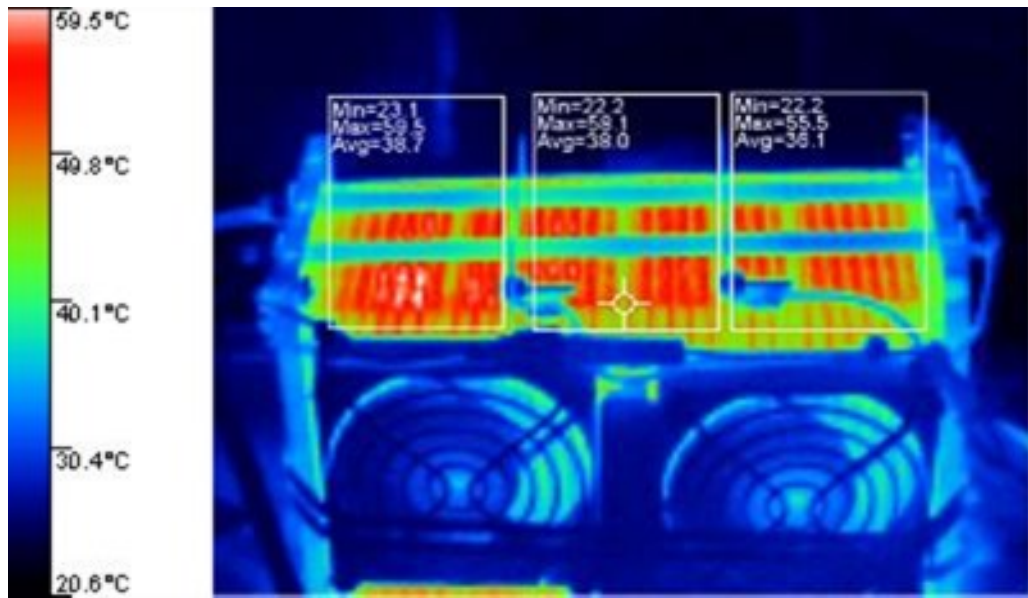


Figure 55. Thermal imaging of a modular fuel cell stack, showing temperature balance.

The other functionality offered by the proposed converter is the ability to discard a section of the fuel cell if the controller detects that the voltage across its terminals drops below a certain threshold level. Here, the prototype fuel cell is rated for 12V at full load, and the nominal voltage of each of the sections at full-load is 4V. Therefore, if a section is faulty, its terminal voltage will fall below this value. For this reason, the threshold level in the controller was set to 3.8 V. Figure 56 shows the behavior of the system when a faulty section is detected, where Ch. 1 corresponds to the current drawn from Section 3 (I_{s3}), Ch. 3 the output voltage of the dc–dc converter (V_o), and Ch. 4 the current drawn from Section 2 (I_{s2}).

In this case, Section 2 in the stack is faulty, and it has to be discarded to avoid stack shutdown due to overheating. As can be seen in Figure 56, once the fault condition is detected, the current drawn from the faulty section (Section 2) falls to zero. In order to maintain the output voltage of the system constant, the currents drawn from the remaining sections in the stack (I_{s1} and I_{s3}) have to increase. This can be observed from Figure 56, where the current supplied by Section 3 (I_{s3}) increases from 5A to 7A after Section 2 is discarded. The increase in the magnitude of the currents drawn from the remaining sections is regulated in terms of their relative health as determined by the converter control. As can be seen from these results, the system can continue operation despite having a faulty section; thus, the modular approach exhibits higher reliability than the traditional approach.

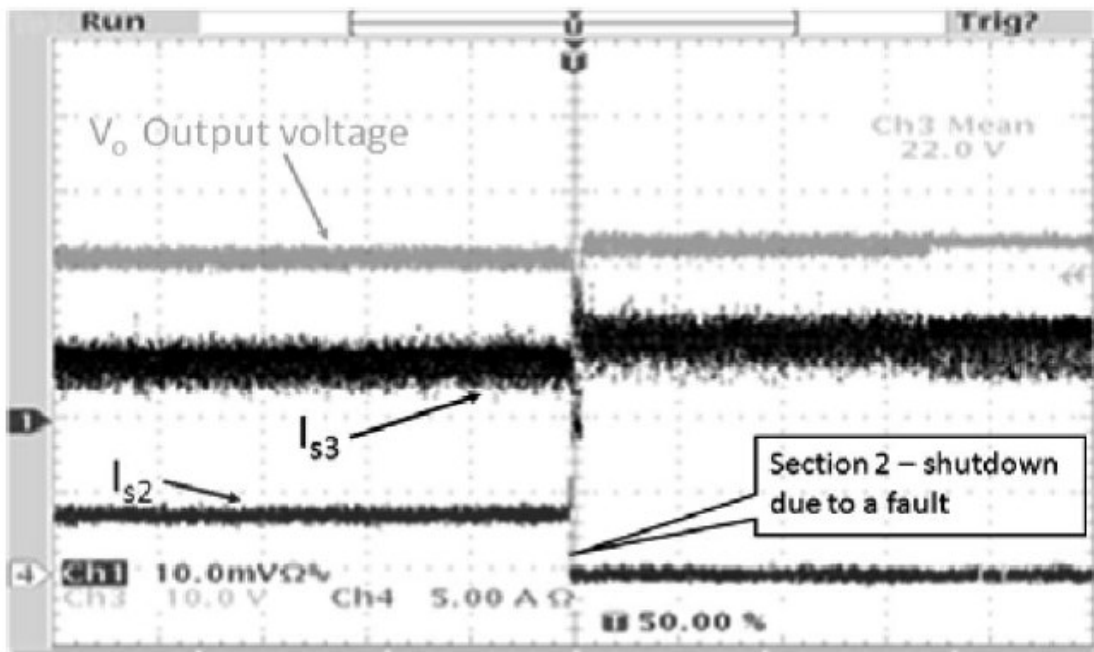


Figure 56. Operation of the modular fuel cell modular dc-dc converter under a fault. Note: Section 2 current is reduced to zero, while the output voltage continues to be regulated.

Overall, modularization of a fuel cell system has many advantages: it is more tolerant under fuel cell and/or converter fault conditions, it is capable of supplying partial load power if one stack section is damaged or disconnected, and it distributes heat more evenly throughout the cell while maximizing the power delivery from each stack section.

System Hybridization

There are two major drawbacks to using FCs in DERS: (1.) FC performance is significantly influenced by rapidly changing load demands and (2.) FCs are electrically slow compared to most electrical Energy Storage Devices (ESDs). These issues are extremely problematic when the system is expected to supply sudden increases in high output power (e.g., motor start-ups, uninterruptible power supplies, etc.). With this said, it is desirable to pair them together when designing a system. Not only do hybrid systems have quicker responses to extreme load variation, but they also realize increased longevity for both FCs and ESDs alike. The Ragone Plot in Figure 57 offers a visual comparison of relevant DES energy- and power-density characteristics.

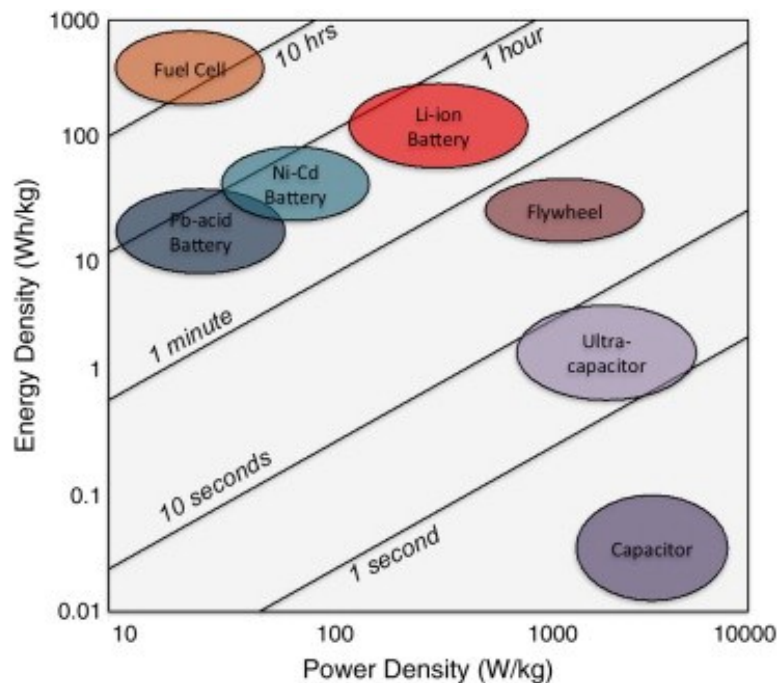


Figure 57. This Ragone Plot illustrates how SCs and LIBs are legitimate candidates for the quick response ESD hybridized with the MFC.

Traditional, non-modular hybrid systems interface the FC with the load via an isolated dc-dc converter (see Figure 58). Depending on the output voltage requirements, flyback, forward, or full-bridge converters are all appropriate candidates. The battery bank charges and discharges through its own separate dc-dc converter, whose output is connected to the load in parallel with the output of the FC's isolated converter. It is common for the FC's converter to be voltage-mode controlled while the battery's converter is current-mode controlled. This specific topology allows for energy to be stored in the ESDs and extracted when demanded by the load (see Figure 58), and proved useful when providing 200% current for 10 seconds in an automotive/emergency power supply system.

Source Modeling

Accurate source modeling plays an important role in system design for the MFC+HES. This section discusses various FC and LIB circuit models, and selects the most realistic representation for each.

Lithium-Ion Battery Circuit Model

There are five popular electrical circuits used to model LIBs: the R_{int} Model, the RC Model, the Thevenin Model, the PNGV Model, and the Dual Polarization Model [60]. Their architectures are illustrated in Figure 59 through Figure 63, respectively.

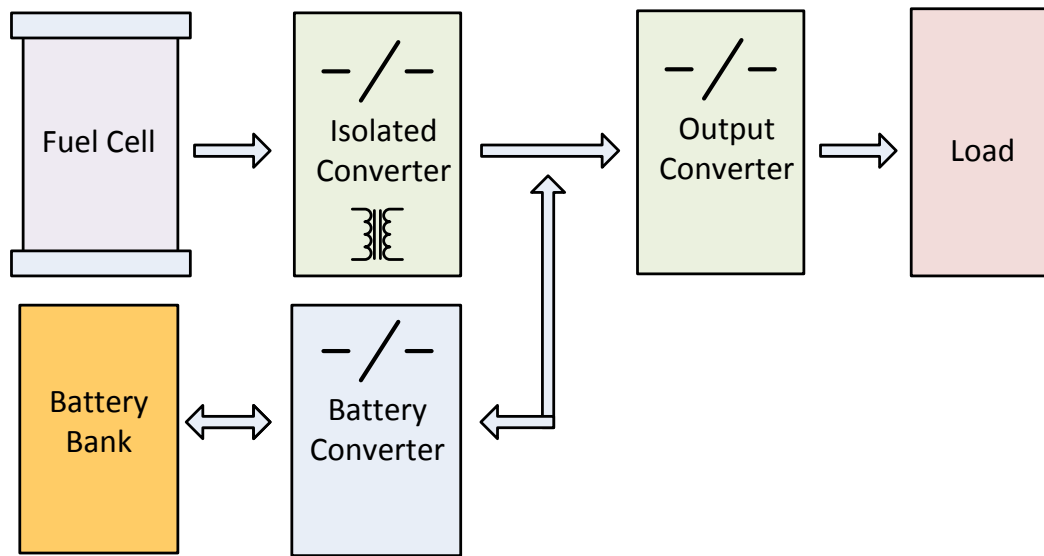


Figure 58. Non-modular fuel cell system connected with a high-power energy storage device and interfaced with dc-dc converters

The R_{int} Model

As shown in Figure 59, the R_{int} model represents the battery's open-circuit voltage with ideal voltage source V_{oc} , and a single series resistance R_o is used to model internal resistances associated with temperature, state of health, and state of charge. The terminal voltage is governed by the following equation:

$$V_L = V_{oc} - I_L R_o. \quad (5.1)$$

Statistical analysis performed in [60] shows this model to have a 2.82% terminal voltage error.

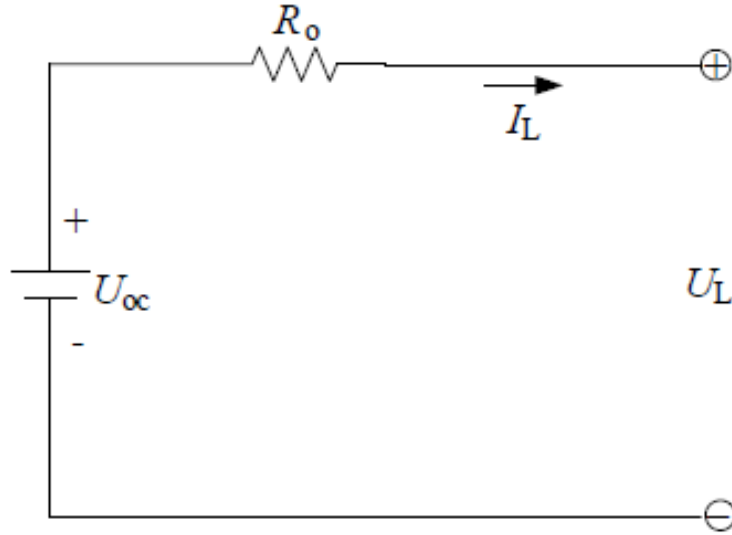


Figure 59. Review of LIB Models: The R_{int} Model.

The RC Model

As shown in Figure 60, the RC Model has five components: the surface capacitor (C_c), the capacitor resistor (R_c), the bulk capacitor (C_b), the end resistor (R_e), and the terminal resistor (R_t). This model breaks up the LIB circuit such that state of charge can be measured across the bulk capacitor. The following equations describe its operation:

$$\begin{bmatrix} \dot{V}_b \\ \dot{V}_c \end{bmatrix} = \begin{bmatrix} \frac{-1}{C_b(R_e + R_c)} & \frac{1}{C_b(R_e + R_c)} \\ \frac{1}{C_c(R_e + R_c)} & \frac{-1}{C_c(R_e + R_c)} \end{bmatrix} \begin{bmatrix} V_b \\ V_c \end{bmatrix} + \begin{bmatrix} \frac{-R_c}{C_b(R_e + R_c)} \\ \frac{-R_e}{C_c(R_e + R_c)} \end{bmatrix} [I_L] \quad (5.2)$$

$$[V_L] = \begin{bmatrix} \frac{R_c}{(R_e + R_c)} & \frac{R_e}{(R_e + R_c)} \end{bmatrix} \begin{bmatrix} V_b \\ V_c \end{bmatrix} + \left[-R_t - \frac{R_e R_c}{(R_e + R_c)} \right] [I_L] \quad (5.3)$$

Statistical analysis performed in [60] shows this model to have a 2.03% terminal voltage error.

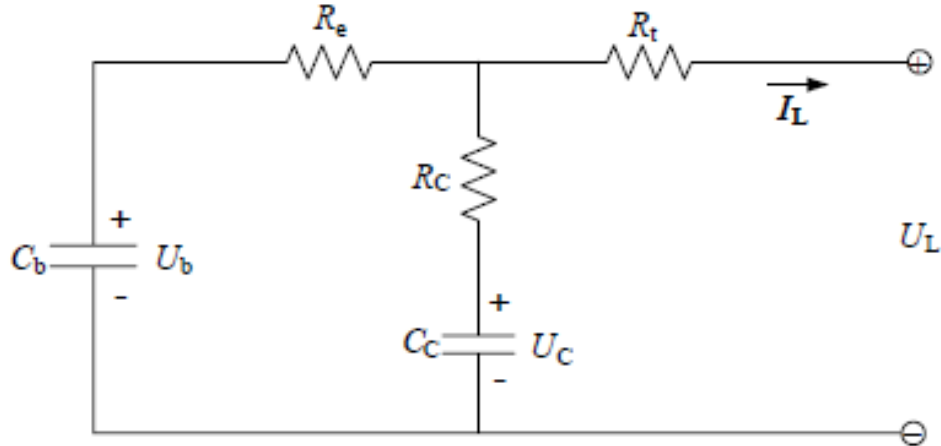


Figure 60. Review of LIB Models: The RC Model.

The Thevenin Model

As illustrated in Figure 61, the Thevenin Model models the LIB's transient response characteristics by connecting a parallel RC network in series with the R_{int} model. The polarization resistance (R_{Th}) and the equivalent capacitance (C_{Th}) comprise the additional components. This model works well for accurately modeling the current response of an LIB, and obeys the following equations.

$$\dot{V}_{Th} = \frac{-V_{Th}}{R_{Th}C_{Th}} + \frac{I_L}{C_{Th}} \quad (5.4)$$

$$V_L = V_{oc} - V_{Th} - I_L R_o \quad (5.5)$$

Statistical analysis performed in [60] shows this model to have a 0.52% terminal voltage error.

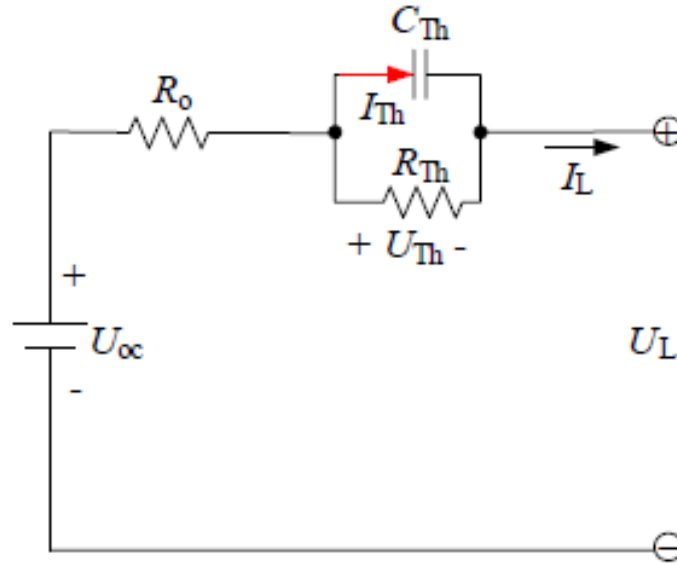


Figure 61. Review of LIB Models: The Thevenin Model.

The PNGV Model

As shown in Figure 62, the Partnership for a New Generation of Vehicles (PNGV) Model takes into account the change in open-circuit voltage characteristics by adding a series capacitance ($1/V_{oc}$) to the Thevenin Model. The PNGV Model obeys the following equations.

$$\dot{V}_d = V'_{oc} I_L \tag{5.6}$$

$$\dot{V}_{PN} = \frac{-V_{PN}}{R_{PN} C_{PN}} + \frac{I_L}{C_{PN}} \tag{5.7}$$

$$V_L = V_{oc} - V_d - V_{PN} - I_L R_o \tag{5.8}$$

Statistical analysis performed in [60] shows this model to have a 1.00% terminal voltage error.

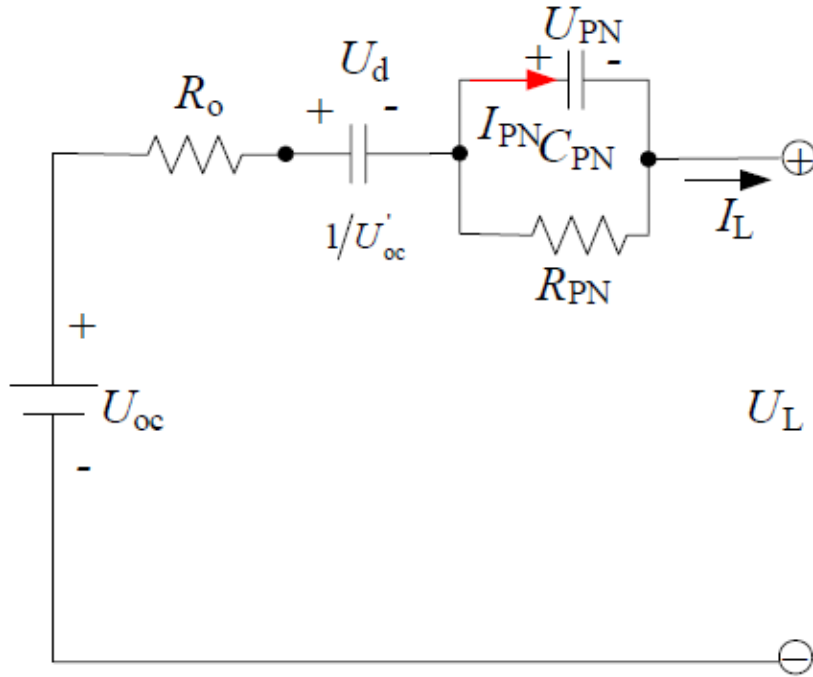


Figure 62. Review of LIB Models: The PNGV Model.

The Dual Polarization Model

As seen in Figure 63, the Dual Polarization Model adds two parallel RC networks in series with the R_{int} Model. Electrochemical polarization and time response are modeled by R_{pa} and C_{pa} , and concentration polarization and time response are modeled by R_{pc} and C_{pc} . R_o continues to represent the ohmic losses of the system.

$$\dot{V}_{pa} = \frac{-V_{pa}}{R_{pa}C_{pa}} + \frac{I_L}{C_{pa}} \quad (5.9)$$

$$\dot{V}_{pc} = \frac{-V_{pc}}{R_{pc}C_{pc}} + \frac{I_L}{C_{pc}} \quad (5.10)$$

$$V_L = V_{oc} - V_{pa} - V_{pc} - I_L R_o \quad (5.11)$$

Statistical analysis performed in [60] shows this model to have a 0.38% terminal voltage error.

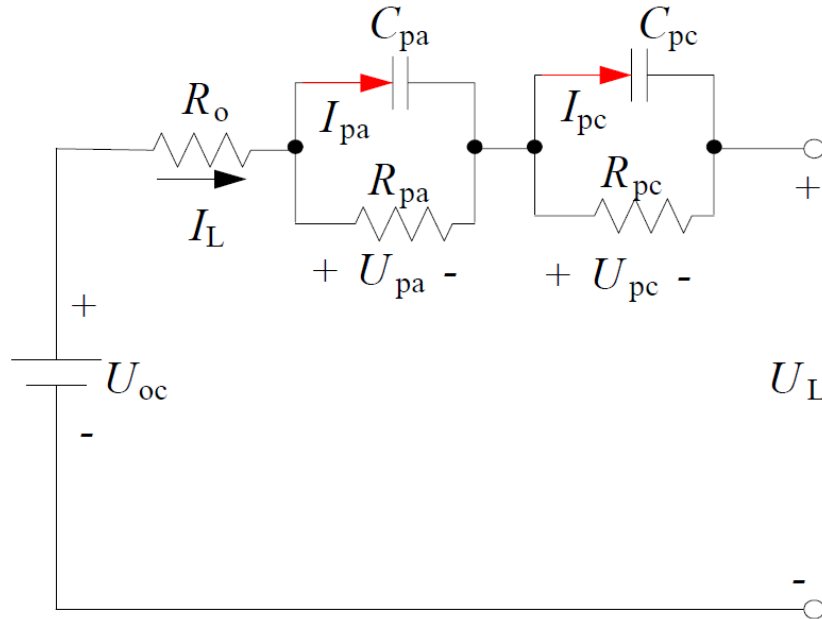


Figure 63. Review of LIB Models: The Dual Polarization Model.

Fuel Cell Electrical Circuit Model

A series resistance model similar to the LIB's R_{int} Model is often used to simulate the electrical behavior of a FC. In cases, such as the aforementioned Power Sharing Converter System, it is acceptable to do this because the FC's transient response does not dramatically affect the system control. However, in the case of the MFC+HES, this is not the case. Therefore, a more accurate model must be chosen to better represent the time transient behavior.

Reference [61] proposes a second order electrical circuit model of a Proton Exchange Membrane (PEM) FC (see Figure 64). R_m models the membrane resistance.

R_{p1} and C_1 represent the anode electron transfer time constant. R_{p2} and C_2 represent the cathode electron transfer time.

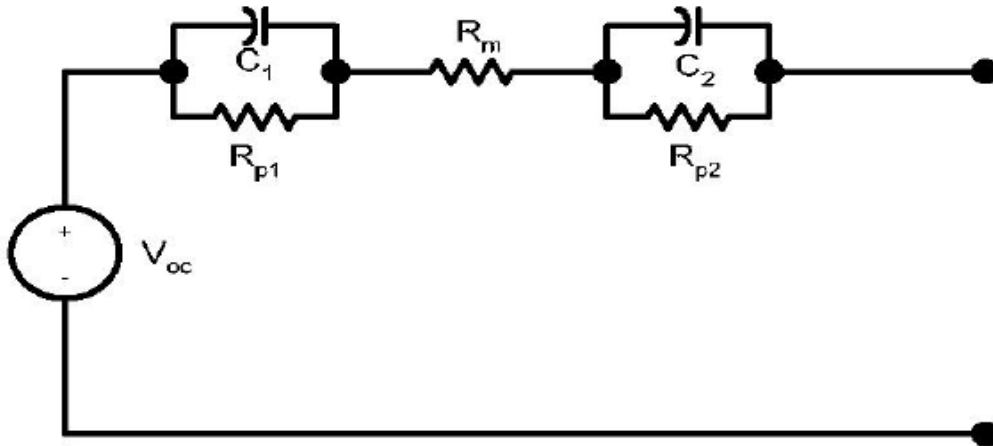


Figure 64. The second order electrical equivalent model of a PEM FC on the basis of electrochemical description.

This model is unique in the fact that it represents time transients associated with the redox reactions that occur separately in both the anode and the cathode of the FC.



A Nyquist plot can be made to verify the electrical circuit values for each section of a MFC stack [62]. The Nyquist Plot in Figure 65 subsequently yields the electrical circuit values used for modeling (see Table 5).

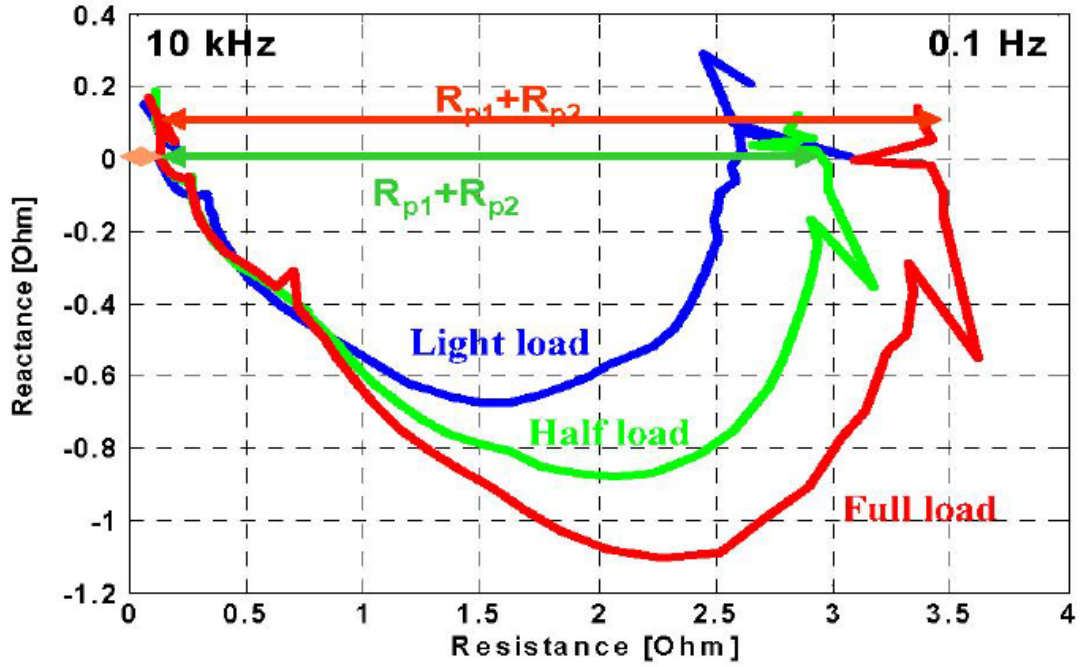


Figure 65. Nyquist Plot for a MFC stack section.

Table 5: Equivalent FC circuit values

Load	R_m (m Ω)	R_{p1} (m Ω)	C_1 (mF)	R_{p2} (m Ω)	C_2 (mF)
Light	100	684	0.622	1126	8.19
Half	100	620	0.987	1460	13.77
Full	100	615	1.277	1805	15.10

Middlebrook's Extra Element Theorem

Middlebrook's Extra Element Theorem can be used to simplify circuit design by ensuring that input resonance does not significantly modify a converter's control-to-output

transfer function. Given the system shown in Figure 66, Middlebrook's Extra Element Theorem states that a system's control-to-output transfer function is uninfluenced by input filter impedances if $Z_o \ll Z_N$ and $Z_o \ll Z_D$, where Z_N is Z_i evaluated with the converter output voltage nulled and Z_D is Z_i evaluated under the assumption that there is no variance in the control signal. This ensures that the correction factor $(1+Z_o/Z_N)/(1+Z_o/Z_D)$ tends towards unity. Equation 4.14 shows how the correction factor modifies the original control-to-output transfer function.

$$G_{vd}(s) = \left(G_{vd}(s) \Big|_{Z_o(s)=0} \right) \frac{\left(1 + \frac{Z_o(s)}{Z_N(s)} \right)}{\left(1 + \frac{Z_o(s)}{Z_D(s)} \right)} \quad (5.14)$$

By treating the equivalent circuit models of the LIBs and FC as "input filter" impedances and using Middlebrook's Extra Element Theorem, the MFC+HES converters can be designed to avoid control-to-output signal disturbance.

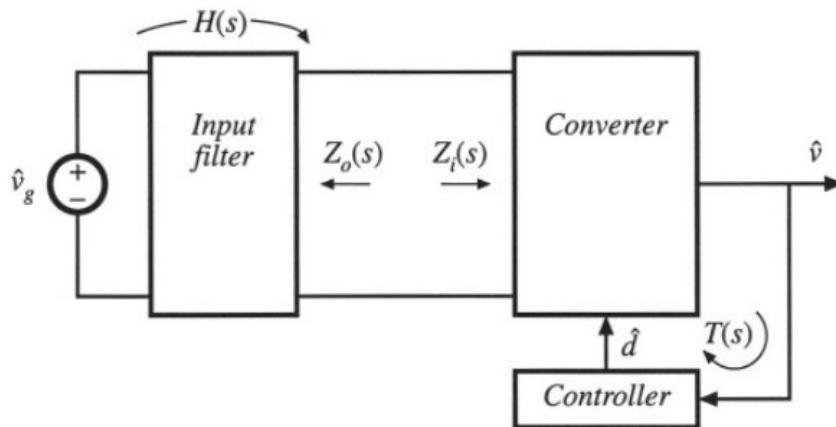


Figure 66. Middlebrook's Extra Element System.

The Modular Fuel Cell with Hybrid Energy Storage

Despite the conventional hybrid topology's advantages, the dc-dc converter gain limitations and high-power energy storage devices' low voltage ratings place a heavy constraint upon the maximum size of the fuel cell stack to which this approach can be applied. By synthesizing the concepts of *modularization* and *hybridization* the proposed system—the Modular Fuel Cell with Hybrid Energy Storage (MFC+HES)—nullifies the aforementioned constraint, while simultaneously enabling the fuel cell system to properly sustain even higher sudden power outputs for longer periods of time. The block diagram in Figure 67 illustrates how the FC stacks and hybrid ESDs are modularly interfaced with the load through a two-stage power conditioning system.

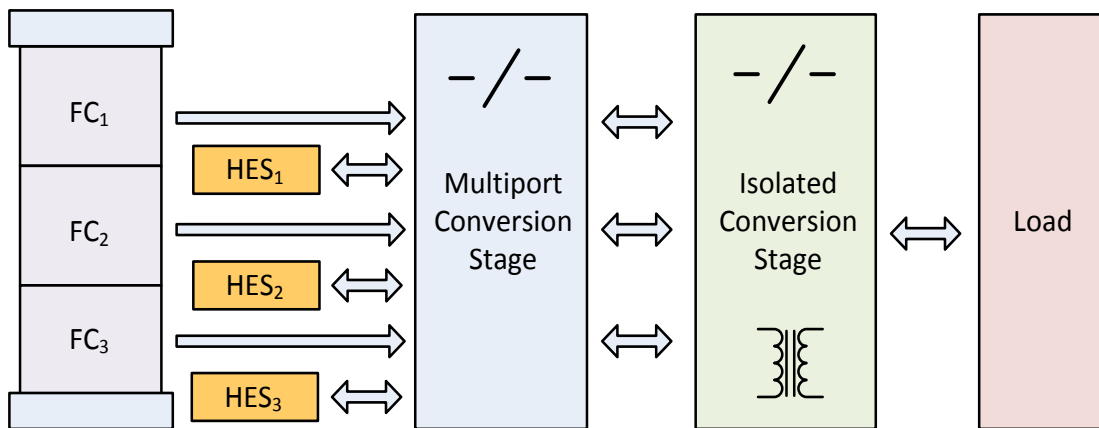


Figure 67. Modular fuel cell system connected with high-power energy storage devices and interfaced with bidirectional dc-dc converters

Altogether, the MFC+HES system achieves the following benefits over conventional hybrid systems:

- **Fault Tolerance:** operable under FC, HES, and converter fault conditions
- **Limp-Home Capability:** capable of supplying partial load power if one or more module is damaged.
- **Increased Output Power:** each module operates at its individual peak power capability.
- **Boost Current:** provides time-sustainable responses to sudden high power load demands.

Energy Storage Device Selection

In order to make an appropriate device selection for the HES stage, Maxwell's BCAP3000 (3kF SC) is compared to A123's ANR26650M1-B (2.4Ah LIB). A few assumptions are made. First, it is approximated that 70% of the energy in each device is safe to use during cycling. Second, each device is overdesigned by an energy buffer of 25%; this value is specifically designed to compensate for the reduction in energy storage capability associated with cycling/aging. Calculations show A123's LIB to be most favorable (see Table 6). It fares much better in the areas of sustained boost times, energy density, and cost savings. At the same time, it is acceptable to lower the power density, since it only requires 34.6A from each LIB to deliver the 300% boost to load. Since the LIB's ceiling for maximum continuous current discharge (50A) is not a restraint faced in

this design problem, it is clear that the SC’s 120A continuous current limit is not necessary. Cycle life is a lower priority issue both because of the limited need for 400% boost current from any load and the lower cost of replacement for LIBs. Also, the operation temperature of LIBs is sufficient for this design. Therefore, three A123 ANR26650M1-B 2.4Ah LIBs are selected to fill the ESD for this design. Table 6 summarizes why the LIB is ultimately selected. Appendix A provides deeper insight into ESD evaluation for HES systems through a detailed case study.

Table 6: Benefits and acceptable trade-offs associated with choosing between A123’s ANR26650M1-B 2.4Ah LIB and Maxwell’s BCAP3000 3kF SC.

Benefits of A123’s ANR26650M1-B 2.4Ah LIB	Acceptable Trade-Offs with Maxwell’s BCAP3000 3kF SC
Longer Boost Time (67% more)	Lower Power Density (56% less)
More Energy Dense (6.7x lighter)	Lower Cycle Life (>1k vs >1M)
Lower Cost (\$10/Wh less)	Decreased Temperature Range (19% less)

System Design Considerations

Two options are available for MPC Stage designs: high-voltage design and regular-voltage design.

High-Voltage Fuel Cell Modularization

In some cases, it may be beneficial to modularly divide the fuel cell system into fewer sections. Therefore, utilizing the synchronous multi-level high gain boost converter [63] shown in Figure 68, can be useful. This converter topology facilitates bi-directional power flow between a low voltage high-power energy storage device and a higher voltage fuel cell stack section. Such a system has many applications, including high-performance uninterruptible power supply systems.

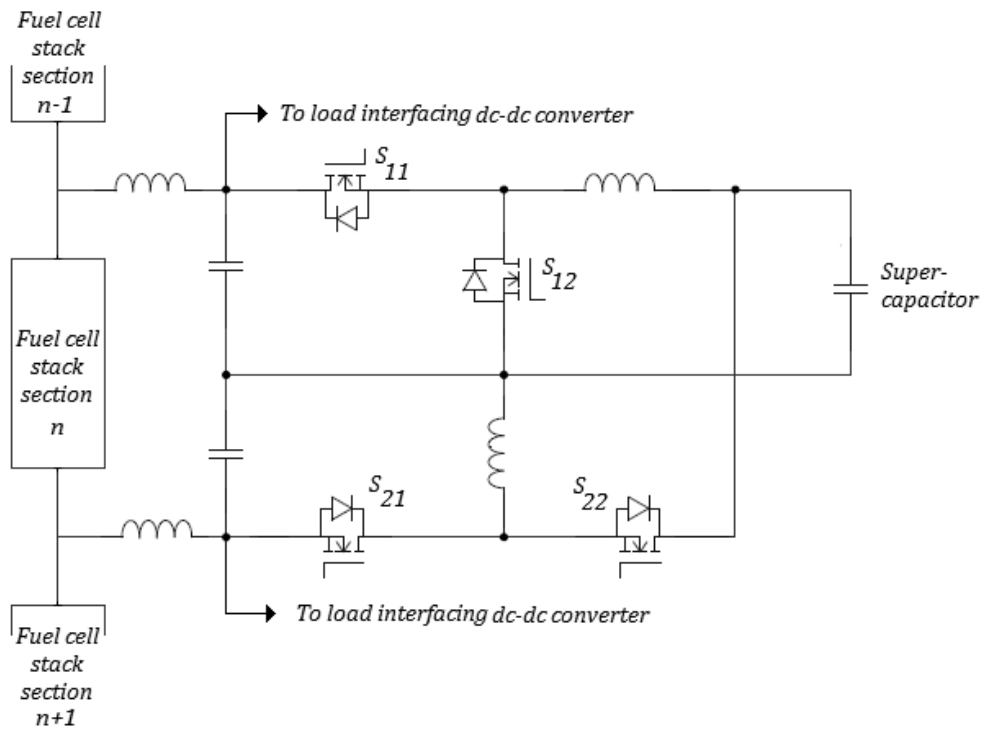


Figure 68. Proposed synchronous multi-level high-gain bi-directional converter interfacing the high-power energy storage device with the load and the hybrid fuel cell stack section.

With this specific topology, the high-power energy storage devices are sized in accordance with the energy storage requirements associated with the transient current demands specifications of the load as well as the desired discharge rate and the design fault duration. The inductors connected to each of the modular fuel cell sections are designed to dampen the impact of rapidly changing currents, while the bi-directional converter powering the high-power energy storage devices is activated. These measures reduce the stress on the fuel cells during sudden load changes, thereby increasing the life expectancy of the cells.

While energy is transferred to the ESD, the converter operates as a two level buck converter using switches S_{11} and S_{21} to enable high-power energy storage device charging. When the high-power energy storage device supplies energy, the converter operates as a high-gain two-level boost converter using switches S_{11} and S_{22} to enable high-power energy storage device discharge. This multi-level dc-dc synchronous converter is a high-gain system, which enables us to choose a lower voltage rating high-power energy storage device for interfacing [64]. Altogether, the proposed hybrid modular fuel cell system can operate in the following three modes:

- 1) *Charging mode*—The fuel cell stack supplies the load and also charges the high-power energy storage devices. The interfacing dc-dc converters operate as buck converters.
- 2) *Discharging mode*—The high-power energy storage devices supply the load along with the fuel cell stack when the load demand surges. The dc-dc converters operate in boost mode.

3) *Regenerative mode*—Energy from the load flows into the high-power energy storage devices through the synchronous dc-dc converters connecting the load.

Figure 69 illustrates the high-gain capability of this topology's non-ideal gain curve relative to the specifications given in the design example. Figure 70 illustrates the proposed high-gain converter's capability of reducing the required number of fuel cell stack sections by 15% if so desired. This figure also clearly shows how the high-power energy storage device interfacing significantly increases the current response time of the hybrid fuel cell section to high-load demands.

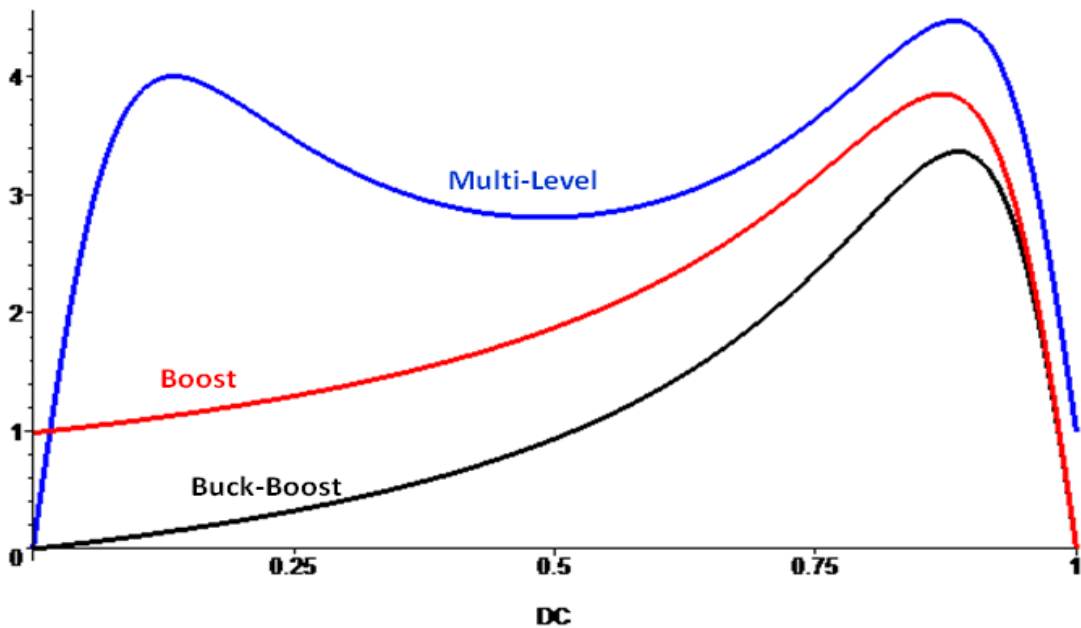


Figure 69. Proposed synchronous multi-level high-gain bi-directional dc-dc converter non-ideal gain compared to regular boost and regular buck-boost non-ideal gains. Design specs based on Section IV's design example.

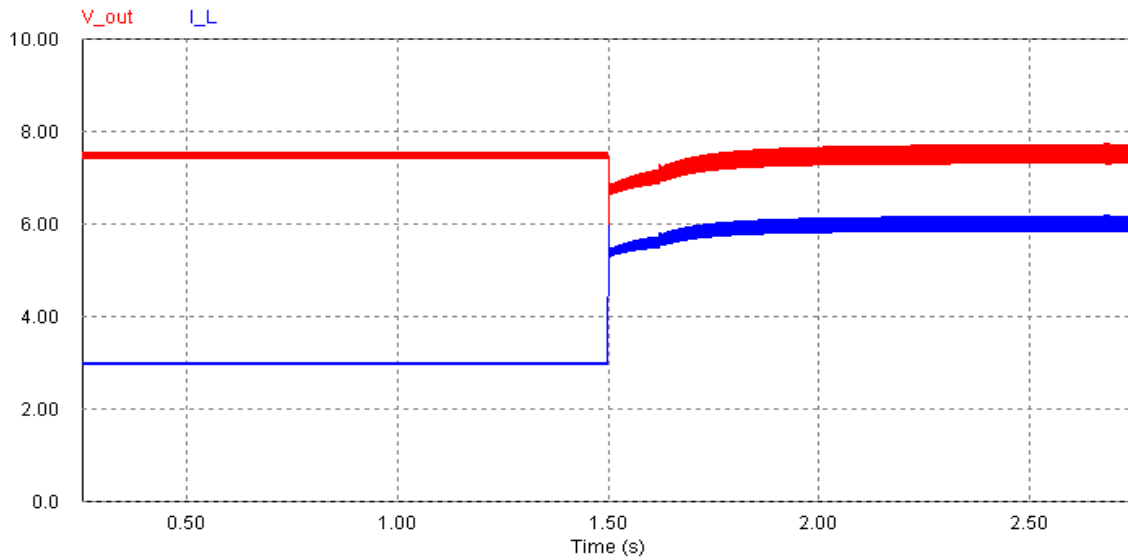


Figure 70. Simulated output voltage/current waveforms of a single fuel cell section modularly interfaced with the proposed synchronous multi-level high-gain bi-directional dc-dc converter, sustaining a 7.5V output with a 100% load increase at $t = 1.5$ s.

Regular-Voltage Modularization

In lower voltage applications (e.g., automotive applications), regular-voltage modularization should be sufficient. At this point the MPC Stage can be treated as a series string of boost converters, and design is simplified from the high-voltage scenario. For example, after selecting the LIB as the ESD unit, the MPC stage can be designed for continuous conduction mode (CCM) during both 300% Discharge Modes and 4.2C Recharge Modes, yielding the following parameters: $C_{cnv} = 3.34\text{mF}$, $L_{cnv} = 12.25$, $D = 40\text{-}50\%$, $I_{L,max} = 34.6\text{A}$, and input/output ripple voltages of 5% and 1% respectively. Figure 71 illustrates a regular-voltage series-output MFC+HES system topology.

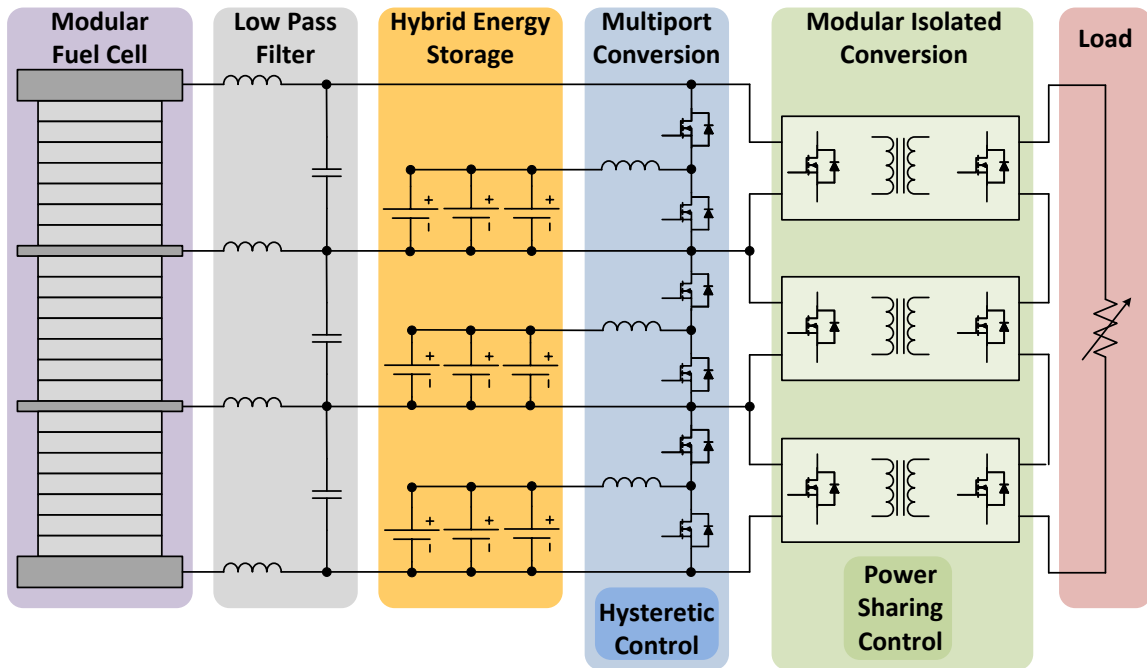


Figure 71. Regular-Voltage Series Output MFC+HES Topology.

Hysteretic Control

As seen in Figure 72, a hysteretic control method is used as sensors monitor the voltage of each section of the MFC stack. When a load demand increases each FC section drops below a set voltage limit and the HES kicks in to quickly provide the newly recognized power demand. Similarly, charging can be turned on whenever the FC voltage is above a set value. An inductor-current PI controller is recommended.

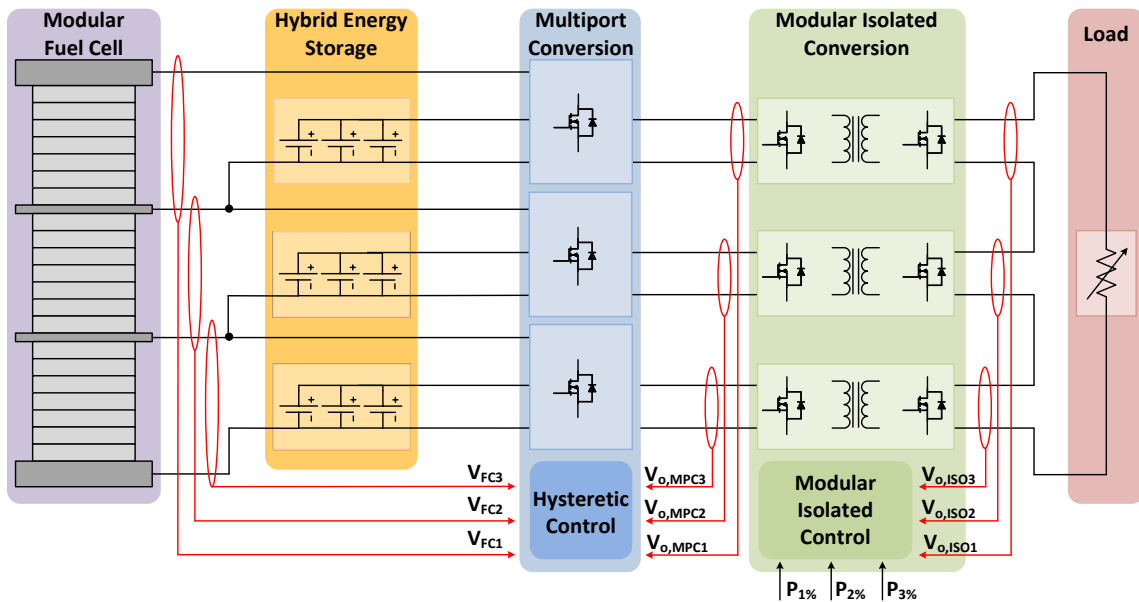


Figure 72. Hysteretic Control for the Multiport Conversion Stage of a 3-Level MFC+HES System.

Modular Isolated Conversion Stage

Depending on the load demands of the application as well as the size of the FC, series or parallel connections are viable at the output of the Modular Isolated Conversion Stage. In either case, offsetting the switching phases can reduce output harmonics.

Simulation and Hardware Results

A 90W/5A PEM MFC stack is considered. Figure 73 illustrates its VI-characteristics. These characteristics along with the LIB's are modeled in PSIM by using the second-order FC model and the Dual Polarization Models discussed earlier.

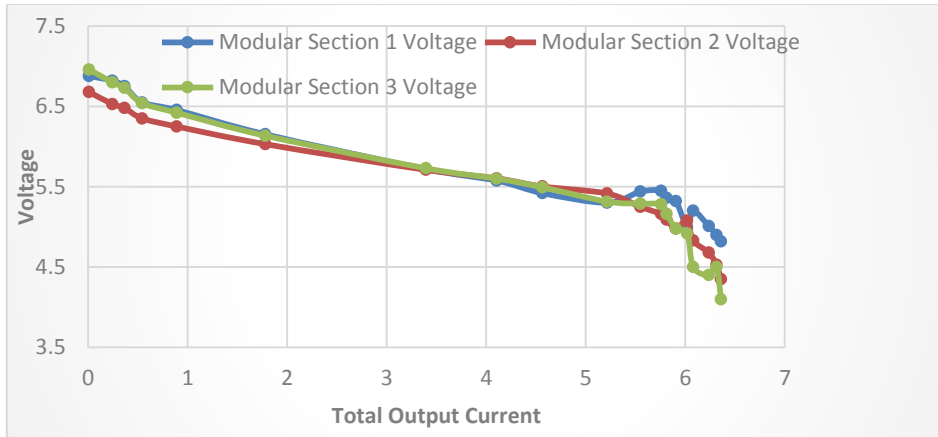


Figure 73. 90W/5A PEM MFC stack VI-characteristics.

An inductor-current PI-control for the MPC conversion stage is implemented as modeled in Figure 74. A microcontroller is used to implement the hysteretic control logic, such that whenever the fuel cell drops below 5V, the HES contributes to load demand.

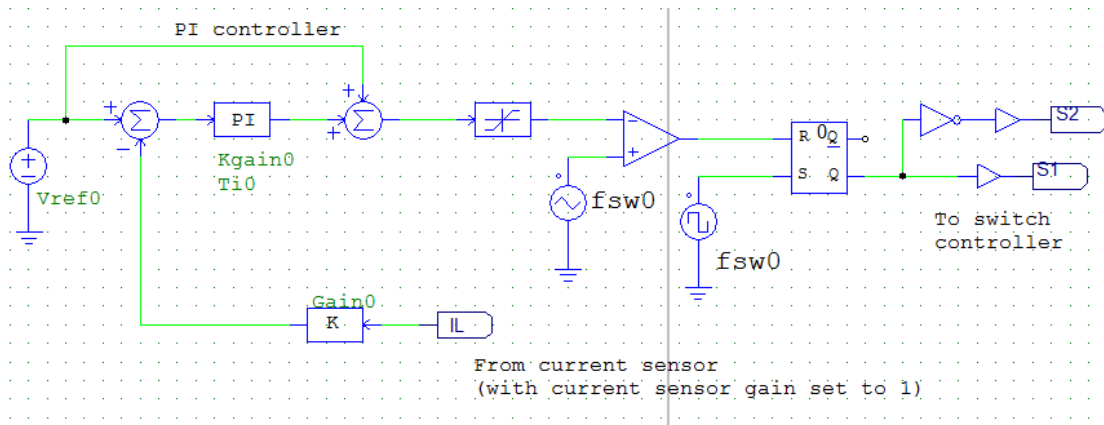


Figure 74. MFC+HES inductor-current PI-control.

Figure 75 illustrates the dynamic response of a single MFC section as load current demand increases 3-fold.

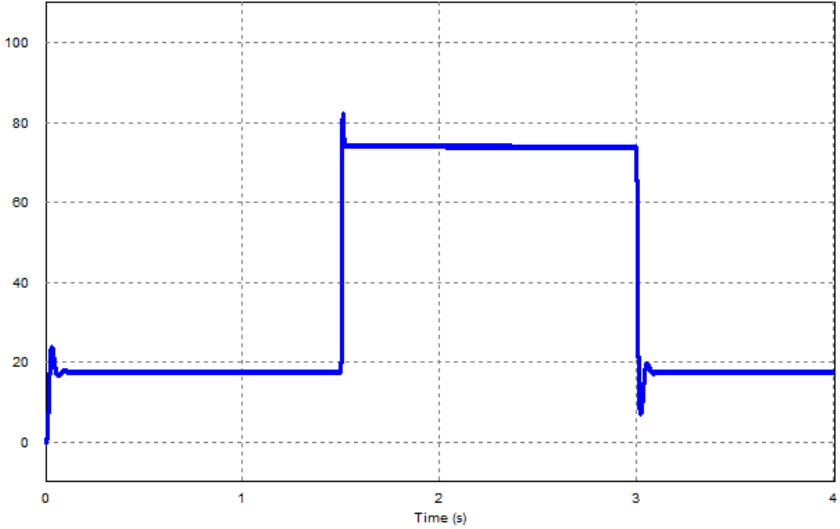


Figure 75. Single MFC Section Response to Instantaneous 300% Current Demand.

A Type-3 Controller is then designed for the isolated full-bridge Modular Isolated Conversion Stage (see Figure 76).

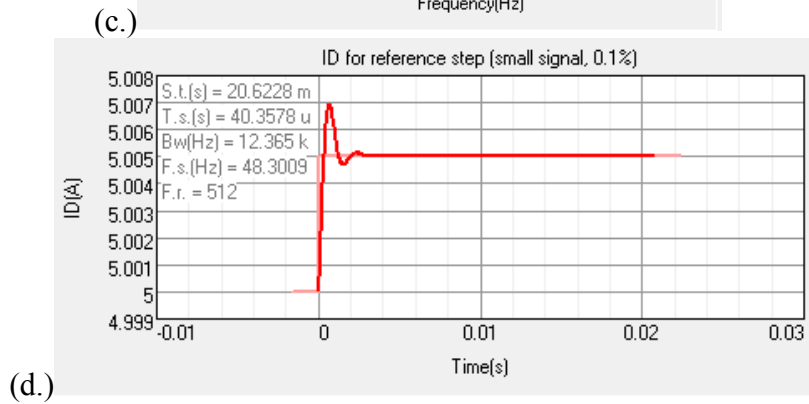
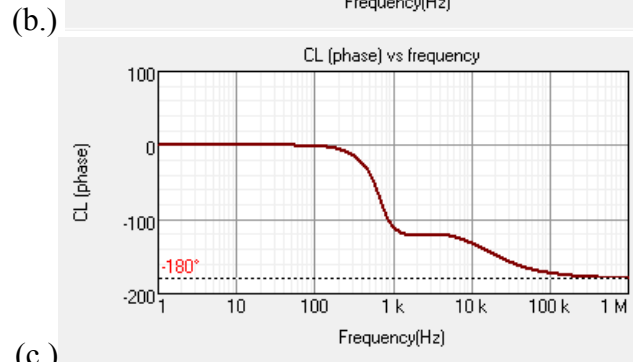
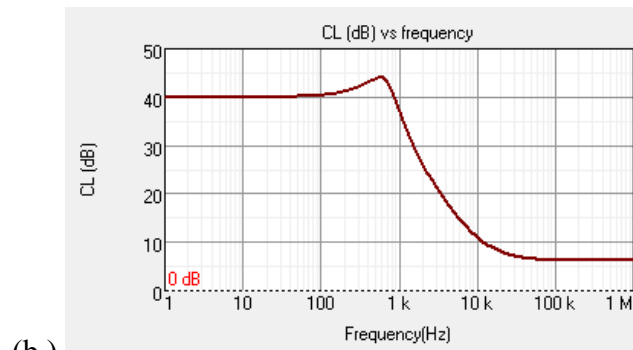
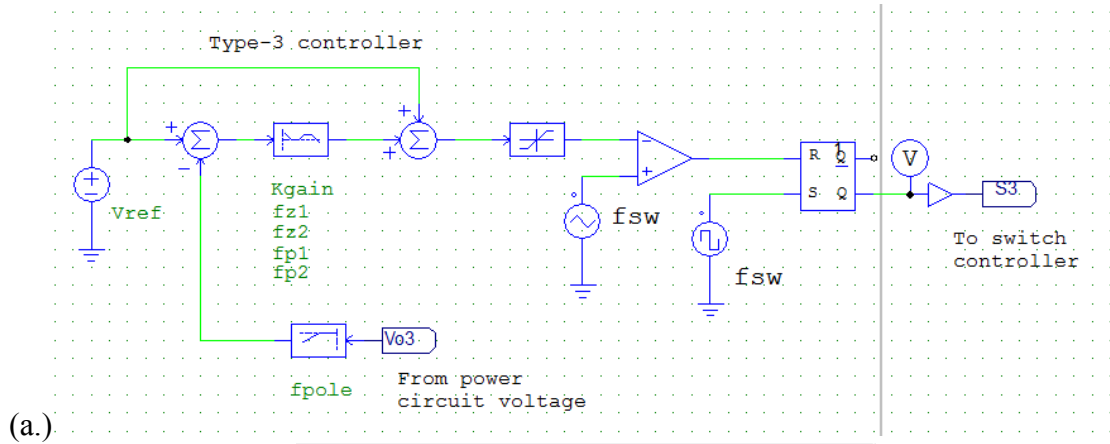


Figure 76. Type-3 output voltage control for the MFC+HES Modular Isolated Full-Bridge Converter Stage.

Figure 77 illustrates how a single isolated modular converter section handles a 300% increase in load.

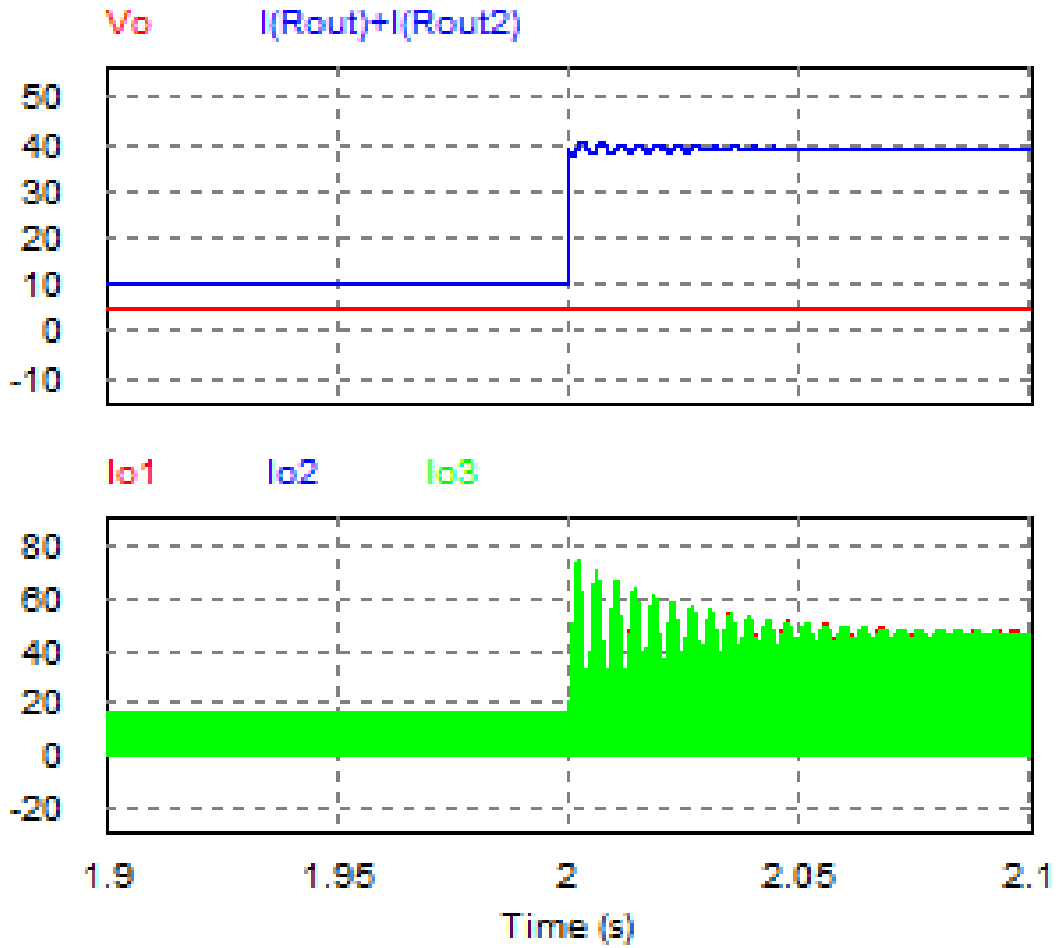


Figure 77. Dynamic Response of the MFC+HES Modular Isolated Full-Bridge Conversion Stage.

Conclusion

MFC+HES technology has been proposed in order to effectively integrate energy-dense MFC technology with power-dense energy storage device (ESD) technology. System modularization and hybridization were discussed initially, followed by ESD selection between supercapacitors (SCs) and lithium-ion batteries (LIBs). Next, system topology and design is discussed, and the MFC and LIBs are electrically modeled such that Middlebrook's Extra Element Theorem can mitigate unwanted system resonance and assist in stack size selection. Simulation and hardware results for a 100W MFC+HES system is shown to provide 300% boost current responses to sudden high-power load demand. Moreover, the following system benefits are realized: limp-home capability, evenly distributed heat/aging, and maximized output power.

CHAPTER VI

CONCLUSIONS AND FUTURE WORK

Power electronics has recently evolved into a top-tier technology discriminator for DERS applications. This dissertation presents three MPC DERS topologies which add to this area of expanding research. The PSC system has been shown to realize independent power control per source as well as increased output power, operational flexibility, thermal balancing, source availability, and cost-effectiveness for utility-scale fuel cell power generation. The ML9SC system features a design with low cost, high efficiency, high power quality, and low EMI characteristics in online UPS as well as six-phase/DFIG wind power generation. The MFC+HES system offers boost current energy storage, increased fault tolerance, limp-home capability, evenly distributed heat and aging, and maximized sectional power for low to medium power applications. Future work will include research for Crane Naval Surface Warfare Center under STO 219 Grant, “A Novel Mobile Electronic Hybrid Power Conditioning Unit.”

REFERENCES

- [1] US Energy Information Administration, "Annual Energy Outlook 2014," Internet: <http://www.eia.gov/forecasts/aeo/pdf/tbla1.pdf>, Feb. 1, 2011 [Oct. 1, 2013].
- [2] D. M. Robert W. Erickson, *Fundamentals of Power Electronics*, 2nd Edition ed. Norwell, Mass: Kluwer Academic, 2001, pp. 1-7.
- [3] D. F. Tan. Keynote Address, Power Electronics: "Power Electronics in Emerging Applications." American Power Electronics Conference, Ft. Worth Convention Center, Ft. Worth, TX, USA, March 17, 2014.
- [4] N. R. Friedman, "Distributed Energy Resources Interconnect Systems: Technology Review and Research Needs," Internet: <http://www.nrel.gov/docs/fy02osti/32459.pdf>, September 1, 2002 [March 20, 2014].
- [5] H. Matsuo, L. Wenzhong, F. Kurokawa, T. Shigemizu, and N. Watanabe, "Characteristics of the multiple-input DC-DC converter," *Industrial Electronics, IEEE Transactions on*, vol. 51, pp. 625-631, 2004.
- [6] H. Tao, A. Kotsopoulos, J. L. Duarte, and M. A. M. Hendrix, "Family of multiport bidirectional DC-DC converters," *Electric Power Applications, IEE Proceedings on*, vol. 153, pp. 451-458, 2006.
- [7] H. Behjati and A. Davoudi, "Single-stage multi-port DC-DC converter topology," *Power Electronics, IET*, vol. 6, pp. 392-403, 2013.
- [8] L. Yuan-Chuan and C. Yaow-Ming, "A Systematic Approach to Synthesizing Multi-Input DC-DC Converters," *Power Electronics, IEEE Transactions on*, vol. 24, pp. 116-127, 2009.
- [9] C. Yaow-Ming, L. Yuan-Chuan, and W. Feng-Yu, "Multi-input DC/DC converter based on the multiwinding transformer for renewable energy applications," *Industry Applications, IEEE Transactions on*, vol. 38, pp. 1096-1104, 2002.
- [10] H. Yuehui and C. K. Tse, "Circuit Theoretic Classification of Parallel Connected DC-DC Converters," *Circuits and Systems I: Regular Papers, IEEE Transactions on*, vol. 54, pp. 1099-1108, 2007.

- [11] L. Yan, R. Xinbo, Y. Dongsheng, L. Fuxin, and C. K. Tse, "Synthesis of Multiple-Input DC/DC Converters," *Power Electronics, IEEE Transactions on*, vol. 25, pp. 2372-2385, 2010.
- [12] M. Dongsheng, K. Wing-Hung, and T. Chi-Ying, "A pseudo-CCM/DCM SIMO switching converter with freewheel switching," *Solid-State Circuits, IEEE Journal of*, vol. 38, pp. 1007-1014, 2003.
- [13] A. Nami, F. Zare, A. Ghosh, and F. Blaabjerg, "A Hybrid Cascade Converter Topology With Series-Connected Symmetrical and Asymmetrical Diode-Clamped H-Bridge Cells," *Power Electronics, IEEE Transactions on*, vol. 26, pp. 51-65, 2011.
- [14] H. Behjati and A. Davoudi, "A MIMO topology with series outputs: An interface between diversified energy sources and diode-clamped multilevel inverter," in *Applied Power Electronics Conference and Exposition (APEC), 2012 Twenty-Seventh Annual IEEE*, 2012, pp. 1-6.
- [15] W. Hongfei, X. Peng, H. Haibing, Z. Zihu, and X. Yan, "Multiport Converters Based on Integration of Full-Bridge and Bidirectional DC-DC Topologies for Renewable Generation Systems," *Industrial Electronics, IEEE Transactions on*, vol. 61, pp. 856-869, 2014.
- [16] T. Haimin, A. Kotsopoulos, J. L. Duarte, and M. A. M. Hendrix, "Transformer-Coupled Multiport ZVS Bidirectional DC-DC Converter With Wide Input Range," *Power Electronics, IEEE Transactions on*, vol. 23, pp. 771-781, 2008.
- [17] O. C. Onar, O. H. A. Shirazi, and A. Khaligh, "Grid Interaction Operation of a Telecommunications Power System With a Novel Topology for Multiple-Input Buck-Boost Converter," *Power Delivery, IEEE Transactions on*, vol. 25, pp. 2633-2645, 2010.
- [18] K. Dongwon and G. A. Rincon-Mora, "Single-Inductor Multiple-Output Switching DC-DC Converters," *Circuits and Systems II: Express Briefs, IEEE Transactions on*, vol. 56, pp. 614-618, 2009.
- [19] S. Gui-Jia, J. P. Cunningham, and T. Lixin, "A Reduced-Part, Triple-Voltage DC-DC Converter for Electric Vehicle Power Management," in *Power Electronics Specialists Conference, 2007. PESC 2007. IEEE*, 2007, pp. 1989-1994.
- [20] H. Behjati and A. Davoudi, "A multi-port dc-dc converter with independent outputs for vehicular applications," in *Vehicle Power and Propulsion Conference (VPPC), 2011 IEEE*, 2011, pp. 1-5.

- [21] T. Bhattacharya, V. S. Giri, K. Mathew, and L. Umanand, "Multiphase Bidirectional Flyback Converter Topology for Hybrid Electric Vehicles," *Industrial Electronics, IEEE Transactions on*, vol. 56, pp. 78-84, 2009.
- [22] L. D. Salazar and J. R. Urra, "A novel three ports power conditioner for renewable electricity generators," in *IECON 2011 - 37th Annual Conference on IEEE Industrial Electronics Society*, 2011, pp. 1131-1136.
- [23] J. Wei and B. Fahimi, "Multiport Power Electronic Interface -- Concept, Modeling, and Design," *Power Electronics, IEEE Transactions on*, vol. 26, pp. 1890-1900, 2011.
- [24] H. Krishnaswami and N. Mohan, "Three-Port Series-Resonant DC-DC Converter to Interface Renewable Energy Sources With Bidirectional Load and Energy Storage Ports," *Power Electronics, IEEE Transactions on*, vol. 24, pp. 2289-2297, 2009.
- [25] Z. Tao and B. Francois, "Energy Management and Power Control of a Hybrid Active Wind Generator for Distributed Power Generation and Grid Integration," *Industrial Electronics, IEEE Transactions on*, vol. 58, pp. 95-104, 2011.
- [26] W. Hongfei, C. Runruo, Z. Junjun, X. Yan, H. Haibing, and G. Hongjuan, "A Family of Three-Port Half-Bridge Converters for a Stand-Alone Renewable Power System," *Power Electronics, IEEE Transactions on*, vol. 26, pp. 2697-2706, 2011.
- [27] W. Zhan and L. Hui, "Integrated MPPT and bidirectional battery charger for PV application using one multiphase interleaved three-port dc-dc converter," in *Applied Power Electronics Conference and Exposition (APEC), 2011 Twenty-Sixth Annual IEEE*, 2011, pp. 295-300.
- [28] J. T. Hawke, H. S. Krishnamoorthy, and P. N. Enjeti, "A new utility-scale power converter for large fuel cell power plants with individual stack power control," in *Applied Power Electronics Conference and Exposition (APEC), 2012 Twenty-Seventh Annual IEEE*, 2012, pp. 1482-1488.
- [29] R. Wolk, "High Megawatt Power Conditioning System," N. I. o. S. Technology, Ed., ed, 2012.
- [30] C. M. Colson, M. C. Deibert, M. R. Amin, C. Wang, and M. H. Nehrir, "Efficiency Evaluation of Solid-Oxide Fuel Cells in Combined Cycle Operations," *Journal of Fuel Cell Science and Technology*, vol. 6, pp. 021006-021006, 2009.

- [31] C. M. Colson, M. H. Nehrir, and C. Wang, "Modeling a large-scale utility-interconnected solid oxide fuel cell power plant," in *Power Symposium, 2008. NAPS '08. 40th North American*, 2008, pp. 1-5.
- [32] A. D. J. Larminie, *Fuel Cell Systems Explained*, 2nd Edition ed.: John Wiley & Sons, 2003.
- [33] Q. Xu, N. Wang, K. Ichiyanagi, and K. Yukita, "PEM Fuel Cell modeling and parameter influences of performance evaluation," in *Electric Utility Deregulation and Restructuring and Power Technologies, 2008. DRPT 2008. Third International Conference on*, 2008, pp. 2827-2832.
- [34] L. Palma, M. Harfman Todorovic, and P. N. Enjeti, "Analysis of Common-Mode Voltage in Utility-Interactive Fuel Cell Power Conditioners," *Industrial Electronics, IEEE Transactions on*, vol. 56, pp. 20-27, 2009.
- [35] G. Bernsten, "Scale-up experience with Mega-Watt Class Inverter Topologies," *Proc. Solid State Energy Conver. Alliance Workshop*, 2006.
- [36] A. H. Ranjbar, P. Shamsi, and B. Fahimi, "Power management in Multi-port Power Electronic Interface (MPEI) based on on-line reliability monitoring," in *Applied Power Electronics Conference and Exposition (APEC), 2013 Twenty-Eighth Annual IEEE*, 2013, pp. 3021-3026.
- [37] P. S. Shenoy, K. A. Kim, B. B. Johnson, and P. T. Krein, "Differential Power Processing for Increased Energy Production and Reliability of Photovoltaic Systems," *Power Electronics, IEEE Transactions on*, vol. 28, pp. 2968-2979, 2013.
- [38] L. Palma and P. N. Enjeti, "A Modular Fuel Cell, Modular DC-DC Converter Concept for High Performance and Enhanced Reliability," *Power Electronics, IEEE Transactions on*, vol. 24, pp. 1437-1443, 2009.
- [39] M. H. Todorovic, L. Palma, and P. N. Enjeti, "Design of a Wide Input Range DC-DC Converter With a Robust Power Control Scheme Suitable for Fuel Cell Power Conversion," *Industrial Electronics, IEEE Transactions on*, vol. 55, pp. 1247-1255, 2008.
- [40] Y. Watanabe, M. Matsumoto, and K. Takasu, "The market for utility-scale fuel cell plants," *Journal of Power Sources*, vol. 61, pp. 53-59, 7/1/1996.

- [41] A. J. Mason, D. J. Tschirhart, and P. K. Jain, "New ZVS Phase Shift Modulated Full-Bridge Converter Topologies With Adaptive Energy Storage for SOFC Application," *Power Electronics, IEEE Transactions on*, vol. 23, pp. 332-342, 2008.
- [42] J. Song-Manguelle, M. Harfman-Todorovic, R. Gupta, D. Zhang, S. Chi, L. Garces, *et al.*, "A Modular Stacked DC Transmission and Distribution System for Long Distance Subsea Applications," *Industry Applications, IEEE Transactions on*, vol. PP, pp. 1-1, 2014.
- [43] Y. Zhao and T. A. Lipo, "Space vector PWM control of dual three-phase induction machine using vector space decomposition," *Industry Applications, IEEE Transactions on*, vol. 31, pp. 1100-1109, 1995.
- [44] F. Blaabjerg, S. Freysson, H. H. Hansen, and S. Hansen, "A new optimized space-vector modulation strategy for a component-minimized voltage source inverter," *Power Electronics, IEEE Transactions on*, vol. 12, pp. 704-714, 1997.
- [45] M. Jones, S. N. Vukosavic, D. Dujic, E. Levi, and P. Wright, "Five-leg inverter PWM technique for reduced switch count two-motor constant power applications," *Electric Power Applications, IET*, vol. 2, pp. 275-287, 2008.
- [46] C. B. Jacobina, I. Soares de Freitas, and A. M. N. Lima, "DC-Link Three-Phase-to-Three-Phase Four-Leg Converters," *Industrial Electronics, IEEE Transactions on*, vol. 54, pp. 1953-1961, 2007.
- [47] C. B. Jacobina, I. Soares de Freitas, and E. R. C. da Silva, "Reduced-Switch-Count Six-Leg Converters for Three-Phase-to-Three-Phase/Four-Wire Applications," *Industrial Electronics, IEEE Transactions on*, vol. 54, pp. 963-973, 2007.
- [48] T. Kominami and Y. Fujimoto, "A Novel Nine-Switch Inverter for Independent Control of Two Three-Phase Loads," in *Industry Applications Conference, 2007. 42nd IAS Annual Meeting. Conference Record of the 2007 IEEE*, 2007, pp. 2346-2350.
- [49] C. Liu, B. Wu, N. Zargari, and D. Xu, "A Novel Three-phase Three-leg AC/AC Converter Using Nine IGBTs," in *Power Electronics Specialists Conference, 2007. PESC 2007. IEEE*, 2007, pp. 2685-2690.
- [50] M. Heydari, A. Y. Varjani, M. Mohamadian, and A. Fatemi, "A novel dual-output six-switch three-phase inverter," in *IECON 2011 - 37th Annual Conference on IEEE Industrial Electronics Society*, 2011, pp. 1109-1114.

- [51] S. M. D. Dehnavi, M. Mohamadian, A. Yazdian, and F. Ashrafzadeh, "Space Vectors Modulation for Nine-Switch Converters," *Power Electronics, IEEE Transactions on*, vol. 25, pp. 1488-1496, 2010.
- [52] G. Feng, Z. Lei, L. Ding, L. Poh Chiang, T. Yi, and G. Houlei, "Optimal Pulsewidth Modulation of Nine-Switch Converter," *Power Electronics, IEEE Transactions on*, vol. 25, pp. 2331-2343, 2010.
- [53] M. F. Schweizer, T. Kolar, "Comparative Evaluation of Advanced 3-phase 3-level Inverter/Converter Topologies against 2-level Systems," *Industrial Electronics, IEEE Transactions on*, vol. PP, p. 1, 2013 (Early Access).
- [54] Z. Wenping, X. Dehong, L. Xiao, X. Ren, L. Haijin, D. Dezhi, *et al.*, "Seamless Transfer Control Strategy for Fuel Cell Uninterruptible Power Supply System," *Power Electronics, IEEE Transactions on*, vol. 28, pp. 717-729, 2013.
- [55] K. Komatsu, M. Yatsu, S. Miyashita, S. Okita, H. Nakazawa, S. Igarashi, *et al.*, "New IGBT modules for advanced neutral-point-clamped 3-level power converters," in *Power Electronics Conference (IPEC), 2010 International*, 2010, pp. 523-527.
- [56] T. Bruckner, S. Bernet, and H. Guldner, "The active NPC converter and its loss-balancing control," *Industrial Electronics, IEEE Transactions on*, vol. 52, pp. 855-868, 2005.
- [57] M. Heydari, A. Y. Varjani, M. Mohamadian, and H. Zahedi, "A novel variable-speed wind energy system using permanent-magnet synchronous generator and nine-switch AC/AC converter," in *Power Electronics, Drive Systems and Technologies Conference (PEDSTC), 2011 2nd*, 2011, pp. 5-9.
- [58] H. S. Che, W. P. Hew, N. A. Rahim, E. Levi, M. Jones, and M. J. Duran, "A six-phase wind energy induction generator system with series-connected DC-links," in *Power Electronics for Distributed Generation Systems (PEDG), 2012 3rd IEEE International Symposium on*, 2012, pp. 26-33.
- [59] T. M. Research, "Fuel Cell Market -- Global Industry Size, Market Share, Trends, Analysis, and Forecasts (2012-2018)," 2012.
- [60] H. He, R. Xiong, and J. Fan, "Evaluation of Lithium-Ion Battery Equivalent Circuit Models for State of Charge Estimation by an Experimental Approach," *Energies*, vol. 4, pp. 582-598, 2011.

- [61] M. Ceraolo, C. Miulli, and A. Pozio, "Modelling static and dynamic behaviour of proton exchange membrane fuel cells on the basis of electro-chemical description," *Journal of Power Sources*, vol. 113, pp. 131-144, 1/1/ 2003.
- [62] L. Palma, M. Harfman-Todorovic, P. Enjeti, and C. Sewan, "Analysis of DC-DC Converter Stability in Fuel Cell Powered Portable Electronic Systems," in *Power Electronics Specialists Conference, 2006. PESC '06. 37th IEEE, 2006*, pp. 1-6.
- [63] M. Harfman Todorovic, L. Palma, and P. N. Enjeti, "Design of a Wide Input Range DC-DC Converter With a Robust Power Control Scheme Suitable for Fuel Cell Power Conversion," *Industrial Electronics, IEEE Transactions on*, vol. 55, pp. 1247-1255, 2008.
- [64] L. Palma, "Supercapacitors in power electronic systems," M.S. Thesis, Texas A&M University, USA, 2003.

APPENDIX A

CASE STUDY: HYBRID ENERGY STORAGE DEVICE SELECTION

In this design example, a 42V/1kW Ballard fuel cell is divided into 7 modular sections. Each fuel cell section is connected in parallel with a hybrid energy storage bank containing a 2.7V/3kF Maxwell supercapacitor and a 3.3V/2.3A.h A123-System LiFePo₄ Battery. A single modular topological connection between the fuel cell section, the supercapacitor, and the lithium-ion battery is clearly illustrated in Figure 78. Here the synchronous multi-level high-gain bi-directional dc-dc converter runs at a switching frequency of 100kHz, and two single-pole double-throw relays are used to switch from one bank to another. Solid state switches could be used instead, but the SPDT relays are less expensive, and, depending upon application, most likely will not need to be thrown frequently.

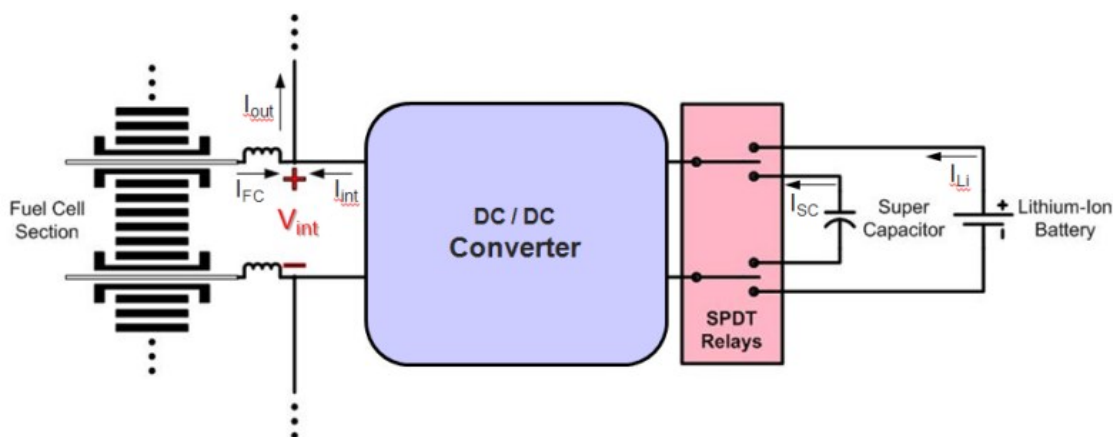


Figure 78. Fuel cell section modularly interfaced with a supercapacitor/Li-ion energy storage bank.

Throughout this design example, the following three interface arrangements are considered as well as the sustainability of their current boosting capabilities:

- (i.) *Supercapacitor energy bank*—The SPDT relays connect the supercapacitor in parallel with the modular fuel cell section via the multi-level DC-DC converter.
- (ii.) *Li-ion energy bank*— The SPDT relays connect the Li-ion battery in parallel with the modular fuel cell section via the multi-level DC-DC converter.
- (iii.) *Supercapacitor and Li-ion hybrid energy bank*— The SPDT relays connect the supercapacitor in parallel to the modular fuel cell section via the multi-level DC-DC converter. When the supercapacitor energy is depleted, the SPDT relays switch such that energy is acquisitioned from the Li-ion battery.

Throughout the design example analysis, the current boost factor (x_f) is defined in Equation A.1 as the ratio of current provided from the energy storage bank interface (I_{int}) with to the current provided from the fuel cell section (I_{FC}).

$$x_f \triangleq \frac{I_{int}}{I_{FC}} \quad (\text{A.1})$$

In the succeeding subsections, device current limitations are considered while energy conservation equations are utilized to derive the maximum time-sustainable current-boost equations for each of the three energy storage bank interface arrangements. It is imperative to note that the total boost current provided from each fuel cell module is found from the following equation:

$$I_{out} = I_{FC} + I_{int} = I_{FC} \cdot (1 + x_f). \quad (\text{A.2})$$

Modular Fuel Cell Supercapacitor Interface

The first portion of this design example inspects the case in which only the supercapacitor in the energy storage bank is allowed to discharge a boost current through the dc-dc converter interface to the load.

Assuming the power loss in the converter to be negligible, one can use the capacitive energy conservation equation

$$E = \frac{1}{2} \cdot C \cdot V^2 = P \cdot t \quad (\text{A.3})$$

to derive the boost current. Below, V_{SC} is defined as the rated supercapacitor voltage and DoD is defined as the chosen depth of discharge. In this case, the depth of discharge is chosen to be 50% such that 75% percent of all stored capacitive energy is discharged to the load.

$$E = \frac{1}{2} \cdot C \cdot V_{SC}^2 \cdot (1 - DoD^2) = V_{int} \cdot I_{int} \cdot t \quad (\text{A.4})$$

By substituting Equation A.1 into Equation A.3, one can solve for the ideal boost-current factor equation.

$$x_{f1}(t) = \frac{C \cdot V_{SC}^2 \cdot (1 - DoD^2)}{2 \cdot V_{int} \cdot I_{FC} \cdot t} = \frac{1.266}{t_{mins}} \quad (\text{A.5})$$

In order to consider the current limit of the supercapacitor, the maximum boost-current is determined by equating the average power drawn from the supercapacitor with the power drawn from the dc-dc converter and solving for the boost factor.

$$x_{f1,max} = \frac{\left(\frac{1 + DoD}{2}\right) \cdot V_{SC} \cdot I_{SC,max}}{V_{int} \cdot I_{FC}} = 260\% \quad (\text{A.6})$$

Combining Equations A.5 and A.6 yields the supercapacitor energy storage bank's boost factor with appropriate device current limitations (see Figure 79).

$$x_{f1(t)} = \left\{ \begin{array}{ll} 2.60 & \text{for } 0 \leq t_{mins} \leq 0.49 \\ \frac{1.27}{t_{mins}} & \text{for } 0.49 < t_{mins} \end{array} \right\} \quad (\text{A.7})$$

Overall, modularly interfacing the fuel cell with the supercapacitor energy storage bank provides more limited sustainability times, higher system current-boosting capabilities (up to 360%), and higher cycling lifetimes in comparison to the lithium-ion energy storage bank interface discussed in the next section.

Modular Fuel Cell Li-Ion Battery Interface

The second part of this design example focuses on the case where only the lithium-ion battery in the energy storage bank is allowed to discharge a boost current through the dc-dc converter interface to the load.

By substituting Equation A.1 into the energy conservation equation below,

$$E = C_{nom} \cdot V_{Li} = V_{int} \cdot I_{int} \cdot t \quad (\text{A.8})$$

one can solve for the ideal boost-current factor equation.

$$x_{f2(t)} = \frac{C_{nom} \cdot V_{Li}}{V_{int} \cdot I_{FC} \cdot t} = \frac{3.16}{t_{mins}} \quad (\text{A.9})$$

Using the maximum rated current for the battery, the maximum boost factor and sustainability time can be calculated.

$$x_{f2,max} = \frac{V_{Li} \cdot I_{Li,max}}{V_{int} \cdot I_{FC}} = 160\% \quad (\text{A.10})$$

$$t_{max} = \frac{C_{nom} \cdot V_{Li}}{V_{int} \cdot I_{FC} \cdot x_{f2,max}} = 1.97 \text{ mins} \quad (\text{A.11})$$

Combining Equations A.10 and A.11 provides the lithium-ion energy storage bank's boost factor with appropriate device current limitations (see Figure 79).

$$x_{f2(t)} = \left\{ \begin{array}{ll} 1.60 & \text{for } 0 \leq t_{mins} \leq 1.97 \\ \frac{3.16}{t_{mins}} & \text{for } 1.97 < t_{mins} \end{array} \right\} \quad (\text{A.12})$$

Altogether, modularly interfacing the fuel cell with the lithium-ion energy storage bank provides extended sustainability times, more limited system current-boosting capabilities (up to 260%), and more limited cycling lifetimes in comparison to the supercapacitor energy storage bank interface discussed in the previous section.

Modular Fuel Cell / Hybrid Interface

The final portion of this design example considers the hybrid case where energy is first drawn from the supercapacitor and then from the lithium-ion battery. In this scenario, the hybrid energy storage bank sustainability time curve can be found by summing the boost factor sustainability times of the supercapacitor and lithium-ion battery.

$$t_{x_{f3}} = t_{(x_{f1})} + t_{(x_{f2})} \quad (\text{A.13})$$

Altogether, combining the two units into a single hybrid energy storage bank allows each device's benefits to compensate for the other's weaknesses. This results extended sustainability times, higher system current-boosting capabilities (up to 360%),

and maximized cycling lifetimes in comparison to the supercapacitor and lithium-ion energy individual storage banks (see Figure 79).

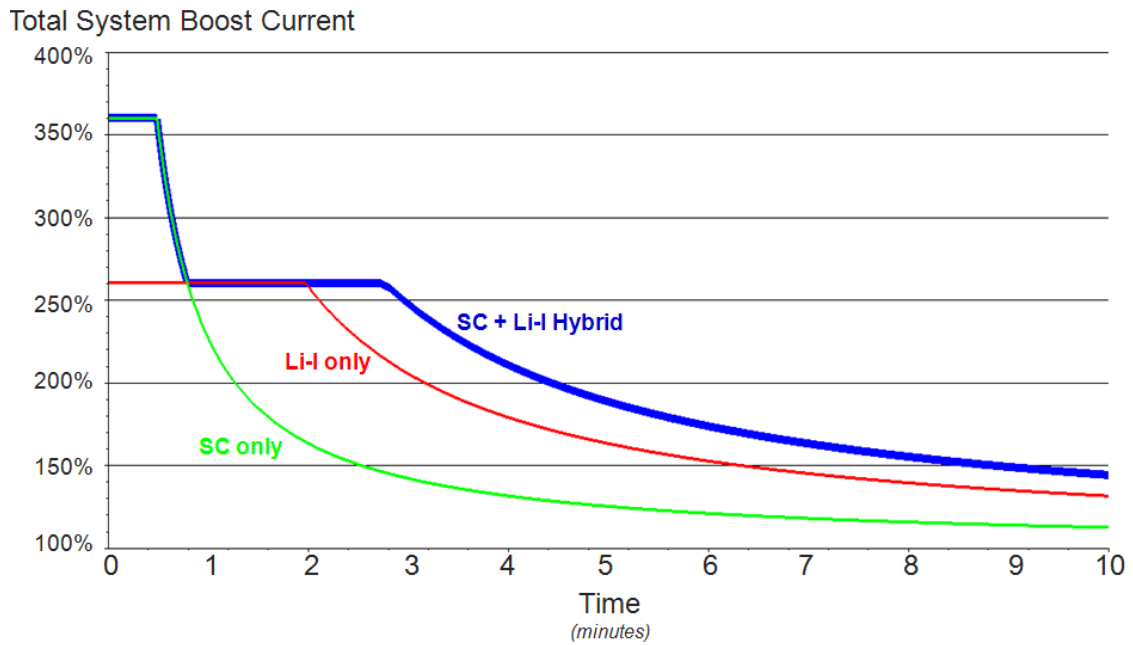


Figure 79. Total time-sustainable boost-current provision of a modular fuel cell section modularly interfaced with (a.) a supercapacitors only, (b.) a Li-Ion batteries only, and (c.) a hybrid combination of both (a.) and (b.).